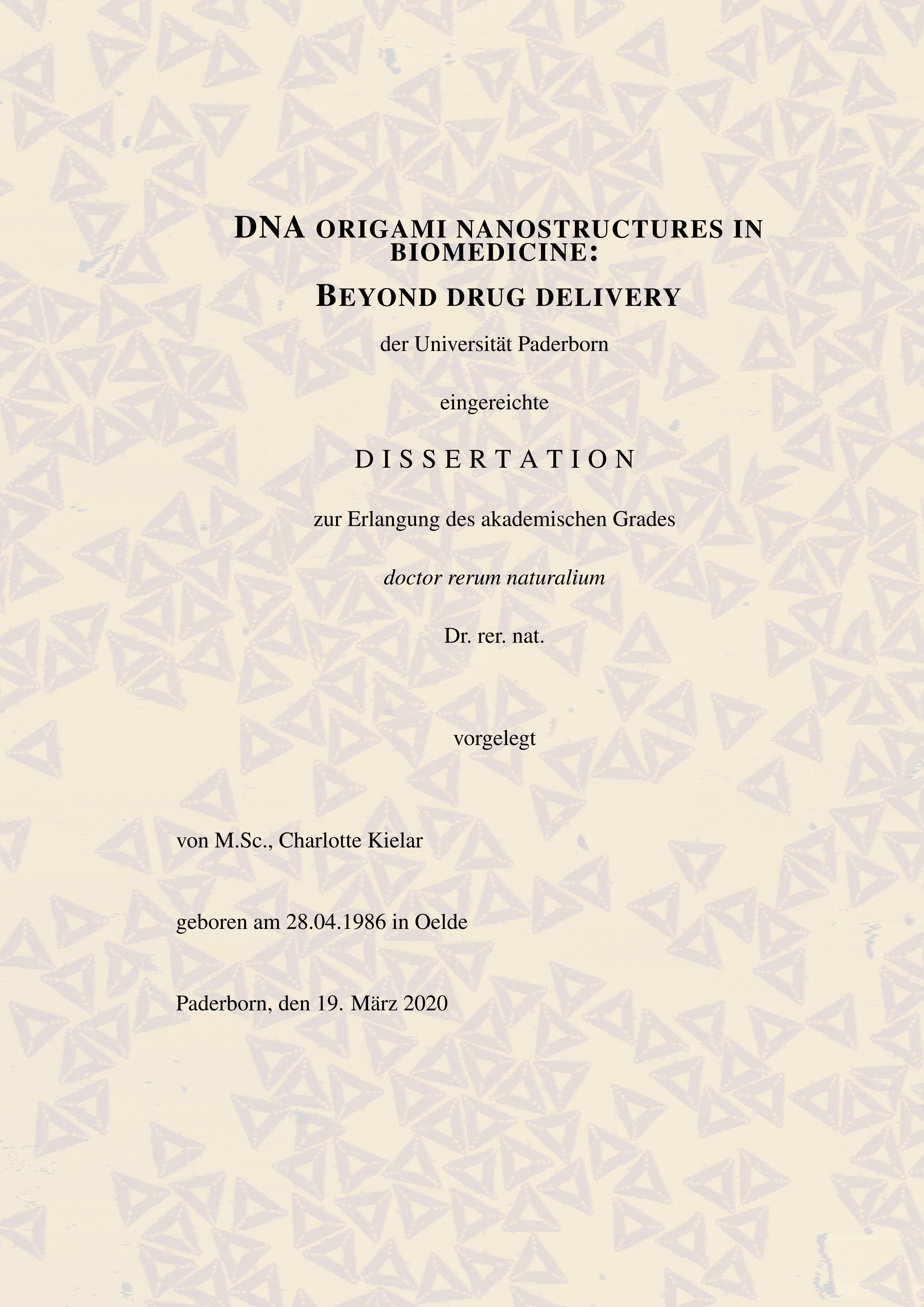

DNA ORIGAMI NANOSTRUCTURES IN BIOMEDICINE:

BEYOND DRUG DELIVERY

der Universität Paderborn

eingereichte

DISSERTATION

zur Erlangung des akademischen Grades

doctor rerum naturalium

Dr. rer. nat.

vorgelegt

von M.Sc., Charlotte Kielar

geboren am 28.04.1986 in Oelde

Paderborn, den 19. März 2020

Promotionskommission:
Vorsitzender: Prof. Dr. Matthias Bauer
Erstgutachter: PD Dr. Adrian Keller
Zweitgutachter: Prof. Dr. Ilko Bald
Drittgutachter: Prof. Dr. Guido Grundmeier

Bibliographic Description

Kielar, Charlotte

DNA origami nanostructures in biomedicine:
Beyond drug delivery

Universität Paderborn, Dissertation
119 S., 230 Lit., 63 Abb., 17 Tab.

Abstract

The present work is concerned with applications of DNA origami nanostructures and can be divided into three main parts. In the first part the experiments performed in this work will be put into a larger context of DNA origami as a tool for nanotechnology. The fundamentals of the DNA origami technique as well as atomic force microscopy and high-speed atomic force microscopy (HS-AFM) needed to get a proper understanding of the results of this work will be covered.

The second part may be divided into two parts as well. The first of which is concerned with the structural stability of DNA origami structures in low Mg^{2+} buffer solutions and after long-term storage of the staple strands used for assembly. Both are relevant aspects for drug-delivery and drug-discovery applications as well. It is further shown that DNA origami remain stable in selected low Mg^{2+} buffers and that even after storage of the staple strands for several months DNA origami may be assembled with high yield. The second half of the main part devoted to the application of DNA origami for single-molecule studies which may aid fragment-based drug discovery and how screening experiments can be speed up using HS-AFM. The results show that precise geometric arrangement of functional molecules on DNA origami simultaneous investigation of different protein-ligand binding systems is possible and that under certain conditions HS-AFM can be used to allow high-throughput screening.

At last, the results obtained within this work will be summarized and an outlook about possible future research will be given.

Zusammenfassung

Die vorliegende Arbeit befasst sich mit Anwendungen von DNA-Origami-Nanostrukturen und kann in drei Hauptteile unterteilt werden. Im ersten Teil werden die in dieser Arbeit durchgeführten Experimente in den Kontext von DNA-Origami als Werkzeug für die Nanotechnologie gestellt. Zudem werden die Grundlagen zur DNA-Origami-Technik sowie (Hochgeschwindigkeits-)Rasterkraftmikroskopie (HS-AFM), die zum Verständnis dieser Arbeit benötigt werden, vermittelt.

Der zweite Teil kann auch in zwei Abschnitte gegliedert werden. Der erste befasst sich mit der strukturellen Stabilität von DNA-Origami-Strukturen in Pufferlösungen mit niedrigem Mg^{2+}-Gehalt und nach Langzeitlagerung der für die Assemblierung verwendeten Heftstränge. Beides sind relevante Aspekte für Anwendungen für Wirkstofftransport und -entdeckung. Es wird gezeigt, dass DNA-Origami in ausgewählten Puffern mit niedrigem Mg^{2+}-Gehalt stabil bleiben und dass DNA-Origami auch nach mehrmonatiger Lagerung der Heftstränge mit hoher Ausbeute assembliert werden können. Die zweite Hälfte des Hauptteils widmet sich der Anwendung von DNA-Origami für Einzelmolekülstudien, die der fragmentbasierten Wirkstoffentdeckung dienen können, und wie Screening-Experimente mit HS-AFM beschleunigt werden können. Die Ergebnisse zeigen, dass eine genaue geometrische Anordnung funktioneller Moleküle auf DNA-Origami möglich ist, um verschiedene Protein-Liganden-Bindungssysteme gleichzeitig zu untersuchen, und dass HS-AFM unter bestimmten Bedingungen für ein Hochdurchsatz-Screening verwendet werden kann.

Abschließend werden die Ergebnisse dieser Arbeit zusammengefasst und ein Ausblick auf mögliche zukünftige Forschungen gegeben.

Abbreviations

HS-AFM	High-Speed Atomic Force Microscope
AFM	Atomic Force Microscope
SAv	streptavidin
Bt	biotin
iBt	iminobiotin
dBt	desthiobiotin
SEM	scanning electron microscope
EDTA	ethylenediaminetetraacetic acid
TAE	tris-acetate-EDTA
AGE	Agarose Gel Electrophoresis
TAMRA	tetramethylrhodamine
FAM	fluorescein amidite
Cy5.5	cyanine 5.5
IgG	immunoglobulin g

Contents

Bibliographic description I

Abstract III

Zusammenfassung V

Abbreviations VII

Contents VIII

1 Introduction 3

2 DNA origami 7
- 2.1 Controlled assembly of 2D and 3D DNA origami systems 8
- 2.2 Arrangement of functional groups via spatial addressability of DNA origami 9
- 2.3 Structural stability of DNA origami nanostructures 15

3 Atomic Force Microscopy and High-Speed Atomic Force Microscopy 21
- 3.1 Atomic Force Microscope 22
- 3.2 Suitable substrate surfaces for AFM imaging 25
  - 3.2.1 Mica surface 25
  - 3.2.2 Planar lipid bilayer (PLB) surface 25
  - 3.2.3 Langmuir-Blodgett-film and -Schaefer-film of an organic mono- and Multilayer 25
- 3.3 High-Speed Atomic Force Microscope (HS-AFM) 26
  - 3.3.1 Feedback bandwidth 26
  - 3.3.2 Adjusting elements for HS-AFM 28
  - 3.3.3 Comparison between AFM and HS-AFM 32

4 Structural stability of DNA origami 35
- 4.1 On the Stability of DNA Origami Nanostructures in Low-Magnesium Buffers 36
  - 4.1.1 Introduction 36
  - 4.1.2 Results and Discussion 37
  - 4.1.3 Conclusion 45
  - 4.1.4 Materials and Methods 45
- 4.2 Effect of Staple Age on DNA Origami Nanostructure Assembly and Stability 47
  - 4.2.1 Introduction 47
  - 4.2.2 Results and Discussion 48
  - 4.2.3 Conclusion 54
  - 4.2.4 Materials and Methods 55

5 DNA origami nanostructures for drug discovery 57
- 5.1 DNA origami based single-molecule assay for fragment-based drug discovery 58
  - 5.1.1 Introduction 58

5.1.2 Results and Discussion 59
5.1.3 Conclusion 71
5.1.4 Material and Methods 72
5.2 Quantitative assessment of tip effects in single-molecule High-Speed AFM 76
5.2.1 Introduction 76
5.2.2 Results and Discussion 77
5.2.3 Conclusion and outlook 84
5.2.4 Materials and Methods 85

6 Summary and Outlook **91**

List of Figures **93**

List of Tables **97**

Bibliography **99**

Publications **117**

Acknowledgements **119**

Chapter 1

Introduction

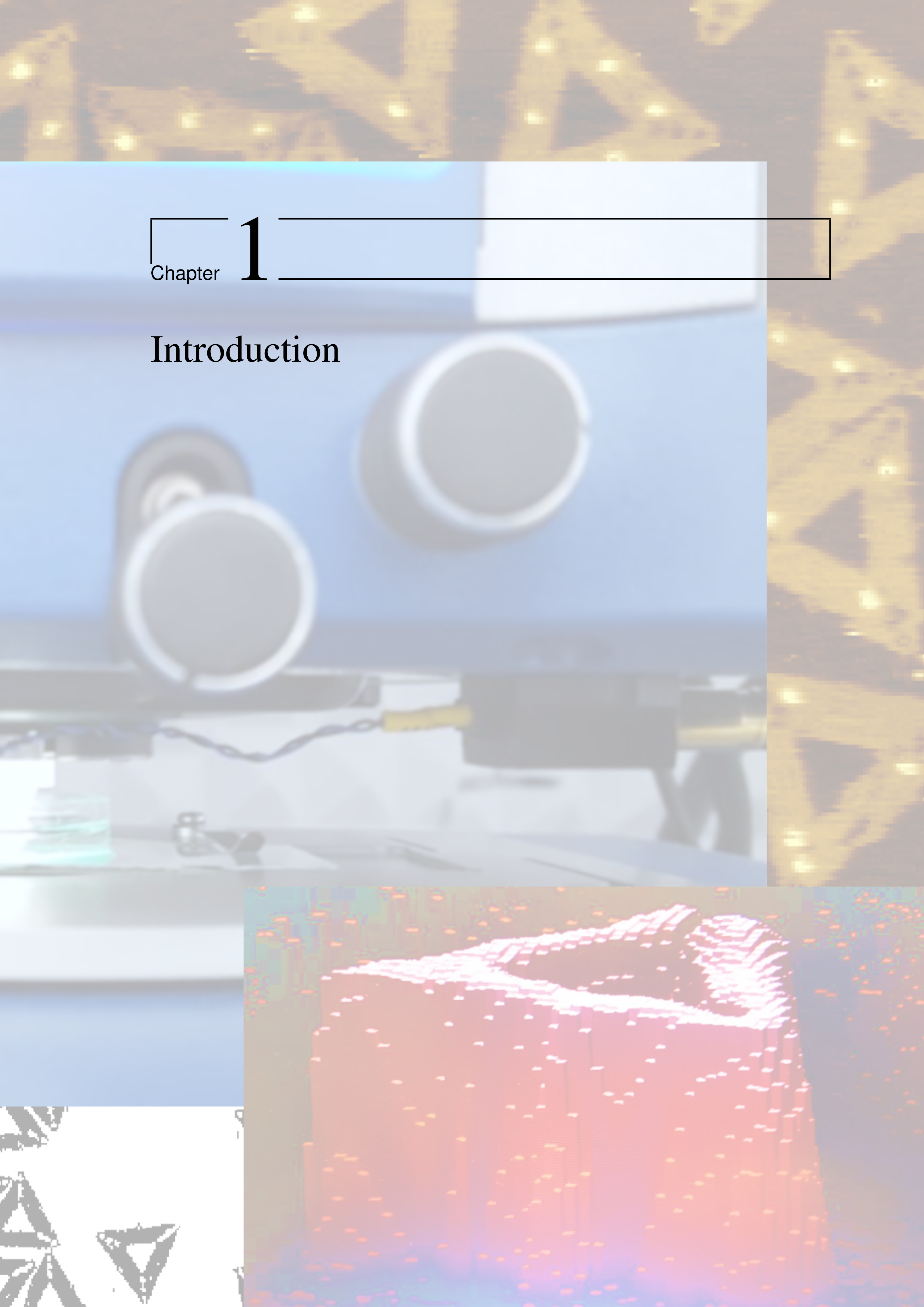

In the field of nanotechnology, Seemann laid the theoretical foundations for the nanoscale construction method of using DNA as a material [1]. Only after that, DNA was transformed into more complex forms and lattice systems, so that these structures with a size of 10 to 20 nm received a lot of attention and interest in DNA nanotechnology, but still left a lot of room for improvement and paved the way for our current DNA origami systems [2–13].

Interesting applications of DNA origami in the context of nanotechnology are the development of DNA machines [14, 15], spatial organization of nanoparticles and proteins [16–20], plasmonic nanostructures [21], and platforms for structural biology [22]. After Rothemund demonstrated hybridization of a given single stranded DNA (ssDNA scaffold) with specially designed oligonucleotides, to fold almost arbitrary shapes by self-assembly [23] the number of studied systems drastically increased. When folded correctly, the resulting DNA origami structures can serve as the basic framework for the production of materials on the nanometer scale with a yield of almost 100%. This process of one-pot synthesis for the production of DNA origami has been used to produce various two- and three-dimensional arrangements [24–33].

A significant part of this work is concerned with applications of DNA origami which may be classified as biomedical research. Here the use of DNA origami systems is gaining particular reputation in the fields of drug discovery and drug delivery. Considering drug delivery applications there are basically two different approaches. In the first approach DNA origami are directly used as a delivery system by loading them with pharmaceutics which may be released under specified conditions [34, 35]. DNA origami drug delivery systems targeted at tumorous environments have been successfully demonstrated, e.g. by Zhang *et al.* [36] and Li *et al.* [37]. An example system in which DNA origami serve as templates for size controlled growth of liposomes which may then be loaded with pharmaceutics has been demonstrated by Yang *et al.* [38] in 2016. As applications in both, drug discovery and drug delivery, rely on the structural stability of the DNA origami, this work additionally focuses on a systematic study of the stability of different DNA origami in different buffer solutions and after long-term cry-storage of the constituents.

Another important field in biomedical research that has attracted a lot of interest is concerned with so-called fragment-based drug discovery [39]. As Erlanson *et al.* [39] point out, in contrast to former approaches used in drug discovery, it is far more easy to optimize the interaction of small molecules, so-called fragments, with a desired target molecule. Essentially fragment-based drug discovery consists of two major steps: finding fragments and converting fragments into so-called Hits and Leads. In order to narrow down the number of potential hits for a given binding site of a protein, several computational and reverse engineering techniques have been elaborated over the years [40–45]. The actual fragment identification is then typically performed using direct binding assays at high concentrations [46], mass spectrometry methods [47], crystallography-based approaches [48], or NMR-based screening [49]. Promising fragments are then typically extended or linked using the target as a template for the synthesis [50, 51]. Due to the possibility to functionalize DNA origami with nanometer control over the exact position of the functional entities [12, 52, 53], DNA origami may help in both, fragment identification and Lead design. The high spatial addressability allows to quantitatively study the affinity of several functional groups to a given target protein, or, as will be shown in chapter 5.1, even different binding systems at once on a single DNA origami.

Binding affinities are determined by atomic force microscopy imaging. Fast screening is highly desirable for drug discovery applications. However, considering high-speed atomic force microscopy to speed up data acquisition, the rapidly scanning tip may significantly disturb the systems under investigation. Therefore, this work additionally studies tip effects in high-speed AFM measurements of protein-ligand binding reactions on DNA origami substrates.

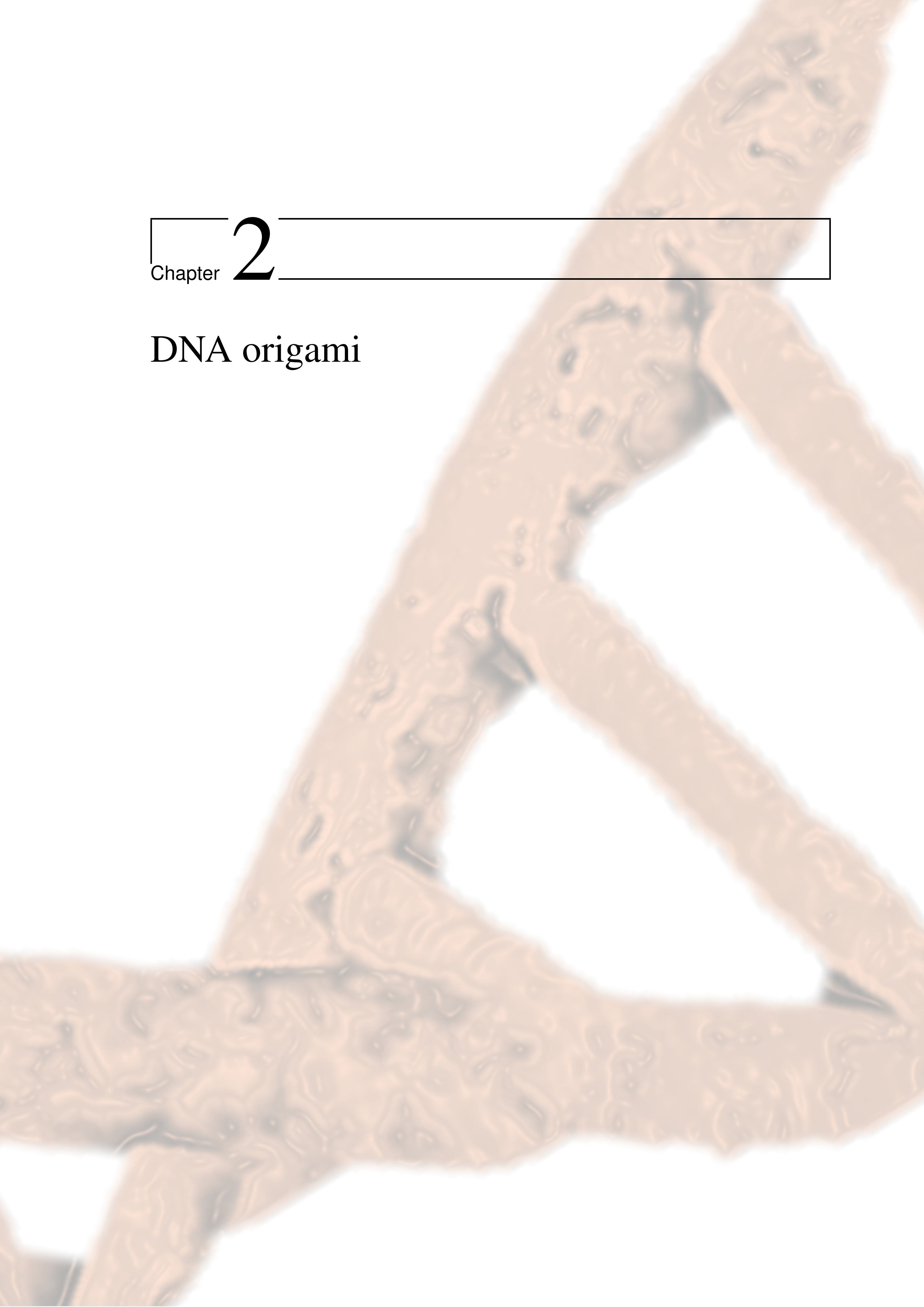

Chapter 2

DNA origami

2.1 Controlled assembly of 2D and 3D DNA origami systems

DNA origami structures, as first presented by Rothemund [23], offer a variety of applications in the field of nanotechnology [54–56] and basic research at the level of single-molecule studies [52, 57–60]. By hybridization with specially designed oligonucleotide chains, a given single-stranded DNA (ssDNA) can be self-assembled into almost any shape [23]. When properly folded, the resulting DNA origami structures can serve as a backbone for making materials on the nanometer scale. Likewise, the targeted modification of the oligonucleotides used for the folding can be used for a spatially selective functionalization on the nanometer scale, too [12, 21, 58–61]. These properties make DNA origami excellent substrates for single-molecule studies of biochemical reactions and processes.
By using DNA origami, it is possible to realize in nanotechnology the production of complex and almost any shapes with high yield. The preparation is carried out with a ssDNA as a scaffold. For this purpose, specially synthesized oligonucleotides (staple strands) of about 40 bases each are added. Each staple strand binds several times with different sequence sections of the ssDNA. By hybridization of the staple strand at two sites on the DNA backbone, the single strand is pulled together at this point. Utilizing Watson-Crick base pairing, ensembles of staple strands tuned to a particular ssDNA can be designed to fold into two- or three-dimensional structures by hybridization with the staple strands in a self-assembly process. The shape of the resulting DNA origami is basically encoded in the sequences of the individual oligonucleotides. In order to obtain a stoichiometric yield in the folding, a large excess of staple strands compared to the scaffold strand is used [23, 58].

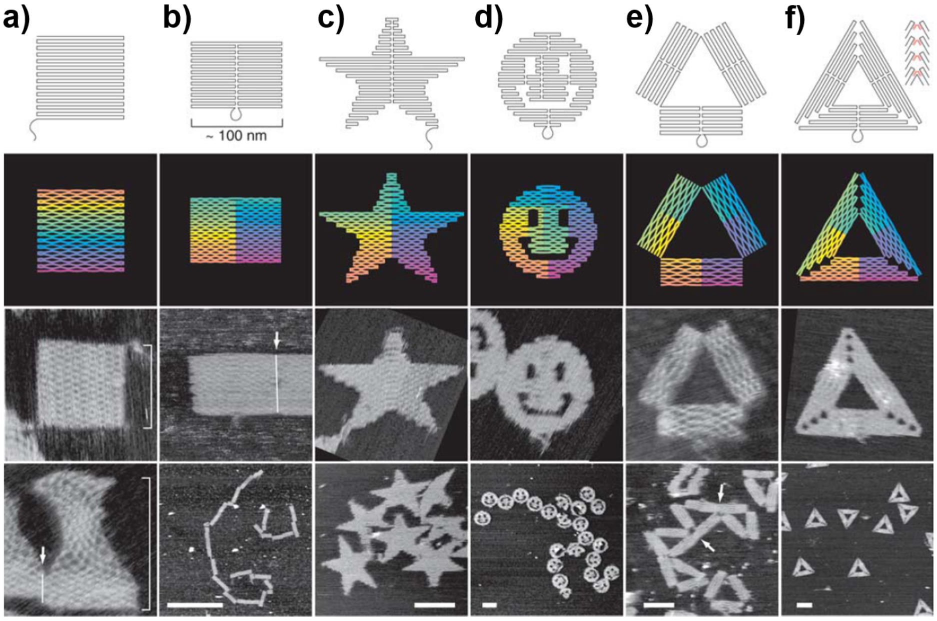

Figure 2.1: Overview of the first DNA origami created by Rothemund, (a) square, (b) rectangle, (c) star, (d) smiley, (e) triangle with rectangular domains, (f) sharp triangle with trapezoidal domains [23]. Reprinted by permission from Springer Nature: Nature: nature *Folding DNA to create nanoscale shapes and patterns*, Paul W. K. Rothemund, (2006).

In 2006, Rothemund published his work on the production of DNA origami containing the single stranded DNA M13mp18 from a 7249 nucleotide viral genome [23]. The DNA origami shown in Figure 2.1 were prepared with a 100-fold excess of 200–250 oligonucleotides to ensure binding and thus controlled folding at the defined sites. Since the sequences of the DNA strand as well as those of the staple strands are known, oligonucleotides can be specifically modified for example with biotin

(Bt) [12] or fluorescent substances [61] and incorporated in the self-assembly of the DNA strand to obtain functionalized origami. In this way not only more complex structures can be made from several DNA origami, but also functionalized sites can be visualized by inserted markers [23].

Another interesting construction of DNA origami occurs with wireframe DNA origami. The folding of polygonal 3D DNA origami structures is demonstrated in the work of Benson *et al.* with designs which differ from the traditional DNA origami structures [62]. Here, a more open helical conformation is used. Only one helix per edge is used. This means that the meshes at the edges are replaced by single DNA double strands so that the scaffold strand crosses these edges once.

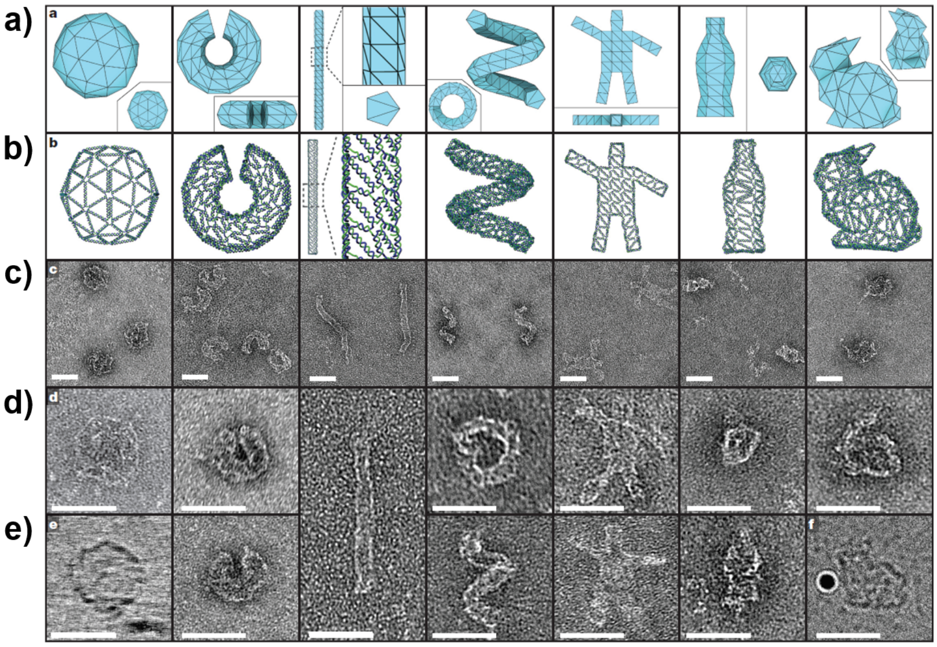

Figure 2.2: 3D-DNA origami: a) schematic representation of the 3D networks. Columns from left to right showing a ball, a nicked torus, a rod and a helix with pentagonal cross-section, a waving stickman, a bottle and a version of the Stanford Bunny. b) schematic representation of the front side of the DNA design with single DNA strands (staple strands in blue and scaffold in green). c)–e) dry transmission electron microscopy (except ball and bunny, e) and f)) of the structures with c) 250 nm×250 nm size, d) and e) 100 nm×100 nm (exception of the pentagonal bar at 200 nm×100 nm). e) and f) the ball and bunny are imaged using cryo-electron microscopy (gold particles for alignment) scale bars are 50 nm [62]. Reprinted by permission from Springer Nature: Nature: nature DNA rendering of polyhedral meshes at the nanoscale, Erik Benson *et al.*, (2015).

In this case, the network must be chosen so that the polygonal framework gets a corresponding rigidity. Each edge is represented by a double helix, which also allows larger structures but requires as little DNA as possible. Depending on the construct, some meshes may require two helices. Figure 2.2 shows some of these three-dimensional polygonal structures, such as the Stanford bunny. These structures have flexibility and the cavity structure allows generation of various reticulated 3D DNA origami designs.

2.2 Arrangement of functional groups via spatial addressability of DNA origami

Three years after the publication of Rothemund, Kuzyk *et al.* demonstrated in 2009 the use of the prepared DNA origami as substrates for protein assembly with streptavidin (SAv) as a marker for

Atomic Force Microscope (AFM) imaging [12]. The authors mention two methods for preparing the DNA origami and protein attachment to the modified oligonucleotides.

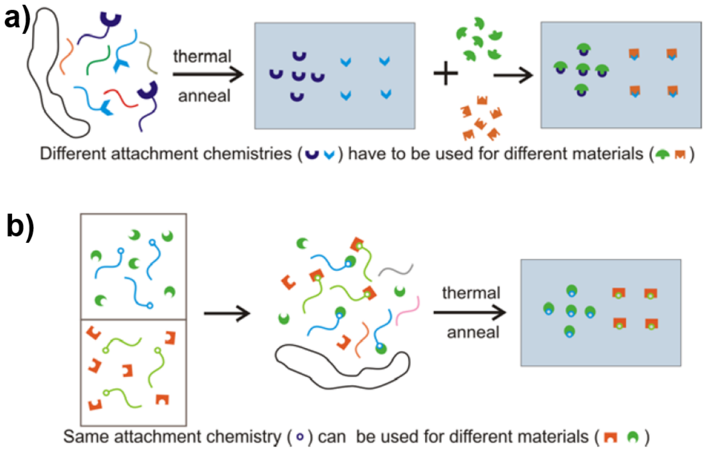
a)
thermal
anneal
+
Different attachment chemistries ( ) have to be used for different materials ( )
b)
thermal
anneal
Same attachment chemistry ( ) can be used for different materials ( )

Figure 2.3: Schematic of two processes to prepare DNA origami with attached proteins. a) a two-step process for the production of functionalized DNA origami with subsequent protein attachment, b) a one-step manufacturing process, simultaneous assembly of DNA and proteins to protein-bound origami [12]

Figure 2.3 a) shows how a ssDNA with modified and unmodified staple strands is first hybridized to a functionalized origami using a temperature program. In a second step, proteins that bind with the modifications are added. Figure 2.3 b) depicts a faster procedure. Here, the desired proteins are first bound in solution to the modified staple strands. Subsequently, this solution is combined with the ssDNA which forms the framework of the origami and the unmodified staple strands. For the obtained solution, a temperature program similar to that in a) is used to assemble the DNA origami with the desired modifications and proteins at the previously defined points. In contrast to a), there is no need for a subsequent step for the binding of the proteins to the modifications [12]. The advantage of the one-step process is that the same ligands can be used for the attachment of the proteins to the modified oligonucleotides. This allows e.g. also incorporation of different proteins that require the same ligands for optimal binding, for example SAv and avidin. A disadvantage is the limited temperature stability of the proteins. While the temperature program for the two-stage process is started at approximately 90°C, the single-stage process requires considerably lower temperatures of the order of 70°C so that the proteins used do not denature. This usually leads to lower assembly yields.

Early studies of the binding of biomolecules are based on a targeted structuring of a substrate on which the binding is then investigated using AFM. Thus, Mazzola and Fodor [63] biotinylated a lithographically generated surface array and subsequently investigated the binding of SAv to the biotinylated surface. However, the exact nature of a single bond can not be tested on such systems, since the control over binding chemistry between Bt and SAv can not be guaranteed. In this method both monodentate bonds and bidentate bonds are formed, whose binding affinity can not be considered separately and thus the affinities can not be determined [64]. In contrast, the oligonucleotides, which serve as staple strands for the creation of DNA origami structures, can be equipped relatively simply with individual biomolecules such as Bt or its derivatives (Figure 2.4) [12, 65]. As each staple strand can be localized only at a single point in the finished origami because of its unique sequence, one can use the origami structures relatively well for observing binding processes at the level of single molecules [57].

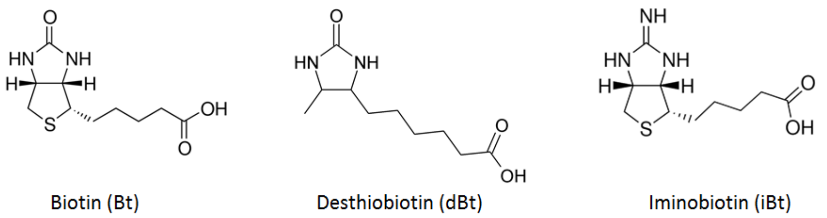

Figure 2.4: Structural representation of Bt and its derivatives with the corresponding dissociation constant to SAv with 10^{-14} mol/l for Bt [66], with 10^{-11} mol/l for desthiobiotin (dBt) [67] and with 10^{-5} mol/l for iminobiotin (iBt) [68].

For example, modified rectangular DNA origami can be used to perform aptamer protein binding distance measurements at the single-molecule level. For this purpose, thrombin was used, which binds from previous investigation, aptamers with a distance of 5.3 nm from each other. The DNA origami was modified with two different protein-binding aptamers, as shown in Figure 2.5 a). In this case, Figure 2.5 a) and b) show the variation of the distances of the aptamers to each other in green and blue markings. These aptamers each bind to opposite positions of the thrombin (about 4 nm in diameter). At distances significantly different from 5.8 nm, hardly any thrombin binding at the aptamer positions could be observed. The protein binds to heteroaptamers, but not at the positions of 20.7 nm distance as shown in the zooms in Figure 2.5 c) and d) [69].

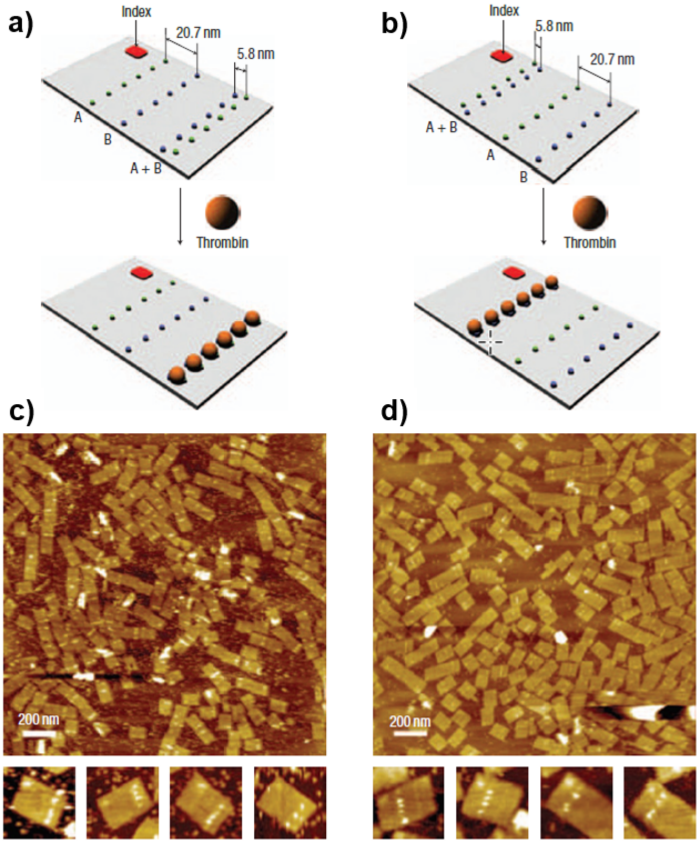

Figure 2.5: Schematic illustration of modified DNA origami rectangles two sorts of modifications. The green markers show aptamer apt-A and the blue markers show apt-B. Scheme a) and b) investigated the positional effects. The positions of apt-A and apt-B were changed. AFM images of the schematically represented origami are shown in c) and d), the size of the zooms is 150 x150 nm^2 [69]. Reprinted by permission from Springer Nature: Nature: nature nanotechnology Self-assembled DNA nanostructures for distance-dependent multivalent ligand–protein binding, Sherri Rinker *et al.*, (2008).

In the work of Voigt *et al.* [59] two-dimensional origami with a size of 100×70 nm^2 were prepared from the viral genome M13mp18 and more than 200 synthesized oligonucleotides. The origami were functionalized at 12 specific positions with Bt-modified oligonucleotides and immobilized on a mica substrate. In order to make the modified sites clearly visible in the AFM, SAv was used as a marker for the specific sites. Since SAv binds strongly to Bt and is large enough to be easily detected in the nanometer range, it is well suited for this process. Investigation of 80 fully assembled origami revealed an SAv-Bt binding probability of 84%.

The modified oligonucleotides on the origami were prepared with three different linker groups A, B and C, which then connect corresponding Bt modifications to the origami surface as depicted in Figure 2.6 a). Four of these linkers (type A) consist of the Bt modification with a non-cleavable oligonucleotide strand. Four additional linkers (type B) have a cleavable disulfide bridge in the oligonucleotide strand. The last four linkers (type C) each have an electron-rich 1,2*bis*(alkylthio)ethene sequence. In Figure 2.6 b) it is shown graphically how the respective linker types are attacked by different groups to selectively destroy the defined bonds.

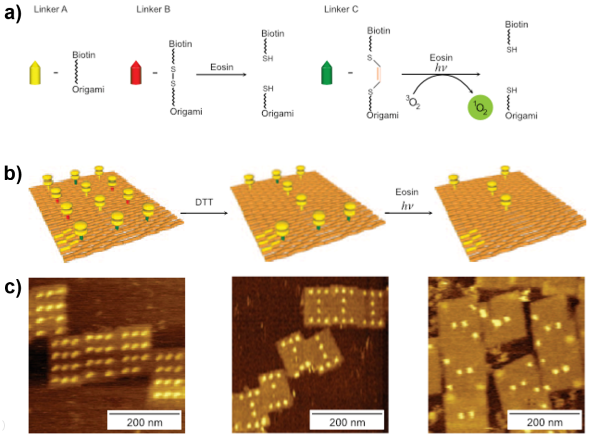

Figure 2.6: Schematic illustration of a DNA origami with selectively removable modifications. a) Illustrated linker A (modified oligonucleotide), linker B (cleavable disulfide bridge) and linker C (cleavable 1,2*bis*(alkylthio)ethene electron-rich sequence), b) schematic representation of the linker Bt-SAv interaction on a DNA origami, c) AFM image: on the left side in the untreated state with SAv, in the middle after cleavage of the disulfide bridges and on the right side a picture after the photochemical cleavage of the electron-rich sequence [59]. Reprinted by permission from Springer Nature: Nature: nature nanotechnology Single-molecule chemical reactions on DNA origami, Niels V. Voigt et al, (2010).

Using SAv as a marker, these reactions could be tracked in the AFM, as shown in Figure 2.6 c). First, all functionalized positions on the origami are visible. After incubation with 1,4-dithiothreitol (DTT) for 6 h, the disulfide bridges of linker B were chemically broken. The AFM images in the middle of Figure 2.6 shows ”I” - formation on the DNA origami. In the second step, the sample is incubated with eosin and irradiated with white light for 60 min. After irradiation, the AFM images of the sample show only the type A linker in ”Y” formations on the origami. The authors have thus shown that the exact position of the reactive functional groups on the DNA origami can be determined as a substrate, and each reaction step can be monitored with AFM images [59]. With this method a variety of functional groups can be introduced into an origami system and further reactions can be carried out on the origami substrates. The programmability of such biological systems opens up a variety of applications in various fields of research, such as structural biology [53], molecular sensing [70] and nanotechnology in general [56]. In 2012, Wong *et al.* [65] also explored the programmability of reversible processes for the assembly of functionalized groups on origami substrates. In this work, Bt and dBt-SAv modified staple strands were used on origami substrates. Using electrophoresis

(**E**lectrophoretic **M**obility **S**hift **A**ssay EMSA), the behavior of Bt- and dBt-modified DNA strands was first investigated with SAv (see Figure 2.7). The Bt and dBt staple strands were incubated in solution with SAv for 2 h each. The solutions were then added overnight with Bt (5 nM). After each process step, samples were taken and analyzed by EMSA. Thus, the altered molecular weight of the staple strands could be examined after each process step (see Figure 2.7 b)). Lanes (1) and (2) show the Bt and dBt DNA strands with a relatively small molecular weight. In the next step, these modified strands were incubated with SAv, which manifests itself in an increased molecular weight as seen in lanes (3) and (4). With the addition of free Bt, the weight of the Bt-SAv modified strand increased slightly (lane (5)) while the dBt-SAv strand decreased in weight because the affinity of SAv to Bt is much higher than the affinity for dBt. As a result, Bt displaces the already bound dBt-modified oligonucleotide strand [65].

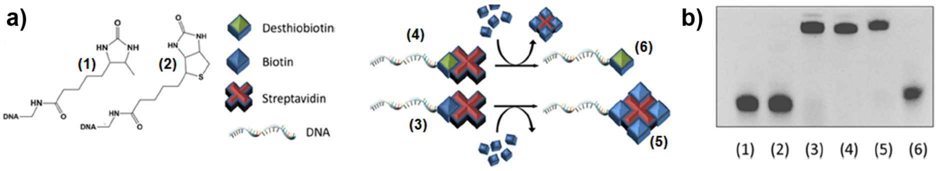

Figure 2.7: Illustration of an EMSA experiment to demonstrate successful binding of SAv to DNA strands modified with Bt derivates. a) Shows the modifications of the DNA strand as well as the reactions of the assembly of the Bt-SAv strand and the reassembly of the dBt-SAv strand with free Bt. b) recorded EMSA of Bt and dBt with SAv [65]. Reprinted with permission from N. Y. Wong et al, Nano-Encrypted Morse Code: A Versatile Approach to Programmable an Reversible Nanoscale Assembly and Disassembly, J. Am. Chem. Soc. 135. Copyright 2013 American Chemical society.

After studying the behavior, the authors used a 100×70 nm^2 DNA origami [23] to generate the reversible behavior of the dBt nano-morse code on the origami.

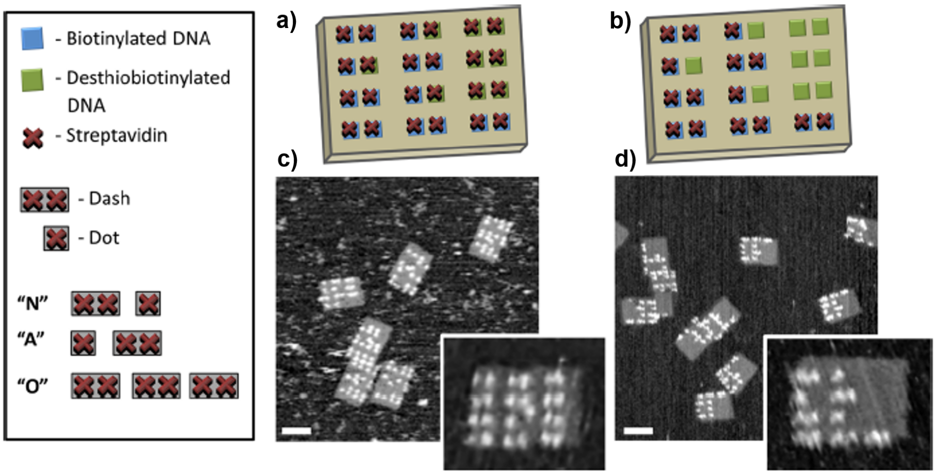

Figure 2.8: Illustration of a switchable protein pattern on a DNA origami. Design of the nano-morse symbols and the origami surface a) and b), AFM images of the functionalized origami surface c) in the ground state bound with SAv, d) obtained the Morse symbol "NANO" after Bt addition [65]. Reprinted with permission from N. Y. Wong et al, Nano-Encrypted Morse Code: A Versatile Approach to Programmable an Reversible Nanoscale Assembly and Disassembly, J. Am. Chem. Soc. 135. Copyright 2013 American Chemical society.

For the origami rectangle, 9 dBt and 15 Bt modified strands were applied at defined positions. By addition of SAv, all functionalized sites were first occupied, see Figure 2.8 a) and c). After displacement of the SAv from the dBt sites by free Bt, the morse codes on the AFM images of the origami are "NANO" in Figure 2.8 b), d). Since this is a reversible process, in the next step the free dBt modifications could be bound with SAv and then separated again with Bt. The binding probability of SAv on the modified origami was 90% for the origami shown in Figure 2.8 c). The binding probability of Bt to SAv was 95%, whereas that of dBt to SAv was only 86%. After incubation with Bt, on 8 well-preserved origami at the desired positions for the Morse code ”NANO” an occupancy rate of 96% could be determined.

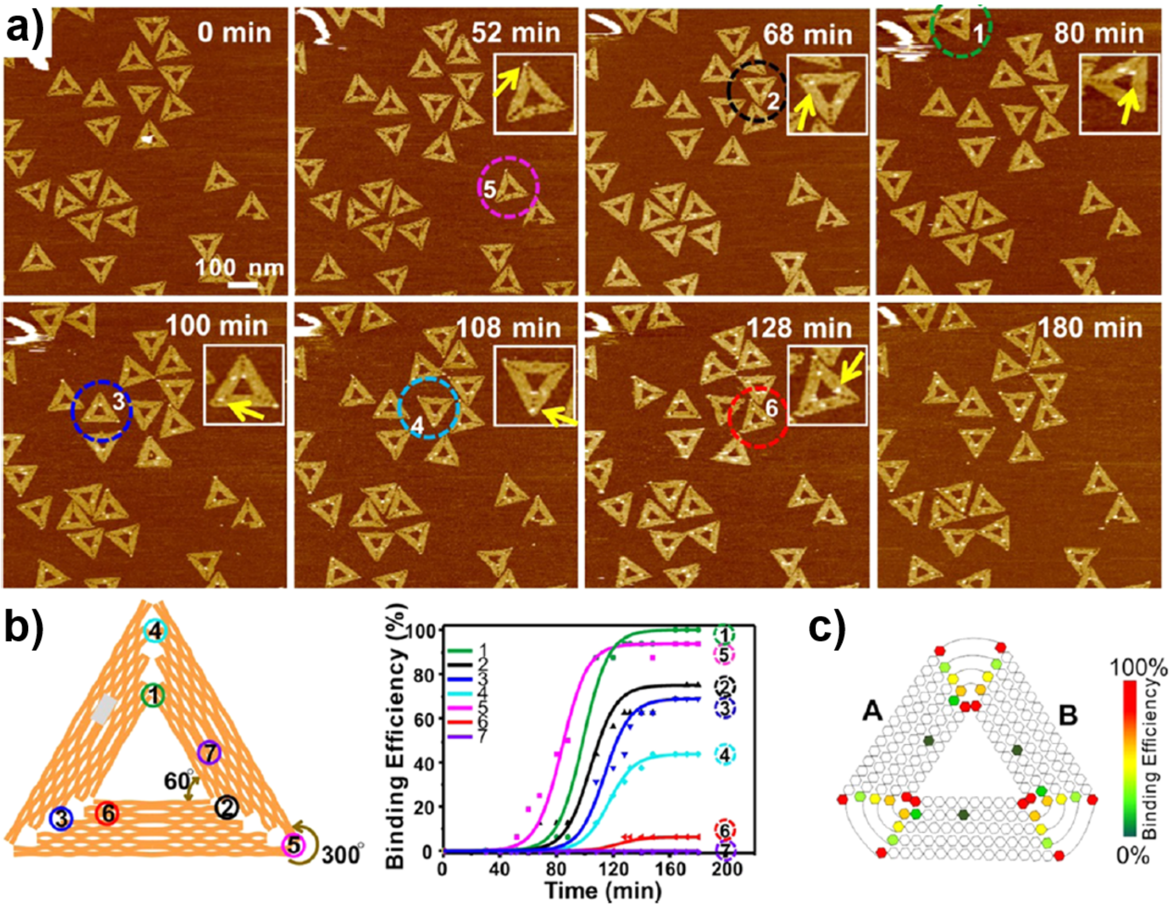

Figure 2.9: Schematic illustration of the formation of individual Bt-SAv bonds at different positions on the DNA origami. a) AFM images of Bt-SAv binding from 0–180 min incubation time on the DNA origami at room temperature. The colored circles show the correspondingly formed Bt-SAv positions. b) shows the binding efficiency between Bt and SAv of the 7 positions on the DNA origami over time. c) Scheme of the binding efficiency on the triangular DNA origami, red has a high detection efficiency, green a low detection efficiency [71]. Reprinted with permission from P. Zhang et al, Quantitative Measurement of Spatial Effects of DNA Origami on Molecular Binding Reactions Detected using Atomic Force Microscopy, ACS applied materials & interfaces 11(24). Copyright 2019 American Chemical society.

The arrangement of the modified positions on the DNA origami is not unimportant, as shown in the work of Zhang *et al.* [71]. The nonuniform spatial organization of the DNA helices at the vertices, rims, corners, and the surface of the DNA origami leads to altered local environments on the structure. The effect of the local positions was tested by different Bt-modified positions on the triangular structure by attachment of the modified positions with SAv. The modified origami were immobilized on mica and measured in a liquid cell with AFM. The time-dependent measurements were started by initiating the SAv solution (see Figure 2.9). It was found that the binding efficiency differs depending on the position on the DNA origami structure for SAv-Bt binding. Also, digoxin-modified positions on the rectangular DNA origami were probed with the antigen antibody immunoglobulin g (IgG) and led to the same conclusion. Thus, the dynamic processes were shown on different positions of the DNA origami in real time and in situ at low concentrations with AFM (Figure 2.9 a)). As a result, minor differences on the DNA origami vertex, rims, corner, and the surface can be quantitatively evaluated.

Although the AFM tip may have an influence on the system (see chapter 5.2), the results depicted in Figure 2.9 show a clear dependency of the binding efficiency on the exact position on the DNA origami surface.

In addition to the selected examples listed above, many other examples of the structural nature and fields of application of DNA origami systems can be found in the literature. The production of various DNA origami systems from 2D and 3D structures [23, 24, 29], wireframe [62], twisted and curved shapes [30, 72] as well as the software for the creation of these structures [29, 62, 73, 74], continues to evolve. Increasing the scale of production to achieve a mass-marketable product [75] or improving the long-term stability of DNA origami systems to extend application capability is also increasing research in these areas. These enhancements will also improve the existing applications. For example, in lithography [76], plasmonics [77], biosensing [78], drug delivery [79, 80], nanophotonics [81], nanorobotics [34, 82, 83] and many more.

2.3 Structural stability of DNA origami nanostructures

The structural diversity of the DNA origami is very far-reaching and provides a gigantic toolbox that grows day by day in its functions and possibilities. In the field of biophysical, biochemical materials science and biomedicine as well, the stability and flexibility of the used DNA origami plays an increasingly important role in the application [84]. In general, the DNA origami protocols are based on the tris-acetate-EDTA (TAE)-buffer solutions with magnesium chloride in the millimolar concentration range. These high levels of magnesium may interfere with investigations of enzyme activity and fluorescence emission. However, it has been commonly assumed that for DNA origami manufacturing and ensuring structural integrity, these ion concentrations are needed to suppress the electrostatic repulsion of the negatively charged backbone of the DNA double helices and stabilize the DNA Holliday junctions during assembly of the DNA origami [85].

In order to extend the boundaries of the use of DNA origami, several studies have been carried out on the stability and denaturation of DNA origami structures. DNA origami can be transferred into low magnesium buffer solutions without causing any structural damage. Also, the stability in other media is also dependent on the structural state of the DNA origami. In chapter 4.1, these phenomena are discussed in more detail. The stability of DNA origami depends on several factors, some of which are the choice of lattice types of the origami system, the compactness and the associated charge density, the resulting structure-dependent flexibility and the strain of the corresponding curvature [84].

In the work of Wang *et al.* [86], the stability of DNA origami nanotubes was investigated in buffers used for the crystallization of proteins (Figure 2.10 a)). Assembled DNA origami remained stable in catalase buffer, but a self-assembly of the DNA origami could not take place in these buffers. They tested the effects of cations, pH, protein precipitants and various buffering agents on their DNA origami system [86]. The obtained results show that DNA origami can be successfully transferred into Mg^{2+} containing 200 mM Na^{+}. Also, the origami remained stable in Tris-, HEPES-, PEPES-, and MES-buffers as well as in buffers containing various precipitating agents such as alcohols, polymers and NaCl up to concentrations of 3M at pH value range of 5–10. In biopysics, the study of protein folding behavior is increasingly being supported by use of single-molecule experiments with fluorescence techniques [87]. Therefore, it is important to examine the integrity of the DNA origami used as a substrate for this single-molecule study of proteins [84]. Urea or guanidinium chloride (GdmCl) are often used as denaturants in high concentrations [88]. In 2016 Ramakrishnan *et al.* used two-dimensional triangular DNA origami to study stability using these denaturants. Their finding was that the DNA origami remained largely intact for at least 24 h in 6 M urea and 6 M GdmCl at room temperature [89].

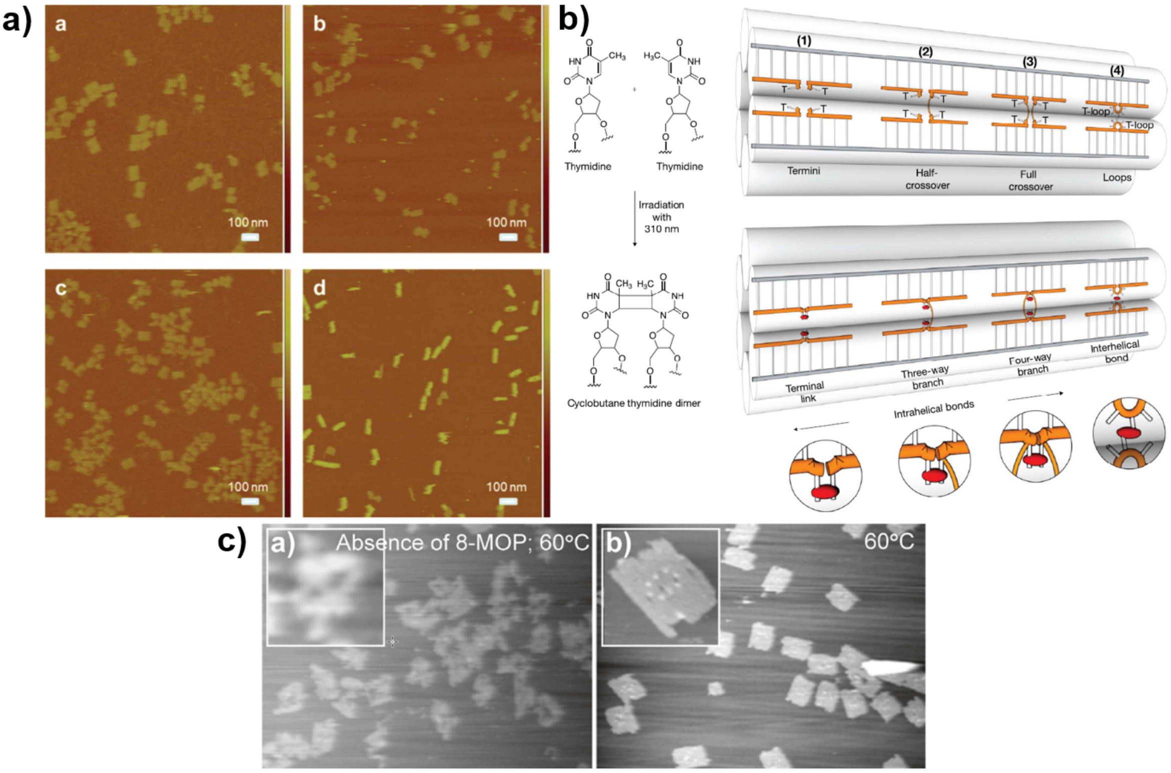

Figure 2.10: DNA origami systems which retain their structural integrity under biochemical and biophysical conditions. In a) the DNA origami nanotubes are shown in the crystallization buffers for lysozyme (a), thaumatin (b), serum albumin (c) and catalase (d) [86]. b) schematically depicts how DNA nanostructures can be connected using proximal thymidines for cross-linking. At the top left, the structure of two thymine modified structures in the ground state is shown. Bottom left cyclobutane-pyrimidine-dimer (CPD) bond after UVB irradiation. On the top right is schematically shown a 6HB DNA origami with different possibilities of the thymidine modified strands as single strand (1), at half-crossover (2), at full-crossover (3) and thymidine loops (4) before UVB irradiation [90]. Reprinted from Gerling *et al.*, Sequence-programmable covalent bonding of designed DNA assemblies. In: Science advances 4(8) (2018), DOI: 10.1126/sciadv.aau1157, CC BY-NC 4.0. At the bottom right, the CPD bonds are shown in red after UVB irradiation. c) shows DNA origami sheets at 60°C on the left without 8-MOP based photocrosslinking and on the right with crosslinking [91]. Reprinted with permission from A. Rajendran et al, Photo-cross-linking-assisted thermal stability of DNA origami structures and its application for higher-temperature self-assembly, J. Am. Chem. Soc. 133(37). Copyright 2011 American Chemical society.

Several approaches have been taken to enhance the stability of DNA origami towards environmental conditions which usually destabilize the assembled origami. For example, covalent cross-linking of DNA origami from 8-methoxypsoralen (8-MOP) with UVA irradiation (Figure 2.10 c)) can increase the melting temperature [91] as well as generate cyclobutane-pyrimidine-dimer (CPD) bonds between two thymidine modified staple strands with UVB irradiation to increase the structural stability of the DNA nanostructure (Figure 2.10 b)) [90]. These CPD-supported multilayer DNA origami objects can remain stable at 90°C and provide higher structural resistance in cryo-electron microscopy (cryo-EM). Depending on the irradiation dose, the UVB and UVC irradiation of DNA origami leads to the degradation of the DNA origami. In contrast, for UVA irradiation the DNA origami show no characteristic damage even at a dose of 200 kJ/m^2 [92].

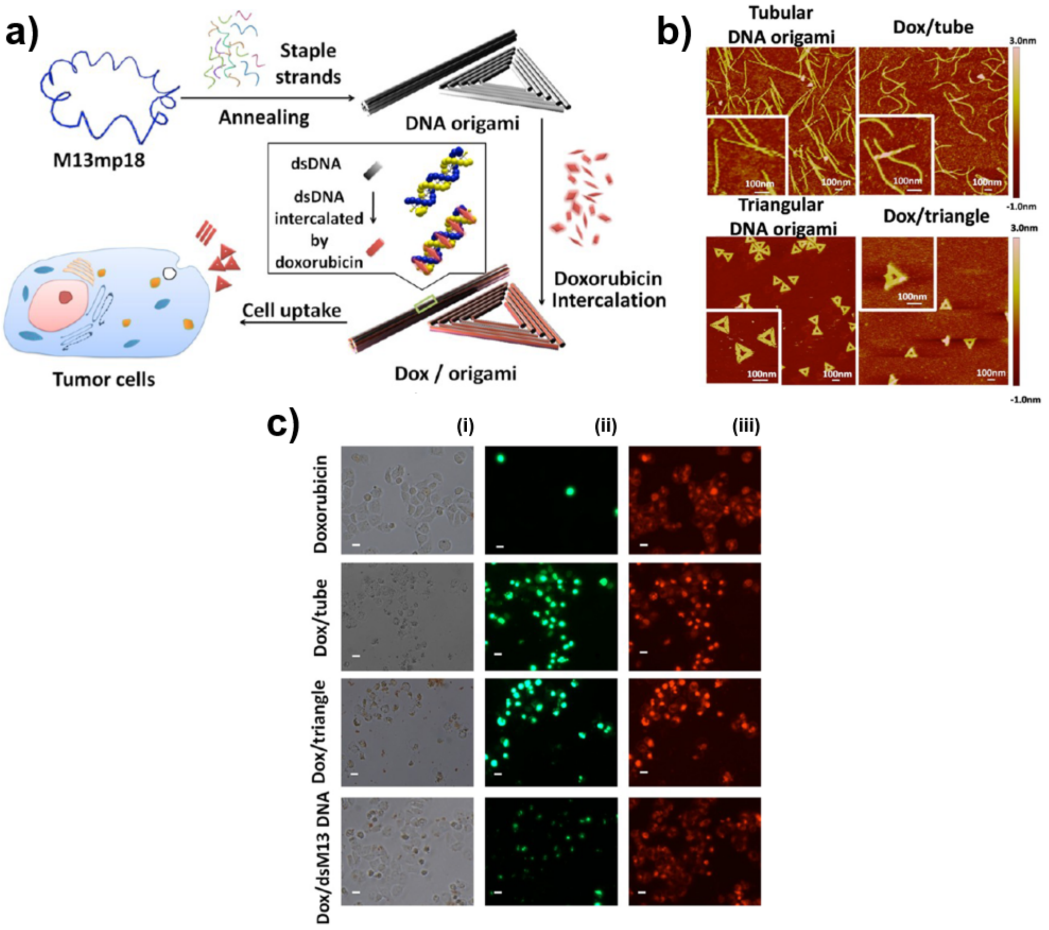
a)
M13mp18
Staple strands
Annealing
DNA origami
dsDNA
dsDNA intercalated by doxorubicin
Doxorubicin Intercalation
Cell uptake
Tumor cells
Dox / origami
b)
Tubular DNA origami
Dox/tube
Triangular DNA origami
Dox/triangle
100nm
3.0nm
-1.0nm
c)
(i)
(ii)
(iii)
Doxorubicin
Dox/tube
Dox/triangle
Dox/dsM13 DNA

Figure 2.11: a) shows the scheme of DNA origami and doxorubicin origami delivery system assembly. After incubation with doxorubicin, the drug-loaded DNA nanostructure delivery systems were administered to regular human breast adenocarcinoma cancer cells (reg-MCF7) as well as doxorubicin-resistant (res-MCF7) cells, and the effects were analyzed. b) shows AFM images of triangular and tubular DNA origami before and after doxorubicin intercalation. c) shows the cytotoxicity of doxorubicin-loaded DNA origami on both cell sublines. Panel (i) bright field microscopy images, panel (ii) shows fluorescence image of SytoX Green stained res-MCF7 cells whereas panel (iii) shows fluorescence of doxorubicin. Image scale bars are 20 μm. From top to bottom the images indicate the uptake of free doxorubicin, doxorubicin bound to a DNA tube, doxorubicin bound DNA origami triangles and dsM13 bound doxorubicin. Doxorubicin-loaded DNA origami structures are more effective at killing doxorubicin-resistant (res-MCF7) cells than free doxorubicin and doxorubincin-loaded dsDNA [93]. Reprinted with permission from Q. Jiang et al, DNA origami as a carrier for circumvention of drug resistance, J. Am. Chem. Soc. 134(32). Copyright 2012 American Chemical society.

In contrast to other nanoparticle based drug delivery systems, DNA origami nanostructures are completely biocompatible and are fixed by their structural specification in shape and size. The addressability on the DNA origami surface can also be precisely defined by functionalization with modified staple strands at defined positions and individual molecules attached to the DNA nanostructures. Furthermore, by intercalation of the incorporated molecules in the DNA origami structure or with loading of an active substance by DNA conjugation [84] the origami can also be used as a transport system. The intercalation of doxorubicin loaded DNA origami triangles and tubes into tumor cells has been extensively studied in literature. An example for an in vitro study by Jiang *et al.* can be found in [93] (see Figure 2.11). The successful application of a similar system in vivo in living mice has been performed, e.g. by Zhang *et al.* [36]. However, the use of DNA origami in cellular environments is difficult. The structural integrity suffers from the environmental conditions. Working in vitro one has decent control over the environmental conditions, however, origami are exposed to the cell and tissue cultures. Aiming for in vivo applications one has to consider additional aspects such as the physiological cation concentrations, the pH ranges and their possible variations in the different compartments of a cell. The degradation of DNA in the cells plays a major role here. Zhang *et al.* [94] and Samejima *et al.* [95] have considered with the degradation of genomic tissue homeostasis DNA in living organisms. The degradation of DNA occurs through the participation of different nucleases in the cell nucleus, in the cytoplasm and in the extracellular space [84]. Examination of some nucleases revealed that DNase I and T7 endonuclease I degrade DNA origami for 18-, 24-, and 32-helix bundles [96]. In general, DNA origami are more resistant to DNase I (abundance in blood and plasma) than the normally formed double-stranded DNA, but how much the resistance increases depends on the assembled DNA origami structure. The more densely packed and compact the DNA structures are, the longer these structures hold the degradation of DNase I [84]. For the stability of DNA origami, the enzymes in in vivo research are still a major issue that will continue to be worked on. Further investigations were carried out on the effects of DNA origami at low magnesium concentrations and in the presence of nucleases in tissue culture media [97]. Depending on the DNA origami system, they may or may not remain stable in **F**etal **B**ovine **S**erum (FBS). The 6HB origami remained stable for several hours in 10% FBS heat-inactivated containing nuclease [97] and wireframe-based DNA origami in phosphate buffered saline (PBS) and in **D**ulbecco's **M**odified **E**agle **M**edia (DMEM) are stable in combination with FBS [62, 98]. Multilayer origami structures in DMEM with FBS show a stable state [99], whereas, box-shaped 3D DNA origami nanostructures are completely unstable in the presence of FBS [100]. Stability of DNA origami in extracellular and intracellular environments is not the only limiting factor for drug delivery systems. The success of these drug delivery systems also depends on how well the DNA origami can be transfected into the cell to reach the desired location in the cell. Structures that can not be internalized are degraded by DNase I in the extracellular domain. However, if a transfection of the structures into the cell has worked, they could encounter the lysosomal enzymes from which they can also be degraded [84]. Therefore, DNA origami nanotube studies have been conducted on stability and distribution in breast cancer cells, remaining intact in the lysosomes for up to 24 h [101]. In order to increase the stability of DNA nanostructures in these areas, the structures were coated with virus capsid proteins [102], virus-mimicking lipid bilayers [103], encapsulated systems with bovine serum albumin (BSA), protein-polymer and protein-dendron conjugates [104–107], cationic polymers such as polyethylene glycol (PEG)-oligolysines and PEG-polylysines, chitosan, polyethyleneimine (PEI), and PEG-poly (2-dimethylaminoethyl methacrylate (PEG-PDMAEMA) copolymers [99, 108–111]. These coatings not only protect the DNA nanostructure but also the encapsulated drug and are more resistant to degradation by DNase I [99, 103, 106, 107, 111] and low-salt conditions [84, 99, 106, 108, 111].

Next to drug delivery, another field of application which requires stability of the assembled origami is material sciences. In this field the demand for novel substrates is growing, so that the use of DNA origami nanostructures increases more and more. They are used as matrices and lithographic masks especially in inorganic materials [112–119] but also in biological [120–123] and organic materials [124–127] transfer the nanostructured form [84]. In some works, the shape of the DNA origami template is taken directly, but the structural stability is not so important. However, in multi-step transfer systems, where the structure is, for example, metalized and etched [118], the structural integrity of the DNA origami plays a major role. Any coating of DNA origami nanostructures can change shape and size, and depending on how complex the systems are, impurities can creep into the system that could potentially damage the DNA origami structure. Interestingly, despite the stability problems mentioned above, DNA origami systems turned out to be incredibly robust against a number of harsh treatments, e.g. mica adsorbed DNA origami can be exposed to air for 45 minutes at a temperature of 150°C without structural damage and degrade only at 250°C [128]. Further chemical and physical conditions have been investigated in the work of Kim *et al.* [129]. The adsorbed DNA origami retained their structure in air and under argon atmosphere for 10 min at 200°C. Upon exposure of the DNA origami to the organic solvents hexane, ethanol and toluene for up to 24 hours, the DNA origami remained stable. The use of deionized water on SiO_2-adsorbed DNA origami structures resulted in the desorption and damage of DNA origami. Using NaCl solution, a similar effect on DNA origami was seen as with deionized water, but with higher salt deposits on the sample. Upon exposure to alkaline and acidic aqueous solutions, the DNA origami were shown to maintain their structural integrity in the range of pH 4 to pH 11.

Due to the oxidative effect with UV/ozone, the DNA origami lasted 5 minutes until they lost their original shape. Thus, a high stability of DNA origami for lithographic applications and other material science areas is given.

Normally high magnesium concentrations of 0.1-0.5 M are used on SiO_2 surfaces to immobilize DNA origami [119, 130–132]. With the high salt concentrations, salt residues can remain, which could disturb the subsequent further processing of the surface. In order to reduce salt concentrations on surfaces, Linko *et al.*'s work by spray application used lower concentrated but homogeneously distributed DNA origami on the sample surface with pure water as the medium to be applied so that the final concentration of magnesium is in the μM range. After applying DNA origami with 3 bar and a salt-free medium, the DNA origami remained intact [133]. This finding is somewhat contradictory to the earlier findings that low Mg concentrations cause structural damage to the DNA origami. A part of this work is aimed at resolving this contradiction.

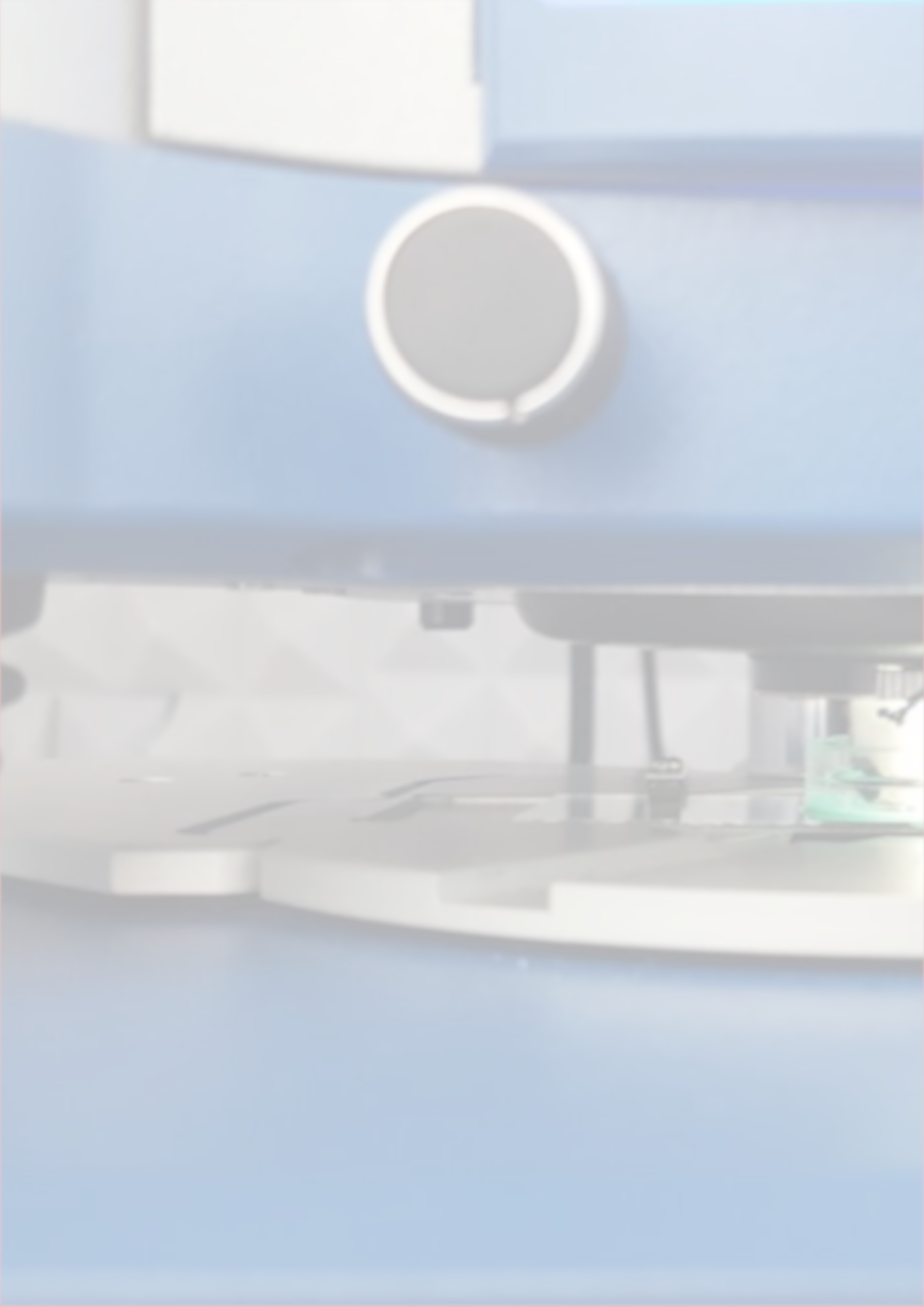

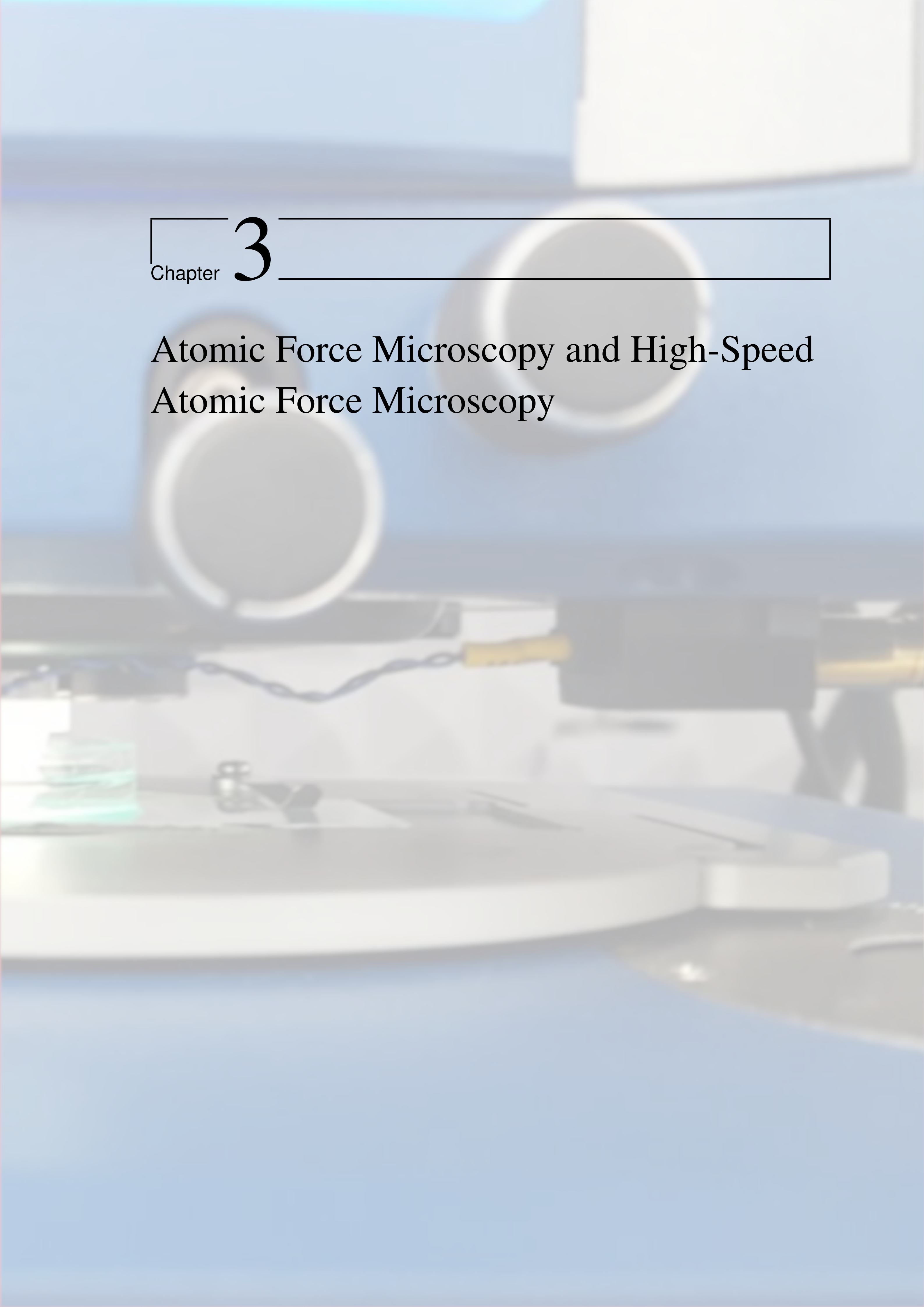

Chapter 3

Atomic Force Microscopy and High-Speed Atomic Force Microscopy

3.1 Atomic Force Microscope

The AFM was introduced in 1986 by Binnig, Quate, and Gerber [134]. The AFM is a very flexible measuring instrument and is well suited for single-molecule investigations since on the one hand biomolecules with a size of ∼5-10 nm can be well resolved, and on the other hand measurements in solution are possible [135].

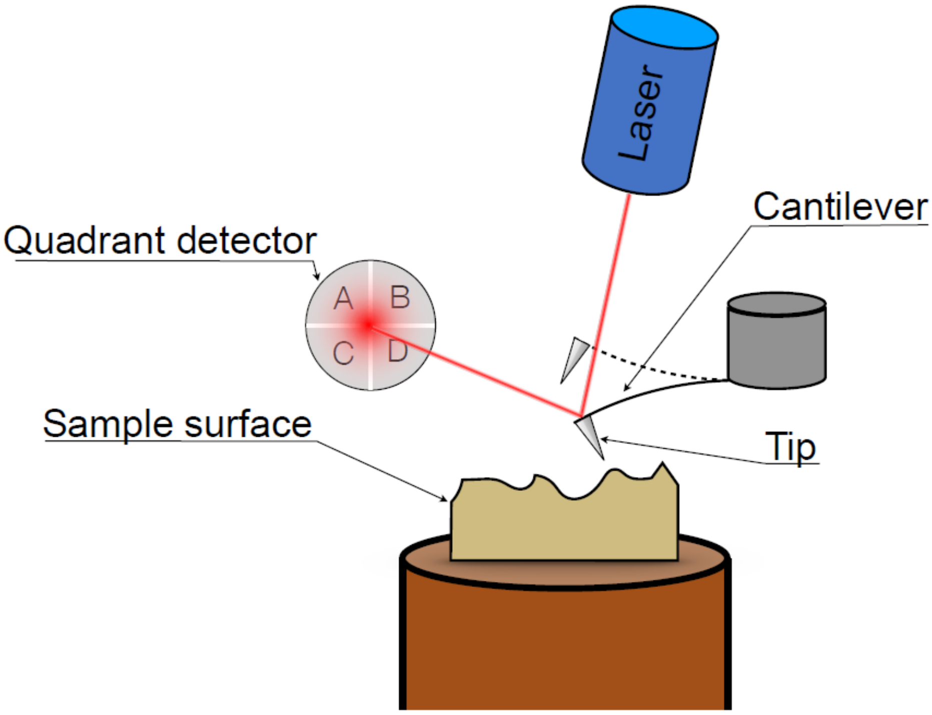

Figure 3.1: Schematic of the measurement technique of an AFM.

In general, the AFM measures the forces between a cantilever tip and the sample surface. These may be Pauli repulsion, chemical, electrostatic, magnetic, and van der Waals forces. Scanning the sample, the forces are registered by deflections of the cantilever by means of a laser beam, which is reflected by the cantilever onto a position sensitive photodetector, i.e. a quadrant photodetector (see Figure 3.1). The signals from the photodetector can be analyzed to obtain topological information about the sample from vertical deflection of the laser beam. Further more the lateral deflection provides information about the torque acting on the cantilever.

There are different modes for creating AFM images, each of which outputs different information about the sample surface. Figure 3.2 shows a diagram of the force exerted on the cantilever tip as a function of the distance to the sample surface. In addition, the figure shows the three most commonly used working modes of AFMs. In contact mode, repulsive forces act on the cantilever tip. This is the case when there is contact with the sample surface. In non-contact mode, mainly attractive forces act and in intermittent contact mode or tapping mode both attractive and repulsive forces.

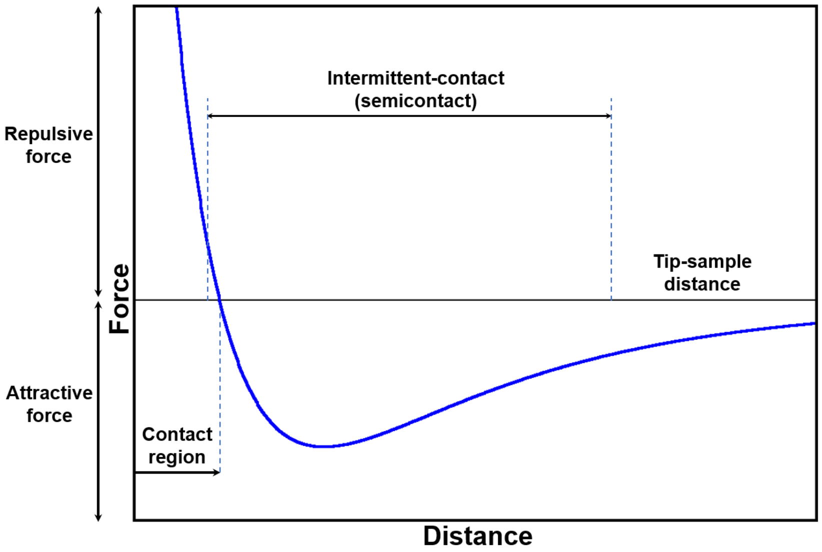

Figure 3.2: Schematic curve of the force between the AFM tip and the sample indicating the regions of the most commonly used AFM modes.

In contact mode, one of the first methods of AF-Microscopy, the cantilever tip is located on the sample surface during the entire measuring time. This mode reveals most accurate information about the surface topography. Due to the permanent contact between tip and sample, this mode primarily gives a map of the repulsive forces and no information about attractive forces. In the simplest version, without a feedback loop, the sample is scanned with a constant z position of the cantilever and the cantilever deflection is recorded as a function of the x and y coordinates.

In general, the contact mode is used for hard and relatively flat sample surfaces. However, this method has some disadvantages. The most obvious disadvantage is that both, the cantilever and sample, are easily damaged when scanning across edges on the sample surface. Adhesive or frictional forces can also wear the tip or degrade the topographical image. Since the forces occurring in this mode are relatively large, depending on the nature and hardness of the sample, either the sample itself or the cantilever tip can be damaged during the recording. For soft, elastic and easily destructible samples, the methods Intermittent-Contact or Non-Contact-Mode are much better suited than the Contact-Mode.

In the intermittent contact mode, the cantilever is excited to a vibration with a frequency close to its own resonance frequency. The tip oscillates close to the surface of the sample. The oscillation amplitude determines how close the tip approaches the sample surface. Due to the limited direct contact with the sample, this working mode is also well suited for the examination of soft, elastic and adhesive samples. When scanning the sample, the oscillation amplitude and/or the phase of the oscillation of the tip may change due to varying interactions with the sample surface. A change in the oscillation amplitude results primarily directly from the changed topography, a change in the phase primarily from altered material properties of the sample. If measurements are made in air in this working mode, additional aspects must be considered in addition to the interactions between the sample and the cantilever tip. Unless it is a highly hydrophobic sample, a thin film of water will be deposited on the sample from the humidity. If the cantilever tip breaks through the surface of the film, attractive capillary forces are created. In the event that the restoring force due to the deformation of the cantilever is not large enough to compensate for these forces, the sample is scanned unintentionally in a kind of contact mode. For this reason, the spring constants for cantilevers for measurements in air are usually several orders of magnitude greater than for cantilevers designed for measurements in contact mode or measurements in intermittent contact mode in liquid.

The non-contact mode is very similar to the intermittent contact mode. Again, the cantilever is excited to a vibration near its resonance frequency, but with a much smaller amplitude than the intermittent contact mode. In this working mode, the long-range forces, van der Waals and electrostatic forces between the atoms in the cantilever and on the sample surface are recorded. The occurring forces cause a detectable shift in the frequency of the oscillating cantilever. Because the cantilever tip does not come into direct contact with the sample surface, the surface region with which the cantilever tip effectively interacts is minimized. Thus, this working mode has the potential of a particularly high resolution. However, measurements in air, similar to the intermittent contact mode, have the problem of a water film on the parts of the sample surface which are not highly hydrophobic. It may happen that the thickness of the liquid film exceeds the range of the investigated forces. In combination with the small oscillation amplitude, this can in practice lead to a significantly reduced surface resolution.

All three working modes can be operated with and without feedback loop. The only difference is that without the feedback loop, the respective measurement signal, in contact mode the bending of the cantilever, is recorded in a location-dependent manner and subsequently converted into a height profile. When using a feedback loop, the signal level is kept constant by continuously adjusting the z-position of the cantilever. Recording the corrections to the z-position of the cantilever, one directly obtains the respective height profile.

The tip-sample interaction manifests in different ways. Considering the model of a simple harmonic oscillator, an applied external force may lead to a change of amplitude, phase, and resonance frequency. Assuming a sinusoidal cantilever motion, the time resolved signal for the vertical deflection $S(t)$ in units of V may be written as

$$S(t) = A(t)\sin\left(\omega_0 t + \varphi(t)\right) \tag{3.1}$$

where $A(t)$ denotes a time-dependent amplitude, ω_0 the angular frequency of the cantilever motion, and $\varphi(t)$ a time-dependent phase shift. This signal can be multiplied by a dimensionless reference signal $R(t)$, which is typically synchronized with the cantilever excitation. The reference signal may be expressed as

$$R(t) = 2\sin\left(\omega_0 t + \phi\right) \tag{3.2}$$

where ϕ denotes an adjustable phase shift of the reference signal. The multiplied signal $M(t) = S(t)R(t)$ is then of the form

$$M(t) = A(t)\left[\cos\left(\varphi(t) - \phi\right) - \cos\left(2\omega_0 t + \varphi(t) + \phi\right)\right] \tag{3.3}$$

and has the physical unit V. Applying a low pass filter and adjusting the phase ϕ of the reference signal yields a slowly varying signal $\tilde{M}(t)$ of the form

$$\tilde{M}(t) \sim A(t)\cos\left(\Delta\varphi(t)\right) \tag{3.4}$$

where the phase difference $\Delta\varphi(t)$ is caused by the tip-sample interaction. This phase signal is typically used to visualize material contrasts.

A thing that should be noted is that the recorded image is always a convolution of the actual sample topography and the shape of the cantilever tip. To this end, the wear and contamination of the tip can worsen the resolution during a measurement. In principle, the resolution of the images gets better, the sharper the tip is.

3.2 Suitable substrate surfaces for AFM imaging

For a good AFM or High-Speed Atomic Force Microscope (HS-AFM) image, a correspondingly good substrate surface is required. The requirement for such a substrate surface is a flat or atomically smooth surface. For the dynamic measurement of proteins, the substrate surface should not bind strongly to the system under investigation, so as not to interfere with possible reaction mechanisms. Mica surfaces are often used for the measurement of biological systems, but also planar lipid bilayer (PLB) surfaces and surfaces of biotin-containing PLB were used for dynamic AFM imaging [136].

3.2.1 Mica surface

Mica, in its natural form muscovite or its synthetic form the fluorophlogopite, is very often used as a substrate for AFM recordings because of its atomically smooth surface over a larger area and its low cost. It has a net negative charge (hydrophilic) and by adding appropriate monovalent or divalent ions and/or adjusting the pH value, the adsorption of DNA and proteins on mica can be actively controlled [136]. By changing the divalent cation concentration of Ni^{2+} and Mg^{2+} [137] or increased addition of Na^{+} [138], the formation of DNA origami can be controlled in a way that allows two-dimensional lattice formation on the mica surface. Likewise, the affinity of proteins for monovalent cations such as Li^{+}, Na^{+}, and K^{+} on mica is affected [139].

3.2.2 Planar lipid bilayer (PLB) surface

With liposomes, planar lipid bilayer surfaces can be assembled on mica [140]. The PLB surfaces can be attached by attaching biotin or nickel-nitrilotriacetic acid (Ni-NTA) to the head groups for specific immobilization. Neutral charged PLB surfaces can protect against nonspecific protein deposition on a sample surface. Electrostatic immobilization with PLB surfaces can be created by charged head groups of the lipids, thus a charge density or polarity on a surface can be more easily varied than with commercial mica surfaces [136].

3.2.3 Langmuir-Blodgett-film and -Schaefer-film of an organic mono- and Multilayer

The Langmuir-Blodgett (LB) and Langmuir-Schaefer (LS) methods are commonly used techniques for deposition of defined organic mono- and multilayers. In the following a comprising description of these methods will be given. A more detailed description may be found, e.g. in [141]. First, a Langmuir film is produced in which a solution of amphiphilic organic molecules is distributed on the surface of a liquid. After evaporation of the solvent, the compression process begins using a mobile barrier which compresses the organic molecules at the air-liquid interface. During compression, the surface pressure of the process allows isothermal monitoring of phase formation and transitions. After the formation of a stable monolayer at the air-liquid interface, the resulting Langmuir film can be transferred onto a substrate. The so-called LB-film may, in principle, be formed in three different ways. Two of which typically result in a monolayer. Either the substrate is initially in air and then immersed through the film, or it is initially located in the sub-phase and then emerged. The last way combines a number of immersion/emersion cycles and results in the deposition of defined multilayers on the given substrate. Different functionalizations of the surface of the substrate can result from the deposition during immersion and/or surfacing. The SL-film is formed quite similarly by bringing the substrate in horizontal position into contact with the liquid surface and removing it from the liquid surface. These methods are used to form controllable organic mono- up to multilayers on substrates which can be functionalized in various ways, such as conductive, semiconductive films to monomolecular layers between two electrodes.

3.3 High-Speed Atomic Force Microscope (HS-AFM)

By now, HS-AFM has become an established method for investigation of biological and molecular processes which take place on sub-second time scales. The following sections cover the central developments towards HS-AFM measurements following two publications of Ando *et al.* [136, 142]. Especially for specific details on the electronics of the feedback loop and the respective theoretical background, the reader is referred to these two publications and references cited therein.

With a conventional AFM, the dynamic tracking of biological processes, in the second range or less, is not possible. The development of the HS-AFM enables observation of the dynamics of molecules, as well as larger systems, to better understand their structural change and interaction with other molecules over time. At imaging rates in the range of a few frames/s, ideally up to a few hundred lines/s (which corresponds to approximately 30 frames/s), it is much easier to track the dynamic interactions of purified proteins on substrates under physiological conditions. Once the molecules are bound in a form, such as on substrate, their interaction with each other is inhibited and they may be investigated on a single molecule level. At the same time this implies that the forces available for interactions are weak. These protein-protein interaction forces lie in the range of 1 pN to 100 pN. A high sensitivity of the AFM tip which is maintained during the measurement is important in order to allow imaging at interaction forces between tip and sample on the order of 1 pN and below. However, it should be noted that the mechanical quantity that can affect the sample is not the force itself but is a force pulse as far as the intermittent contact mode is concerned. Here the product of the force and time over which this force acts is considered. Ando *et al.* also point out that if the tip is acting at high speed in the intermittent contact mode, the time of the force action is short and thus has a large peak force (>20 pN) and that would not significantly affect the sample. In Chapter 5.2, tip effects in intermittent contact mode are examined more closely and a system for quantifying these effects in HS-AFM measurements is presented.

3.3.1 Feedback bandwidth

When using the HS-AFM, it is helpful to understand basic assumptions about how each component affects scan speed and imaging rate. In a previous work a theoretical consideration of the dependence of the feedback bandwidth was shown for the intermittent mode [143], as well as the effect of the dynamic tip-sample interaction [144]. But for a practical consideration that is not enough. At first, the image acquisition time and the feedback bandwidth shall be examined more closely. It is assumed that if an image is taken in a time period T over a scan range of $W \times W$ nm^2 with N scan lines, then the velocity V_s in the x-direction is $V_s = 2WN/T$. Assuming that the sample, in Figure 3.3 a), is sinusoidal and has a periodicity of λ, the scan velocity V_s requires a feedback operation with a frequency of $f = V_s/\lambda$ to maintain the tip to sample distance. This estimate applies strictly to a sample with a periodic surface structure, as shown in Figure 3.3 b).

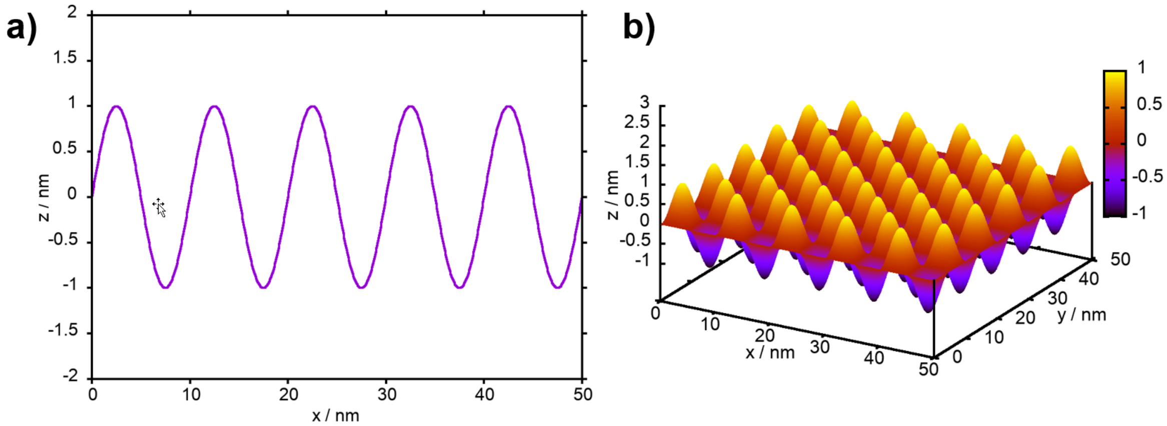

Figure 3.3: Examples for perfectly sinusoidal surfaces in 1D and 2D: In a) the sinusoidal representation of a sample surface is simulated in the x-direction, b) shows an ideal periodic surface structure with a sinusoidal shape in the x- and y-direction of $\lambda = 10$ nm and an area of 50×50 nm.

The feedback bandwidth f_B should be greater than or equal to the frequency f. This condition may be expressed as in equation 3.5. From this relation it becomes clear, that the required feedback bandwidth is inversely proportional to the desired imaging time T;

$$f_B \geq \frac{2WN}{\lambda T} \tag{3.5}$$

In the following, the required feedback bandwidth is estimated for the sample topography depicted in Figure 3.3 b). In this case, W=50 nm, T=30 ms and the scan line N=100. The scan velocity is thus 0.33 mm/s and with a periodicity of 10 nm, the feedback bandwidth needed to achieve the desired velocity is f_B=33.33 kHz. It should be noted that the maximum achievable scan velocity, for a given feedback bandwidth, depends on the maximum spatial frequency in the sample topography. A more precise expression for the maximum achievable scan velocity, taking into account surface elasticity and damping of the cantilever in the surrounding medium, is given by [145]

$$V_s \sim \frac{\lambda}{2}\sqrt{\frac{k_c + S}{m} - \frac{D^2}{2m^2}} \tag{3.6}$$

where S is the surface elasticity and D describes the damping in the surrounding medium. k_c and m describe the spring constant and the effective mass of the cantilever respectively.

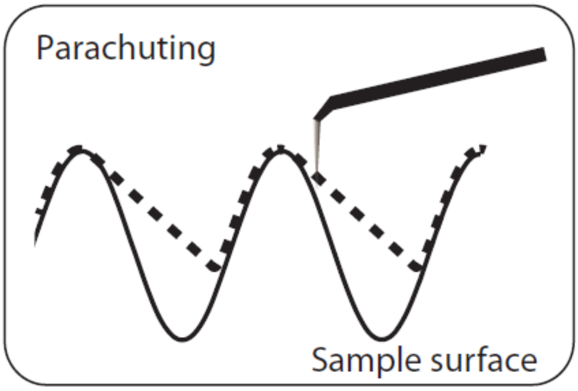

Figure 3.4: Schematic representation of parachuting [136].

The feedback bandwidth depends on several factors. In intermittent contact mode, the main delays in the AFM are the read time of the cantilever oscillation amplitude τ_d and its response time τ_c, the z-scanner response time τ_s, the parachuting time τ_p and the integral time τ_I of the error signals in the feedback controller. Parachuting here means that the cantilever tip separates from the surface in a strongly inclined area on the sample and then takes a certain amount of time until the tip returns onto the sample surface (see Figure 3.4). The time required to measure the amplitude of a cantilever that is oscillating at its resonance frequency is at least $1/(2f_c)$. An approximation for the feedback bandwidth depending on the cantilever and z-scanner parameters is given by

$$f_B = \frac{\alpha\pi f_c f_s}{8(\pi f_s + 2f_s Q_c + 2Q_s f_c + 2\pi f_s f_c(\tau_p + \tau_I + \delta))} \tag{3.7}$$

where f_s is the z-scanner resonant frequency and the quality factor for cantilever is Q_c and for z-scanner Q_s. Other time delays are referred to as δ and α is considered a factor for the phase compensation effect associated with the proportional-integral-derivative (PID) feedback controller or the respective additional phase compensator. Depending on the sample to be imaged and its phase delay, the highest possible imaging rate can be estimated in an AFM setup for intermittent contact mode. Parachuting will be explained in more detail at a later stage.

3.3.2 Adjusting elements for HS-AFM

3.3.2.1 HS-AFM Tips

Now, some elements that are important for optimizing the HS-AFM system are considered. When looking at the cantilever, the related feedback delays are the amplitude detection time and the response time of the cantilever. These delays are inversely proportional to the resonance frequency and decrease as the f_c increases. Thus, cantilevers with high resonance frequencies are desirable. For a rectangular cantilever with the corresponding dimensions of thickness d, width w and length L, the resonant frequency f_c and the spring constant k_c can be expressed as follows in equation (3.8) and (3.9). In these equations, the Young's modulus E and the density q are material-specific quantities.

$$f_c = 0.56\frac{d}{L^2}\sqrt{\frac{E}{12q}} \tag{3.8}$$

$$k_c = \frac{wd^3}{4L^3}E \tag{3.9}$$

Slim cantilevers not only have a high imaging rate, but at a given spring constant, the resonant frequency increases with decreasing cantilever mass. A point which has to be taken into account as well, is thermal noise. The thermal energy of the Brownian vibration is described by the RMS amplified spectral density n_{zB} with equation (3.10) [146].

$$n_{zB} = \sqrt{\frac{2k_B T}{\pi f_c k_c Q_c}\frac{1}{\left[1-(\frac{f}{f_c})^2\right]^2 + \left[\frac{f}{f_c Q_c}\right]^2}} \tag{3.10}$$

where k_B is the Boltzmann constant, T is the absolute temperature and Q_c is the quality factor of the cantilever. The total RMS vibration amplitude $\overline{z_B}$ which is induced by the heat energy is obtained by integrating n_{zB} over the entire frequency range yielding the expression in equation (3.11).

$$\overline{z_B} = \sqrt{\frac{k_B T}{k_c}} \tag{3.11}$$

The total thermal noise for oscillation along the z-direction depends only on the spring constant and the temperature and is given by the term $\sqrt{\frac{k_B T}{k_c}}$. Due to the much higher spring constant for oscillation in the lateral direction, the thermal noise signal for lateral oscillations should be negligible at common room temperatures. Therefore, a cantilever with a higher resonant frequency suffers less noise. The imaging frequency range in the intermittent contact mode is approximately the imaging bandwidth (where the maximum frequency is the feedback frequency) centered on this resonance frequency. Also, shorter cantilevers have higher optical beam deflection (OBD) detection sensitivity. Similarly, a high resonance frequency and a small spring constant cause a large (f_c/k_c) ratio and thus the cantilever has a high sensitivity with respect to the force gradient (k) exerted between the tip and the sample. The cantilever resonance frequency was shifted by the force gradient by -0.5 kf_c/k_c. Therefore, small cantilevers with large f_c/k_c are suitable for phase contrast imaging.

Cantilevers used for HS-AFM are small in size and therefore have a very high resonance frequency. AFMs with a sufficient small laser spot and corresponding electronics, which work with high resonant frequencies of up to 5 MHz, can use these ultra-short cantilevers (USC). These ultra-short cantilevers (see Figure 3.5 a)) vibrate in the MHz range and are very sharp and wear-resistant. They are rectangular, made of a quartz-like material, and except for the tip, the cantilevers are gold-plated on both sides to optimize the reflectivity for the laser beam. To preserve the wear resistance of the tips, they are made of High Density Carbon (HDC) and Diamond Like Carbon (DLC) material. The height of the tip is 2.5 microns and the radius of curvature is less than 10 nm. All presented AFM tips have a silicon carrier chip with the dimensions of 1.6 mm×3.4 mm×0.3 mm. In order to avoid contact between the carrier chip and the sample, the corners have been lowered and grooves have been made on the back of the cantilevers to maintain the matched laser beam without major impact on the measurement.

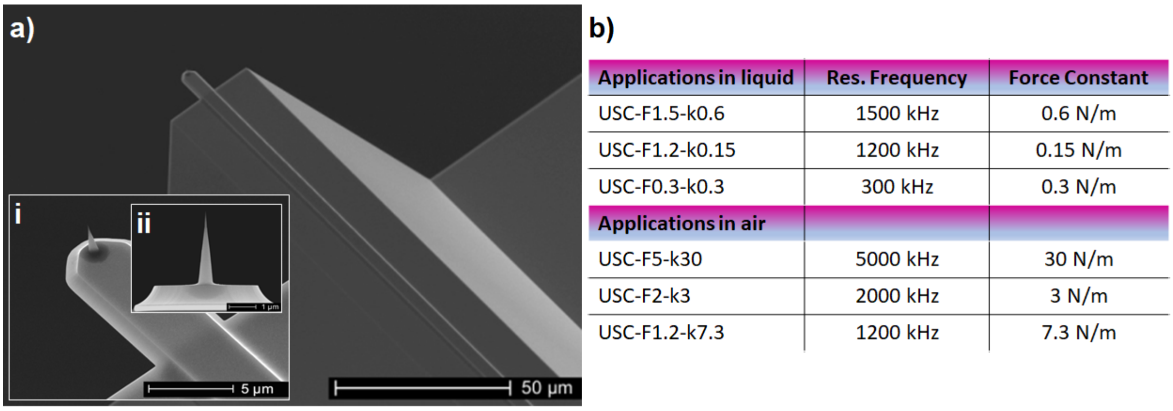

Applications in liquid	Res. Frequency	Force Constant
USC-F1.5-k0.6	1500 kHz	0.6 N/m
USC-F1.2-k0.15	1200 kHz	0.15 N/m
USC-F0.3-k0.3	300 kHz	0.3 N/m
Applications in air		
USC-F5-k30	5000 kHz	30 N/m
USC-F2-k3	2000 kHz	3 N/m
USC-F1.2-k7.3	1200 kHz	7.3 N/m

Figure 3.5: USC Cantilever used for HS-AFM. a) shows scanning electron microscope (SEM) images of a USC cantilever from NanoWorld AG, i) shows a zoom of the tip and in the inset ii) is again shown an enlargement of the actual tip of the USC cantilever, b) shows the parameters of different USC cantilevers suitable for HS-AFM measurement in liquid or air [147]. The SEM images in a) were kindly provided by NanoWorld AG. All image rights remain at NanoWorld AG.

These cantilevers can be divided into two categories, one for the basic dynamic application in air and the other for basic liquid application. The USC cantilevers for measurements in liquid in Figure 3.5 have a resonance frequency of 1500 to 300 kHz and a force constant of 0.6 to 0.15 N/m. The USC cantilevers designed for measurements in air have a slightly higher resonance frequency and start at 1200 kHz and go up to 5000 kHz. Accordingly, the force constants cover a range from from 3 N/m to 30 N/m. The cantilever USC-F0.3-k0.3 was used for the HS-AFM measurements in this work.

3.3.2.2 The optical beam deflection detector OBD

For a small cantilever, a tailored optical beam deflection detector, as the one developed by Schäffer *et al.* [148], is also required. The reflected laser beam from the cantilever is collected and collimated with the same lens as the incident laser beam focused on the cantilever. In the work of Ando *et al.* [142] it was also described that exactly this method is used, with a few changes. They do not use single lenses but a Nikon lens. The incident and reflected laser beam is separated with a $\lambda/4$ plate and a polarization beam splitter. Figure 3.6 shows the inverse optical microscope described in their HS-AFMs.

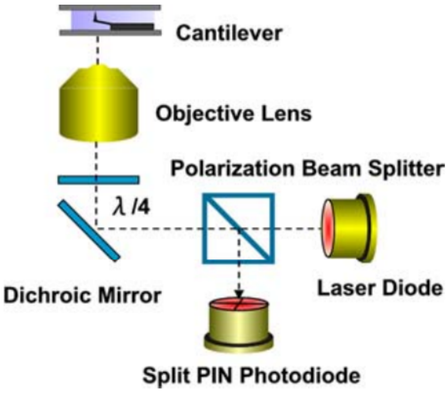

Figure 3.6: A schematic of the OBD detection system. From the laser diode, light falls on the polarization beam splitter and becomes linearly polarized. At the dichroic mirror, the light is mirrored and guided to the $\lambda/4$ plate and is circularly polarized. The objective lens focuses the light and guides it to the cantilever. The circularly polarized light reflected by the cantilever thereby reverses its direction of rotation and is collected by the objective, guided to the $\lambda/4$ plate and converted back into linear polarized light. By changing the direction of rotation, the linearly polarized light is perpendicular to the incident polarization at the polarization beam splitter. Thus, the light is not transmitted but is reflected onto the split PIN photodiode [142].

To further suppress noise originating from the optics, the laser diode is modulated using an RF power modulator. In addition, a 4-segment Si PIN photodiode with 3 pF and 40 MHz and a corresponding fast amplifier/signal conditioner with about 20 MHz is used.

3.3.2.3 Counterbalance of the HS-AFM piezoelectric actuators

For HS-AFM measurement, the mechanical components may create unwanted vibrations and are the hardest to optimize for high-speed scanning. Optimizing high-speed scanners requires certain conditions. Firstly, high resonance frequencies are needed to allow fast scanning (see equations 3.5 and 3.7). Additionally, the possible number of resonance peaks in a narrow frequency range should be kept as small as possible, ideally only one resonance peak. Ideally, the x, y, and z piezo electronics should be independently controllable with as little cross-talk as possible. Next to high scanning rates, it is desirable to maintain a reasonably large scanning area. As already mentioned, the quality factor of the cantilever should be kept small to suppress thermal noise (see equation 3.10).

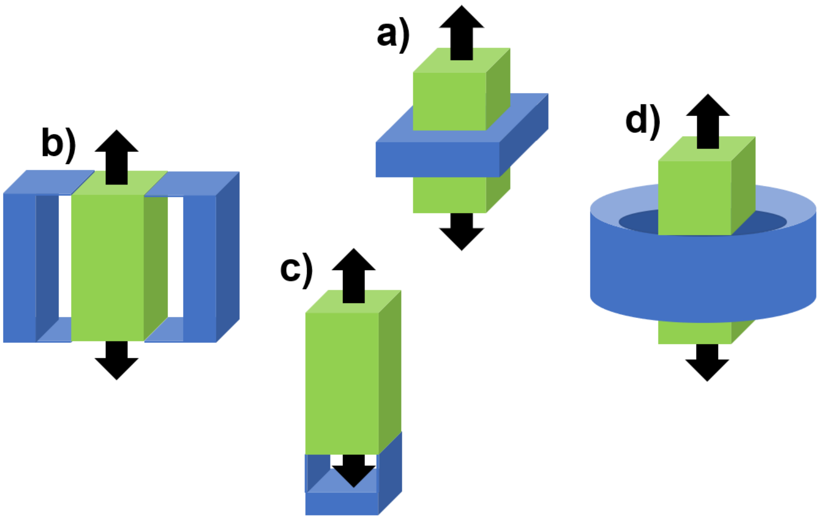

Figure 3.7: Different setups to minimize undesired vibrations cause by the piezoelectric actuators: The piezoelectric actuators (green), and the holders are in blue a) Shows two actuators are attached to the base (blue), b) Two sides of the actuator are held in place with a clip, c) the actuator is held at the corners of a plane perpendicular to the displacement direction, d) the actuator is glued at the edge parallel to the displacement direction [142]

In order to minimize the vibrations originating from the piezo electric actuators, they need a good counterbalance. The rapid shifts in one of the piezoelectric actuators cause a force pulse on the base and the surrounding framework. This in turn leads to unwanted vibrations of the actuator itself through the connection of actuator and base.

There are various approaches to avoid such unwanted vibrations. Figure 3.7 illustrates four of these approaches. In Figure 3.7 a) an approach in which two actuators are mounted on opposite sides of the base so that the vibrations caused by one actuator are canceled by the other actuator is illustrated. Below the resonance frequency of the actuators, the counterbalance works well, otherwise the compensation of the momentum forces is insufficient [142], since the phase of the oscillation changes strongly around the resonance frequency. This has the consequence that even small differences in the mechanical properties of the two actuators lead to insufficient compensation of the vibrations.

Another actuator (Figure 3.7 b)) has a structure in which the actual actuator is held by two set pieces arranged along the direction of displacement. Yet another possibility is to connect the actuator to the base via the edges of corners that are perpendicular to the direction of displacement. In the last variant presented (Figure 3.7 d)), the actuator is glued to an annular base along the direction of displacement.

3.3.2.4 Adjusting the PID controller for HS-AFM

A critical aspect when performing measurements on biological samples, is the force exerted on the system under investigation. This force can be divided into a static and a dynamic part. At this point it is sufficient to note that both parts grow with a decreasing amplitude setpoint. Thus, when biological samples are investigated, the amplitude setpoint is typically chosen as close to 1 as possible in order to prevent damage of the sample. This poses a problem for conventional PID controllers which use a static set of gain parameters. When the scanning AFM tip encounters a downhill region on the sample surface, a static set of gain parameters easily leads to the AFM tip loosing the surface when high amplitude setpoints are used. Depending on the exact gain parameters, it takes a certain time (τ_p) until the tip gets back in contact with the surface. During this period, the AFM cannot provide any useful information about the sample topology. This phenomenon is commonly called parachuting and is schematically depicted in Figure 3.4. According to [136], the condition, under which no parachuting occurs may be expressed as

$$A_0 \left(1 - r\right) - h_0 \sin\left(\frac{\theta}{2}\right) > 0 \tag{3.12}$$

where A_0 denotes the free oscillation amplitude and r the normalized amplitude setpoint, h_0 denotes the height amplitude of the assumed sinusoidal surface, and θ denotes the phase delay between the cantilever oscillation and the cantilever excitation signal. This relation, however, poses a severe limitation to the feedback frequency of the system. Ando *et al.* give a concrete example where $A_0 = h_0/5$ and $r = 0.9$. Using these values, relation (3.12) restricts the phase delay θ to values below $2.3°$. The achievable maximum feedback frequency is then given as $f < 0.05 f_B$. In contrast, using realistic parameter values from actual imaging experiments on functioning proteins, keeping the maximum force exerted to the sample in uphill regions below a value of 100 pN, the feedback frequency is limited to $f < 0.46 f_B$. To this end, the limit imposed by parachuting is far more severe than the limit imposed by the maximum allowed force.

The parachuting problem may be leveraged by using dynamic PID controllers which use changes in the oscillation amplitude of the cantilever to detect whether a flat or an inclined region of the sample is scanned. For uphill regions, the oscillation amplitude gets smaller whereas in downhill regions it gets larger. The dynamic PID may be achieved by feeding the actual PID with a false error signal by adding a term $(A(t) - A_{\text{lower/upper}})$ to the actual error signal [142]. Here A denotes the detected oscillation amplitude and A_{lower} and A_{upper} denote acceptable lower and upper bounds respectively. The adjusted error signal leads to a quicker feedback of the PID in both, uphill and downhill regions of the sample.

3.3.3 Comparison between AFM and HS-AFM

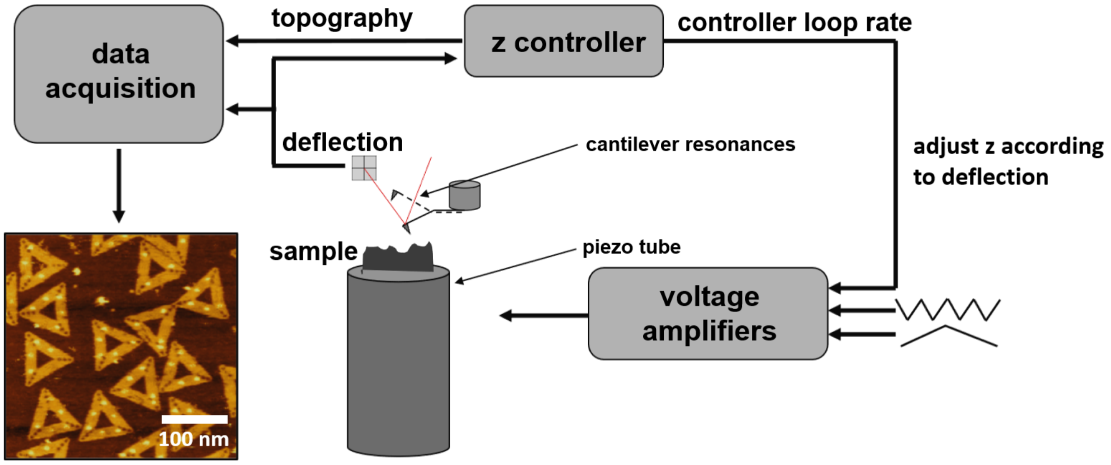

Figure 3.8: Schematic layout of the HS-AFM and AFM. The benchmarks listed in Table 3.1 show the differences between conventional and HS-AFMs.

The differences between AFM and HS-AFM are found in the components of the systems, as well as the use of appropriate cantilevers. Figure 3.8 shows the schematic structure of an AFM and Table 3.1 compares some of the key data between AFM and HS-AFM.

Table 3.1: Comparison of the AFM against HS-AFM with some key data of the systems and used cantilever tips.

	AFM	HS-AFM
cantilever resonance (in air)		
contact	13–67 kHz	
tapping	75–3200 kHz	1.2–5 MHz
piezo tubes		
z	1 kHz [149]	$>$ 50 kHz [150]
x, y	200–1,200 Hz [149]	$>$ 1kHz [150]
data aquisition	0–21 Hz [a)]	1–150 Hz [b)]
controller loop rate	50–500 Hz [149]	$\sim$ MHz[c)]

[a)] Used settings on the JPK NanoWizard 2

[b)] Used settings on the JPK NanoWizard Ultra Speed 1

[c)] Estimated order of magnitude

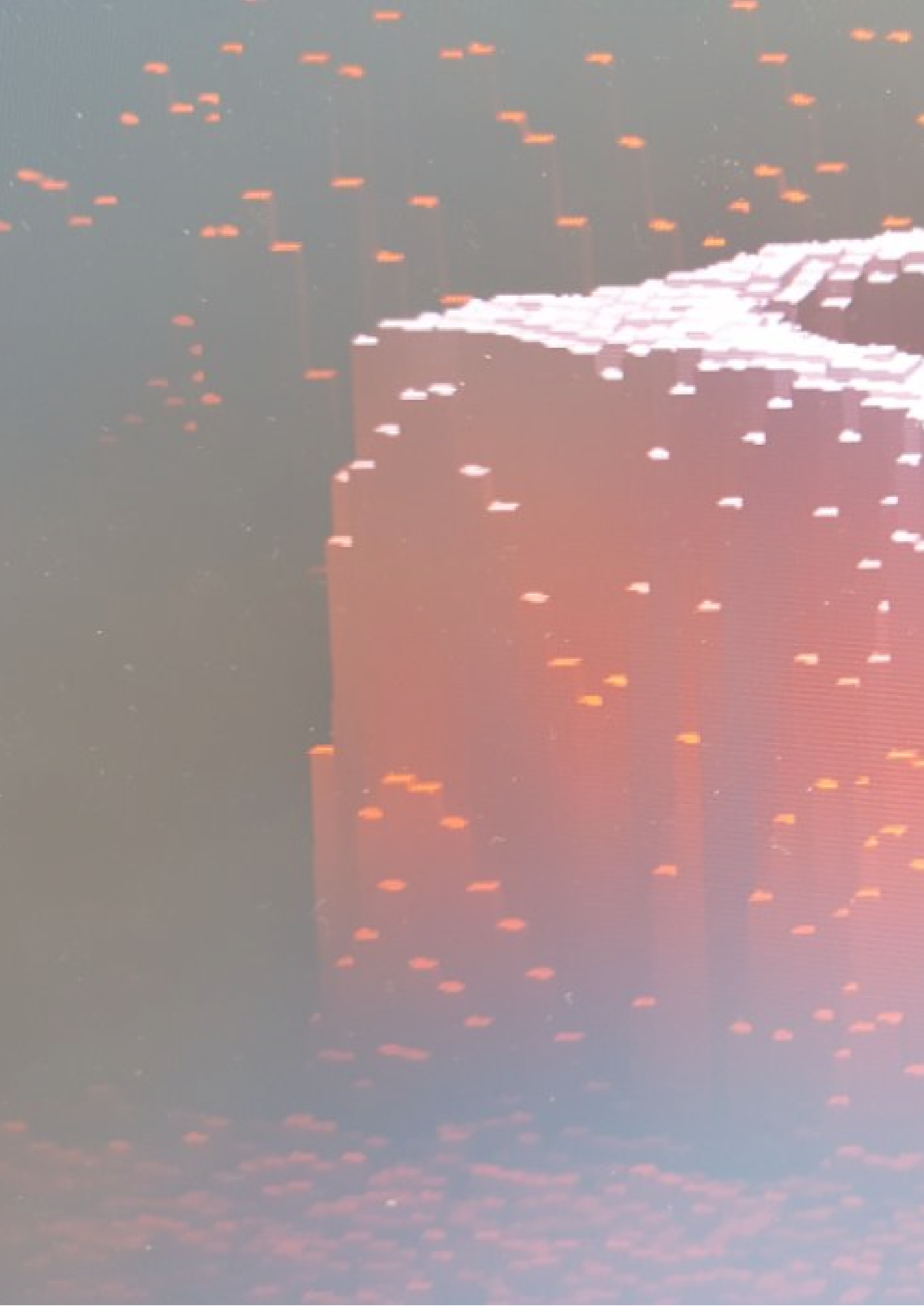

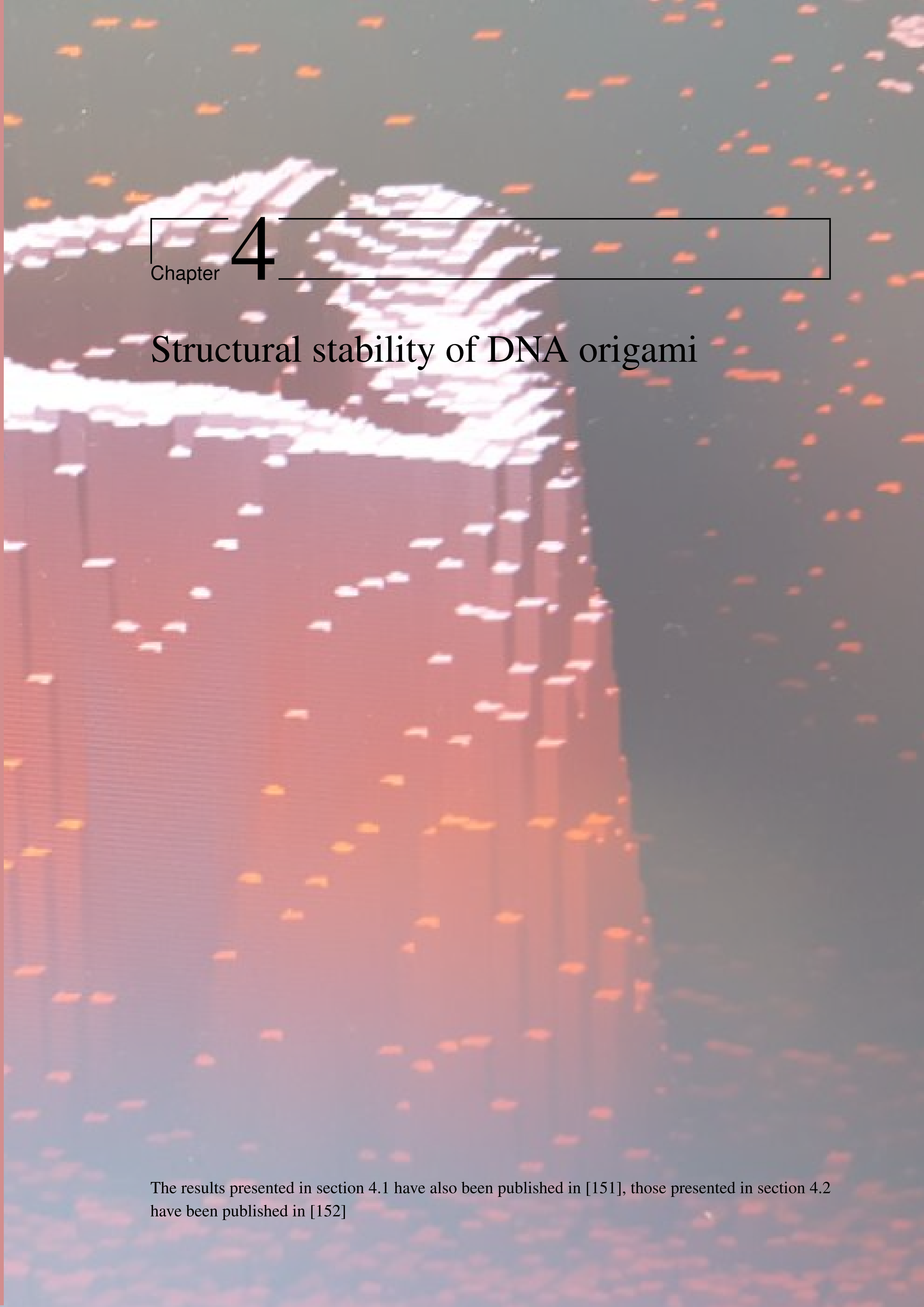

Chapter 4

Structural stability of DNA origami

The results presented in section 4.1 have also been published in [151], those presented in section 4.2 have been published in [152]

DNA origami nanostructures are widely employed in various areas of fundamental and applied research. Due to the tremendous success of the DNA origami technique in the academic field, considerable efforts currently aim at the translation of this technology from a laboratory setting to real-world applications, such as nanoelectronics, drug delivery, and biosensing. While many of these real-world applications rely on an intact DNA origami shape, they often also subject the DNA origami nanostructures to rather harsh and potentially damaging environmental and processing conditions. Furthermore, in the context of DNA origami mass production, the long-term storage of DNA origami nanostructures or their pre-assembled components also becomes an issue of high relevance, especially regarding the possible negative effects on DNA origami structural integrity.
Thus, the following section will cover considerations and experiments regarding the stability of different DNA origami structures in different low Mg^{2+} buffer solutions. Furthermore, considering the problem of long-term storage, the stability of DNA origami assembled with staple strands which have been stored for time periods ranging up to 44 months in case of triangle DNA origami and 56 months in case of 6HBs, is investigated.

4.1 On the Stability of DNA Origami Nanostructures in Low-Magnesium Buffers

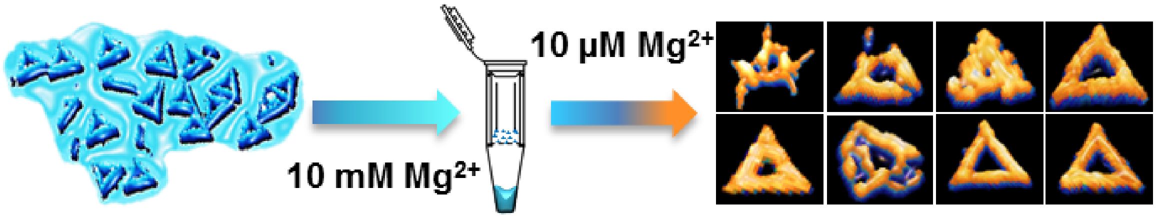

4.1.1 Introduction

The DNA origami technique [23, 29] has become a widely used method for the fabrication of complex, yet well-defined nanostructures [153, 154] with applications in biophysics [155, 156], molecular biology [53, 157], and drug and enzyme delivery [158, 159]. Since many of these applications rely on intact DNA nanostructures, the investigation of DNA origami stability under application-specific conditions has become a major research focus [86, 89, 97, 101, 129, 133, 160–163]. Biomedical applications in particular are often incompatible with the comparatively high (10 - 20 mM) Mg^{2+} concentrations required for DNA origami assembly. On the other hand, low Mg^{2+} concentration ($\leq$ 1 mM) has been identified as one of the two most critical parameters that reduce DNA origami stability in cell culture media [97]. Consequently, many approaches have been reported for protecting DNA origami nanostructures against destabilizing conditions and in particular low Mg^{2+} concentrations [103, 106–111]. All the more surprising was the discovery that DNA origami are stable in water for several weeks [133]. In these experiments, the Mg^{2+}-containing assembly buffer was exchanged against water via spin filtering, resulting in Mg^{2+} concentrations of a few μM. Although not completely Mg^{2+}-free, many applications may benefit from intact DNA origami nanostructures under such low-Mg^{2+} conditions. However, other studies observed DNA origami denaturation in buffers containing low Mg^{2+} concentrations [97, 108, 111, 160, 163]. These discrepancies could have various origins, such as differences in the buffer exchange methods, buffer conditions, and DNA origami designs. In this work, therefore the stability of three DNA origami nanostructures in a selection of low-Mg^{2+} buffers is investigated using the spin filtering-based buffer exchange approach established by Linko *et al.* [133] which is described in more detail in section 4.1.4.2. It is found that the composition of the buffer plays a critical role in DNA origami stability, while different DNA origami nanostructures show different buffer dependencies.

4.1.2 Results and Discussion

At first an attempt is made to reproduce the results of Linko *et al.* for the three DNA origami nanostructures investigated in this work, i.e., the Rothemund triangle [23], a 24-helix bundle (24HB) [21], and a six-helix bundle (6HB) [164]. The DNA origami were assembled using Mg^{2+} concentrations of 10 mM for triangles and 6HBs, and 14 mM for 24HBs as described in section 4.1.4.1. After folding, spin filtering and washing with water were used to purify the structures from excess staple strands.

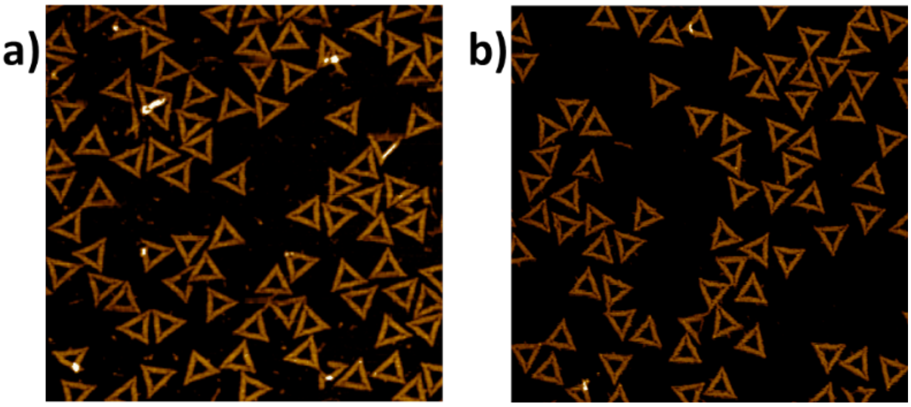

Figure 4.1: AFM images of triangular DNA origami before a) and after spin filtering 1 x tris-acetate-EDTA (TAE) with 10 mM $MgCl_2$ b). No significant differences in DNA origami damage are observed. Image sizes and height scales are $1.5\times1.5\ \mu m^2$ and 2.0 nm, respectively.

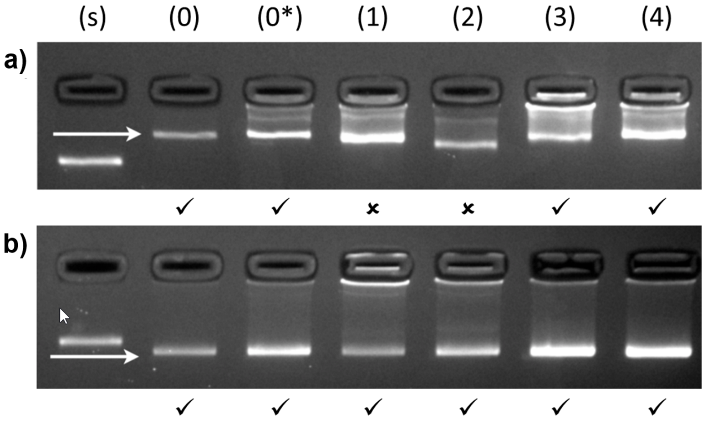

Figure 4.2: AGE results of DNA origami triangles a) and 6HBs b) before (0) and after buffer exchange into 1 x TAE + 10 mM $MgCl_2$ (0*), 1 x TAE with pH 8 (1), 1 x TAE with pH 9 (2), 10 mM Tris with pH 8 (3), and 10 mM Tris with pH 9 (4). The M13mp18 scaffold (s) is used as a control (7249-nucleotides). The positions of the monomer bands are indicated by the white arrows. DNA origami stability and denaturation as observed in the gel images are indicated by ✓ and ✗, respectively. DNA origami before (0) and after (0*) spin filtering with folding buffer (1 x TAE with 10 mM $MgCl_2$) do not show significant differences in DNA origami stability (agree with the results shown in Figure 4.1). For triangles, 1 x TAE with pH 8 (1) and 1 x TAE with pH 9 (2) denature DNA origami samples (denaturation is more pronounced at pH 9 as EDTA chelation efficiency increases with pH). However, triangles remain intact in Tris buffers at both pH levels. In case of 6HB no significant effect of buffer pH on DNA origami stability is observed. The AGE measurements have been performed at the Department for Bioproducts and Biosystems of Aalto Unitversity (Finland)[151].

Spin filtering itself, i.e., without buffer exchange, has no significant effect on DNA origami stability (see Figures 4.1 and 4.2). Repeated application of filtering/washing cycles results in a continuous decrease in the Mg^{2+} concentration. The filtered DNA origami were immobilized on mica after each cycle and evaluated by AFM. Image acquisition has been performed as described in section 4.1.4.3. As can be seen in Figure 4.3 d), all three DNA origami nanostructures are stable even after three filtering/washing cycles, corresponding to a Mg^{2+} concentration < 1 μM (see Table 4.1). Closer inspection of the AFM images in Figure 4.3 d), however, reveals some defect triangular DNA origami at such low Mg^{2+} concentrations. This indicates that a minimum Mg^{2+} concentration in the low-μM range is required to ensure DNA origami stability. Because of their less distinctive shapes, similar defects are harder to identify in the helix bundles. For further experiments two filtering/washing cycles for buffer exchange have been used, resulting in residual Mg^{2+} concentrations of around 10 μM, see Table 4.1.

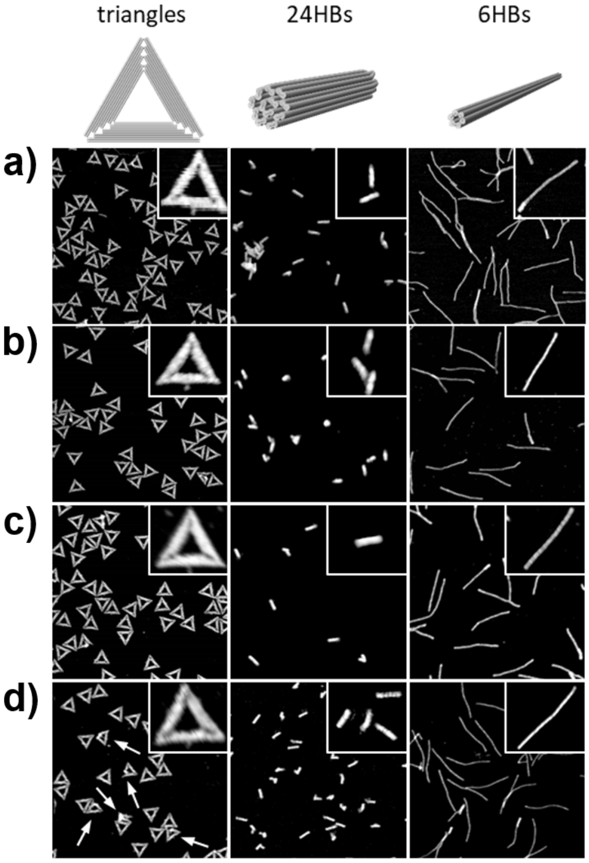

Figure 4.3: AFM images of DNA origami triangles, 24HBs, and 6HBs in 1 x TAE containing 10 mM $MgCl_2$ for different numbers of filtering/washing cycles. a) and after applying one b), two c), and three d) filtering/washing cycles with pure water. Image sizes are 1.5×1.5 μm^2 and height scales 2.0 nm (triangles), 4.0 nm (24HBs), and 2.7 nm (6HBs), respectively. Insets show representative zooms of individual DNA origami. The arrows in d) indicate defective DNA origami triangles.

Figure 4.4 shows AFM images of all three DNA origami nanostructures after exchanging the Mg^{2+}-containing 1 x TAE assembly buffer against eight different Mg^{2+}-free buffers. Exchange against pure 1 x TAE (condition 1) results clearly in the disintegration of the DNA origami triangles and 24HBs. This drastically decreased stability of the DNA origami triangles and 24HBs in TAE compared to water may be explained by the presence of 1 mM ethylenediaminetetraacetic acid (EDTA) in the TAE buffer, which will chelate all the remaining Mg^{2+} ions bound to the phosphate groups in the DNA backbone. Repulsive electrostatic interactions between neighboring helices then induce DNA origami disintegration. In order to test this hypothesis, DNA origami have transferred into EDTA-free 10 mM Tris buffer and indeed stable DNA origami triangles and 24HBs (Figure 4.4, condition 2) have been observed, thus confirming the damaging effect of EDTA. Surprisingly, EDTA does not seem to affect the stability of the 6HBs which show no visible signs of damage in neither buffer (Figure 4.4 c), conditions 1 and 2). This observation is in agreement with previous experiments of Hahn *et al.*, who found the DNA origami 6HBs significantly more stable in low-Mg^{2+} tissue culture medium than other 3D DNA origami [97]. These differences may originate from a superstructure-dependent binding of Mg^{2+} to the backbone phosphates, as has been observed for Eu^{3+} coordination of the same triangles and 6HBs studied here [165]. Furthermore, the 6HBs are more flexible than the triangles and 24HBs and may more easily compensate electrostatic repulsion between their helices by adopting a conformation with larger interhelical spacing [166].

In many medical and biological applications, phosphate-based buffers such as phosphate-buffered saline are routinely employed. Therefore, DNA origami nanostructures have also been transferred the into 10 mM Na_2HPO_4. This resulted in denatured DNA origami triangles and 24HBs, whereas the 6HBs again remained stable (Figure 4.4, condition 3). At first glance, the decreased stability of the DNA origami triangles and 24HBs in Na_2HPO_4 compared to water seems counterintuitive since the phosphate buffer contains much more cations which should stabilize the DNA origami nanostructures. While Na^+ is about 10 times less efficient in stabilizing DNA duplex structure than Mg^{2+} [167], a concentration of 20 mM should still be sufficient to maintain intact duplexes even if the residual Mg^{2+} ions were completely displaced from the backbone phosphates. On the other hand, Na_2HPO_4 introduces partially dissociated ${HPO_4}^{2-}$ ions which may interact with the phosphate-bound Mg^{2+} ions and reduce their efficiency of screening electrostatic repulsion between neighboring helices. In addition, the resulting bulky complex will make Na^+-phosphate binding much less effective. Increasing the Na^+ concentration should then lead to a gradual replacement of the Mg^+ complexes and finally to stable DNA origami. Indeed, as can be seen in Figure 4.4 a), addition of 100 mM NaCl results in DNA origami nanostructures with clearly identifiable triangular shapes, despite being visibly damaged. Increasing the NaCl concentration further to 200 mM (Figure 4.4 a), condition 5), results in completely intact DNA origami triangles. In contrast, no stabilization with increasing NaCl concentration is observed for the 24HBs (Figure 4.4 b), conditions 3–5). This may be the result of the compact 3D DNA origami nanostructure, which features a dense packing of DNA helices with a high negative charge density and consequently may require even higher Na^+ concentrations for efficient stabilization.

Some applications require the use of potassium-based phosphate buffers instead of sodium-based ones, for instance to ensure the stability of certain proteins when arranging them with DNA origami scaffolds [120]. Therefore, DNA origami stability has also been evaluated in 10 mM K_2HPO_4. As can be seen in Figure 4.4 (condition 6), a similar behavior is observed as for Na_2HPO_4, with DNA origami triangles and 24HBs being almost completely denatured, while the 6HBs remain intact. In contrast to the case of Na^+, however, addition of 100 mM KCl already results in perfectly intact DNA origami triangles (Figure 4.4 a), condition 7). This difference in the stabilizing effect of Na^+ and K^+ is rather surprising, considering their close similarity and the large number of studies that observed no significant differences in DNA duplex stabilization by Na^+ and K^+ [167–170]. However, there are also a few reports of DNA having higher affinity for K^+ than for Na^+ [171, 172]. These observations have further been substantiated in molecular dynamics simulations of parallel arrangements of DNA duplexes which also included DNA-DNA interactions [173]. This system can thus be considered a more accurate representation of DNA origami nanostructures than the typically used isolated duplexes. The simulations revealed that Na^+ binds preferentially to the phosphates in the backbone, whereas K^+ predominantly interacts with electronegative sites of the nucleobases. Also the water structure around the DNA duplex is differently affected by these ions [173]. The higher stability of the DNA origami triangles in the K^+-based buffer is thus attributed to the differences in the interaction of K^+ and Na^+ with DNA.

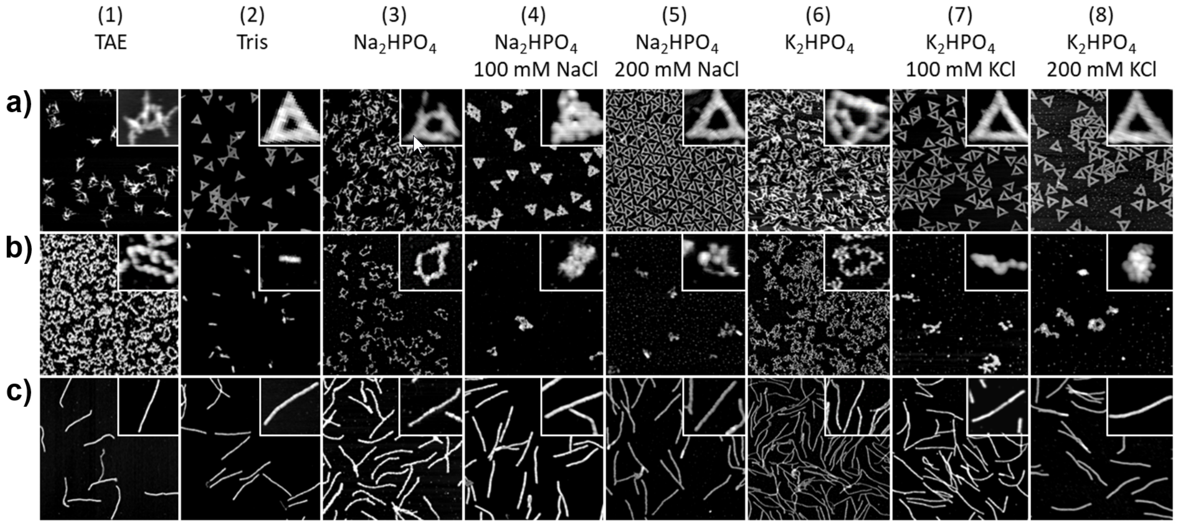

Figure 4.4: AFM images of DNA origami triangles, 24HBs, and 6HBs after transfer into different buffers. a) DNA origami triangles, b) 24HBs, and c) 6HBs after transfer into 1 x TAE (1), 10 mM Tris (2), 10 mM Na_2HPO_4 (3), 10 mM Na_2HPO_4 + 100 mM NaCl (4), 10 mM Na_2HPO_4 + 200 mM NaCl(5), 10 mM K_2HPO_4 (6), 10 mM K_2HPO_4 + 100 mM KCl (7), and 10 mM K_2HPO_4 + 200 mM KCl (8). Image sizes are 1.5×1.5 μm^2 and height scales 2.3 nm (a, conditions 1–8 and b, conditions 1 and 3–8), 4.0 nm (b, condition 2), and 3.0 nm (c, conditions 1–8). Insets show representative zooms of individual DNA origami.

In Figure 4.4 large variations in DNA origami surface coverage are observed. These differences may be caused by a number of effects. Most importantly, DNA origami adsorption is never uniform across the whole mica substrate due to surface inhomogeneities and the deposition of the sample solution which involves a meniscus moving across the surface. This is exemplified in Figure 4.5. Furthermore, also the presence of different concentrations of monovalent cations in conditions 3 to 8 may affect DNA origami adsorption efficiency as they can replace some of the Mg^{2+} ions from the mica surface and thus interfere with electrostatic interactions between DNA origami and surface [120].

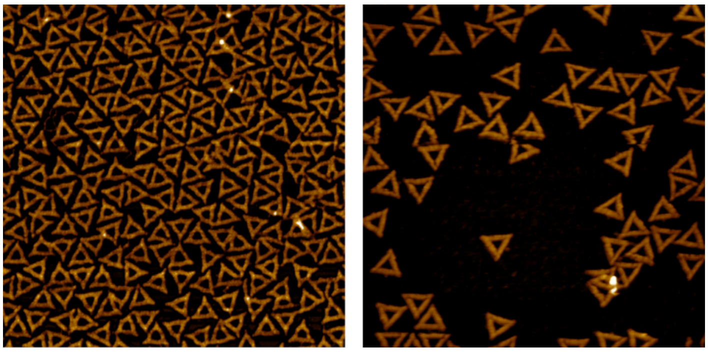

Figure 4.5: AFM images of triangular DNA origami in 10 mM Na_2HPO_4 + 200 mM NaCl. The images correspond to two different, identically treated samples. Significant variations in DNA origami coverage are observed. Image sizes and height scales are 1.5×1.5 μm^2 and 2.3 nm, respectively.

Since structural damage of the 24HBs and the 6HBs is hard to identify in AFM images, all tested DNA origami-buffer combinations were also examined by agarose gel electrophoresis [151]. For the DNA origami triangles, the Agarose Gel Electrophoresis (AGE) results shown in Figure 4.6 a) agree with the ones obtained by AFM, with the exception of 10 mM Na_2HPO_4 + 100 mM NaCl (condition 4). Here, AGE indicates intact DNA origami while AFM clearly shows partially denatured triangles (see Figure 4.4 a)). This discrepancy can be attributed to the rather well conserved triangular shape of the damaged DNA origami which thus run at a similar speed as the intact ones. This demonstrates the limitations of assessing nanostructural integrity solely by AGE without the aid of single-molecule imaging techniques. This is becoming even more obvious for the 24HBs (Figure 4.6 b)). Due to their tendency to form aggregates (see Figure 4.3 a), middle panel), identifying the bands in the gel images is rather difficult. This is particularly obvious in the case of the unfiltered 24HBs (lane 0), where only a faint monomer band is seen below intense multimer bands (aggregates are also seen under the same conditions in Figure 4.3 a), middle panel). However, filtering/washing with water releases the monomers and results in a clear monomer band (in accordance with AFM, see Figure 4.3 d), middle panel). While for 1 x TAE and 10 mM Tris (conditions 1 and 2) rather unambiguous results are obtained, the phosphate buffers yield results that are less clear. As in the case of the DNA origami triangles, a pronounced monomer band is observed for 10 mM Na_2HPO_4 + 100 mM NaCl (condition 4), which can again be attributed to the rather compact shapes of the denatured 24HBs (see Figure 4.4 b)). Also for 10 mM Na_2HPO_4 + 200 mM NaCl (condition 5), a faint monomer band can be identified in Figure 4.6 b) for the same reason, which could falsely be interpreted as proof of intact DNA origami. For 10 mM K_2HPO_4 + 200 mM KCl (condition 8), a weak leading band can be seen that runs between the bands of completely denatured and intact 24HBs. This may indicate that the 24HBs are getting gradually more stabilized by the increasing KCl concentration, although they still are strongly denatured as is evident from AFM (Figure 4.4 b)). The AGE results of the 6HBs in Figure 4.6 c) are in excellent agreement with the AFM analysis and show only intact DNA origami.

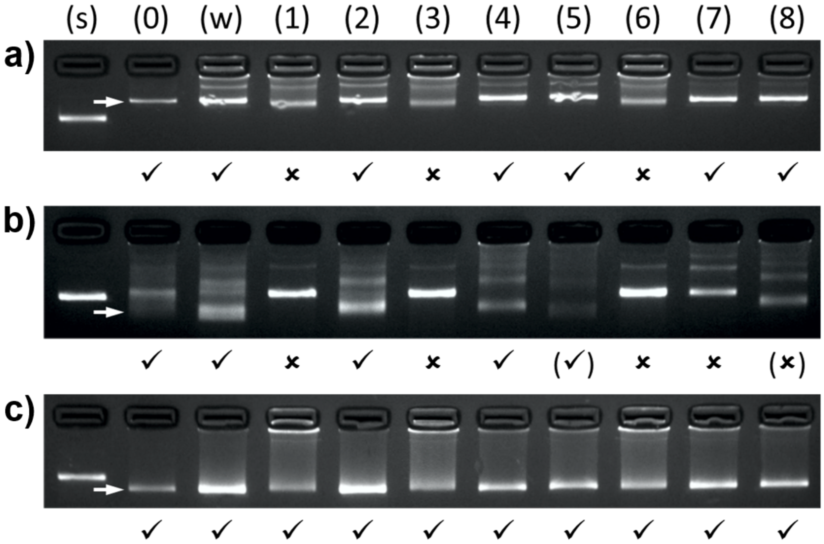

Figure 4.6: AGE results for different DNA origami structures before and after transfer into water from different buffers. a) DNA origami triangles, b) 24HBs, and c) 6HBs before (0) and after transfer into water (three filtering/washing cycles) (w), 1 x TAE (1), 10 mM Tris (2), 10 mM Na_2HPO_4 (3), 10 mM Na_2HPO_4 + 100 mM NaCl (4), 10 mM Na_2HPO_4 + 200 mM NaCl (5), 10 mM K_2HPO_4 (6), 10 mM K_2HPO_4 + 100 mM KCl (7), and 10 mM K_2HPO_4 + 200 mM KCl (8). The M13mp18 scaffold (s) is used as a control (7249-nucleotide scaffold for the triangle and 6HB, and 7560-nucleotide version for the 24HB). The positions of the monomer bands are indicated by the white arrows. DNA origami stability and denaturation as observed in the gel images is indicated by ✓and ✗, respectively. Brackets denote ambiguous results. The AGE measurements have been performed at the Department for Bioproducts and Biosystems of Aalto Unitversity (Finland)[151].

Finally, it is shown that the DNA origami are stable in the respective low-Mg^{2+} buffers for extended periods of time. This has been investigated for the triangular DNA origami in water, 10 mM Tris, 10 mM Na_2HPO_4 + 200 mM NaCl, 10 mM K_2HPO_4 + 100 mM KCl, and 10 mM K_2HPO_4 + 200 mM KCl by AFM (see Figure 4.11). For long-term stability measurements, one DNA origami sample per buffer condition was stored at 4°C and examined periodically by AFM. Due to their well-defined shape, stability of the triangular DNA origami could be assessed quantitatively, while the evaluation of the 24HBs and the 6HBs was done only qualitatively. For the quantitative evaluation, a 5×5 μm^2 AFM image was been recorded and the fraction of intact DNA origami triangles quantified by manual counting. For each data point, between 44 and 598 DNA origami triangles have been analyzed. The fractions of intact DNA origami are presented as mean values with the standard error of the mean as error bars.

Considering the stability in pure water firstly, Figure 4.7 shows representative AFM images depending on the number of filtering/washing cycles and the age of the sample. The respective fractions of intact DNA origami are plotted in Figure 4.8.

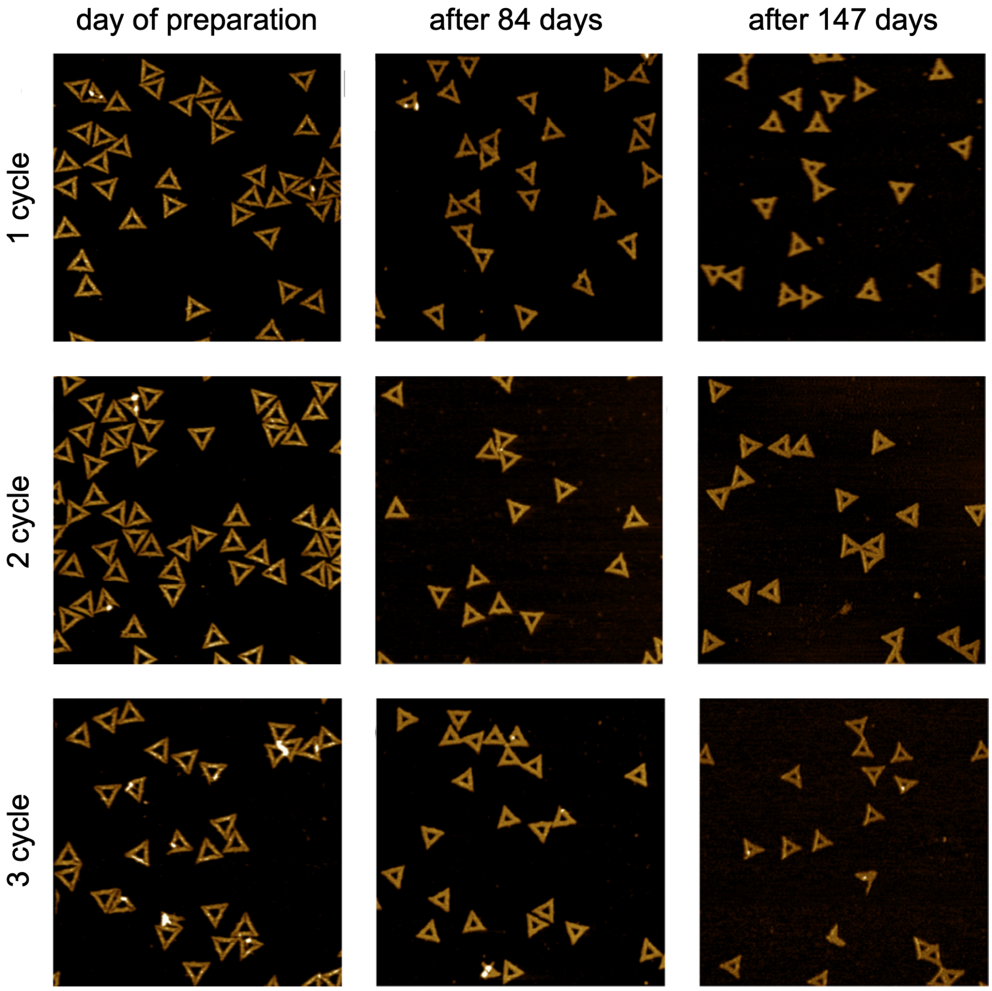

Figure 4.7: AFM images of triangular DNA origami in water after one (top row), two (middle row), and three (bottom row) filtering/washing cycles at the day of preparation (left column), after 84 days (middle column), and after 147 days (right column). Image sizes and height scales are 1.5×1.5 μm^2 and 2.0 nm, respectively.

As can be seen, the fraction of intact origami decreases both, with an increasing number of filtering/washing cycles and with increasing age of the sample. However, interestingly in the oldest sample subjected to the most filtering/washing cycles, still roughly 60% of the DNA origami are intact.

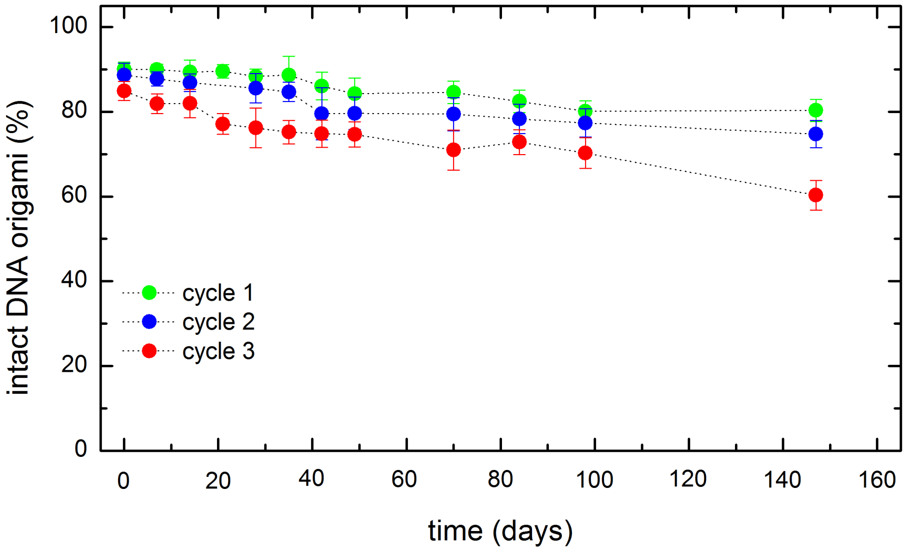

Figure 4.8: Fraction of intact DNA origami triangles in water after different numbers of filtering/washing cycles as a function of time.

Coming to the other low Mg^{2+} buffer solutions, Figures 4.9 and 4.10 show representative AFM images of triangular DNA origami in these buffer solutions. In these media, the DNA origami triangles are stable for at least two months without any significant decrease in the fraction of intact nanostructures.

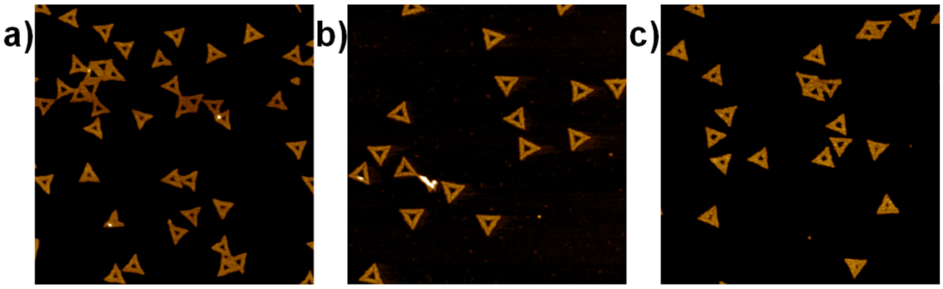

Figure 4.9: AFM images of triangular DNA origami in 10 mM Tris after two filtering/washing cycles at the day of preparation a) and after 70 b) and 126 days c). Image sizes and height scales are 1.5×1.5 μm^2 and 2.0 nm, respectively.

In Figure 4.11 the fraction of intact DNA origami in the different buffer solutions is plotted depending on the age of the samples. Here the oldest sample (in Tris) has an age of 126 days. Nevertheless, roughly 80% of the DNA origami were intact.

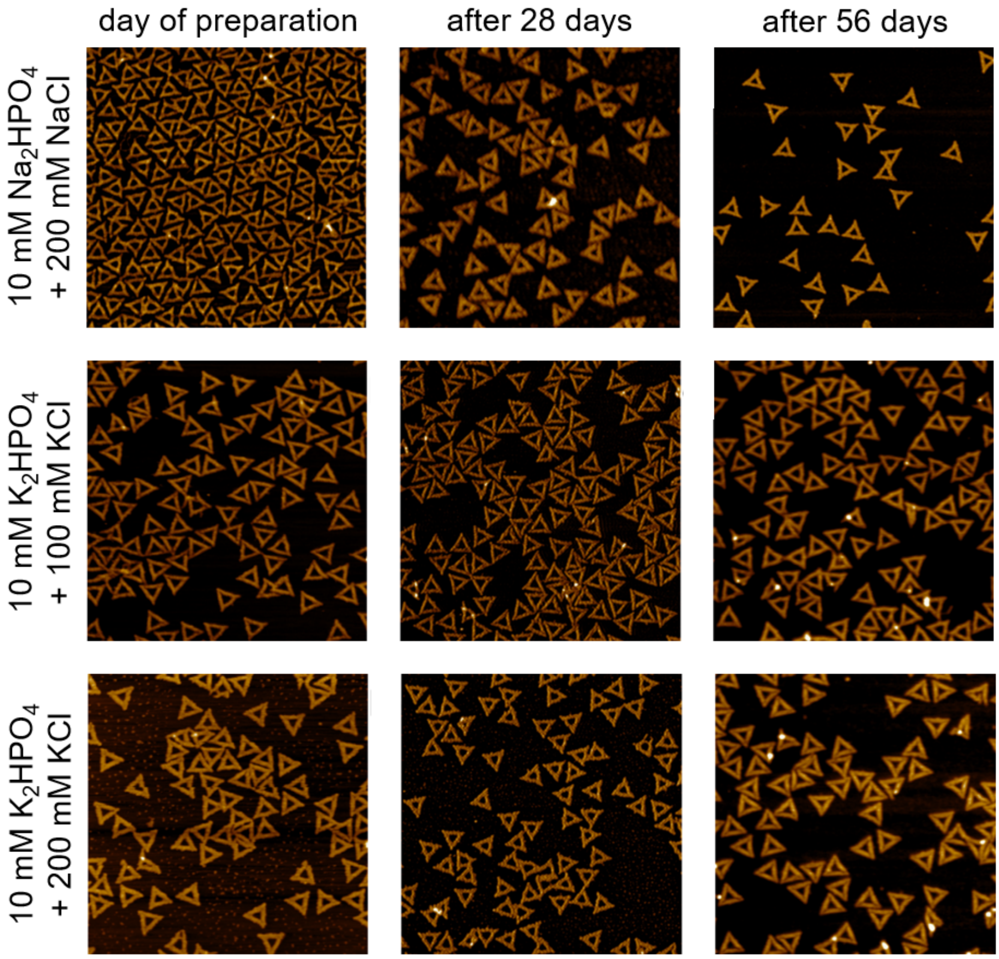
day of preparation
after 28 days
after 56 days
10 mM Na2HPO4 + 200 mM NaCl
10 mM K2HPO4 + 100 mM KCl
10 mM K2HPO4 + 200 mM KCl

Figure 4.10: AFM images of triangular DNA origami in different low Mg^{2+} buffer solutions after two filtering/washing cycles at the day of preparation (left column), after 28 days (middle column), and after 56 days (right column). The individual rows correspond to 10 mM Na_2HPO_4 + 200 mM NaCl (top row), 10 mM K_2HPO_4 + 100 mM KCl (middle row), and 10 mM K_2HPO_4 + 200 mM KCl (bottom row), respectively. Image sizes and height scales are 1.5×1.5 μm^2 and 2.3 nm, respectively.

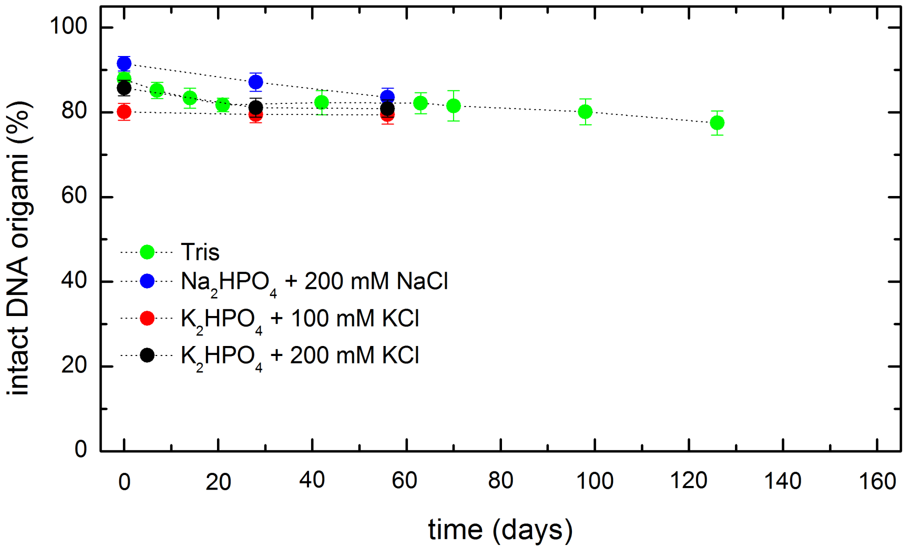

Figure 4.11: Fraction of intact DNA origami triangles in different buffers after two filtering/washing cycles as a function of time.

4.1.3 Conclusion

In summary, the stability of DNA origami triangles, 24HBs, and 6HBs has been investigated in different buffers with about 10 μM residual Mg^{2+}. The results are summarized in Table 4.2. DNA origami stability was found to crucially depend on the availability of residual Mg^{2+} ions for binding to the phosphates in the DNA backbone and screening electrostatic repulsion between neighboring helices. The presence of EDTA may facilitate DNA origami denaturation by chelating and thus removing Mg^{2+} ions from the backbone. In addition to EDTA, also phosphate ions may interact with the bound Mg^{2+} ions and induce DNA origami denaturation by reducing the strength of the Mg^{2+}-DNA interaction. However, these effects are more complex and highly dependent on the presence of monovalent cations which may replace the Mg^{2+} complexes at the phosphates and thus stabilize the DNA origami. The exact concentration necessary to ensure structural integrity, however, depends on the DNA binding affinity of the monovalent cation and the preferred binding sites, as observed here when comparing Na^+ to K^+.

Most remarkably, these buffer effects were found to depend also on DNA origami superstructure. Lattice-based 3D DNA origami nanostructures, such as the 24HB seem to require higher concentrations of monovalent cations than 2D DNA origami to maintain their structural integrity, presumably due to the high density of negative charges in their interior. In contrast, 6HBs are stable in all the tested buffers, including 1 x TAE featuring 1 mM EDTA. While this extraordinary stability of 6HBs has already been observed by Hahn *et al.* [97], it can so far only be speculated about its origin. Superstructure-dependent geometries of ion-binding sites may play a role in Mg^{2+} displacement and removal [165], while the lower stiffness of the 6HBs may allow more drastic conformational changes to compensate for electrostatic repulsion between helices [166].

The obtained results demonstrate that high Mg^{2+} concentrations are by no means a prerequisite for maintaining DNA origami stability. On the contrary, by employing rationally selected buffers and considering superstructure-dependent effects, the structural integrity of a given DNA origami nanostructure may be maintained even at Mg^{2+} concentrations in the low-μM range for extended periods of time. This qualifies DNA origami nanostructures for a broad spectrum of biophysical and biomedical applications incompatible with high Mg^{2+} concentrations.

4.1.4 Materials and Methods

4.1.4.1 DNA origami assembly

Triangular [23] and 6HB DNA origami [164] have been assembled with staple strands from Metabion and the 7249-nt long M13mp18 scaffold (Tilibit) as previously described in 1 x TAE (Carl Roth) containing 10 mM $MgCl_2$ (Sigma-Aldrich) [89]. Hybridization was carried out in a Thermocycler Primus 25 advanced (PEQLAB) by heating to 80°C and subsequent cooling to room temperature over a time course of 90 min.

24HB DNA origami from Kuzyk *et al.* [21] (left-handed design) have been assembled with staple strands from IDT and the 7560-nt long M13mp18 scaffold (Tilibit) in 1 x TAE (VWR Chemicals) containing 14 mM $MgCl_2$ (Sigma-Aldrich). The folding solution was annealed using a G-Storm Thermocycler by heating to 65°C and subsequent cooling to 40°C over a time course of 61 h.

4.1.4.2 Buffer exchange for low-magnesium buffers

The buffer of the assembled DNA origami samples was exchanged by spin filtering using Amicon ultra-0.5 ml centrifugal filters (Millipore) with 100 kDa MWCO. To this end, 100 μl of DNA origami solution were spin-filtered together with 200 μl of the respective target buffer for 10 min at 2000–6000 g. After adding 300 μl of target buffer, the sample was spin filtered a second time for 10 min at the same speed. Depending on the target Mg^{2+} concentration, this filtering/washing cycle was repeated up to twice. The concentration of residual Mg^{2+} after each filtering/washing cycle was calculated from the sample volume retained in the filter; average values are given in Table 4.1.

Table 4.1: Average concentrations (in μM) of residual Mg^{2+} for each DNA origami after each filtering/washing cycle.

	Triangles	6HBs	24HBs
1 cycle	450	450	650
2 cycles	10.6	10.6	11.6
3 cycles	0.3	0.3	0.4

The following Mg^{2+}-free buffers were prepared using HPLC-grade water (Carl Roth): 1 x TAE (Carl Roth), 10 mM Tris (Sigma-Aldrich), 10 mM Na_2HPO_4 (Merck) with and without 100 mM and 200 mM NaCl (Sigma-Aldrich), 10 mM K_2HPO_4 (Merck) with and without 100 mM and 200 mM KCl (Merck). The pH of the more alkaline buffers was carefully adjusted using 1 M HCl (Stockmeier Chemie) to reach a value between pH 8 and 9 (see Table 4.2). In this range, no significant effect of pH on DNA origami stability was observed (see Figure 4.2).

Table 4.2: Buffer solutions and their respective pH value considered for the stability studies. Summary of the results obtained for the three DNA origami nanostructures in different buffers (conditions 1 to 8) containing 10 μM of Mg^{2+}. Note that no influence of pH on DNA origami stability between pH 8 and 9 has been observed (see Figure 4.2).

Condition	Buffer	pH
1	1 x TAE	8.5
2	10 mM Tris	8.9
3	10 mM Na_2HPO_4	8.0
4	10 mM Na_2HPO_4 + 100 mM NaCl	8.3
5	10 mM Na_2HPO_4 + 200 mM NaCl	8.5
6	10 mM K_2HPO_4	8.5
7	10 mM K_2HPO_4 + 100 mM KCl	8.7
8	10 mM K_2HPO_4 + 200 mM KCl	8.9

4.1.4.3 AFM imaging

For AFM imaging, 10 μl of the DNA origami sample and 30 μl of 1 x TAE containing 10 mM $MgCl_2$ were incubated on freshly cleaved mica surfaces for 1 min. Subsequently, the mica sample was vertically dipped into HPLC-grade water for 30 seconds and blow-dried in a stream of ultrapure air. AFM measurements were carried out using an Agilent 5100 and an Agilent 5500 AFM, respectively, operated in intermittent contact mode with silicon cantilevers (HQ:NSC18/Al BS) from MikroMasch. Images were recorded with scan sizes of 5×5 μm^2 with a resolution of 2048 px$\times$2048 px. Examples of intact (green) and damaged DNA origami (red) are shown in Figure 4.12. The DNA origami indicated in white and blue have not been considered because they are not completely visible in the AFM image and lie on top of each other, respectively.

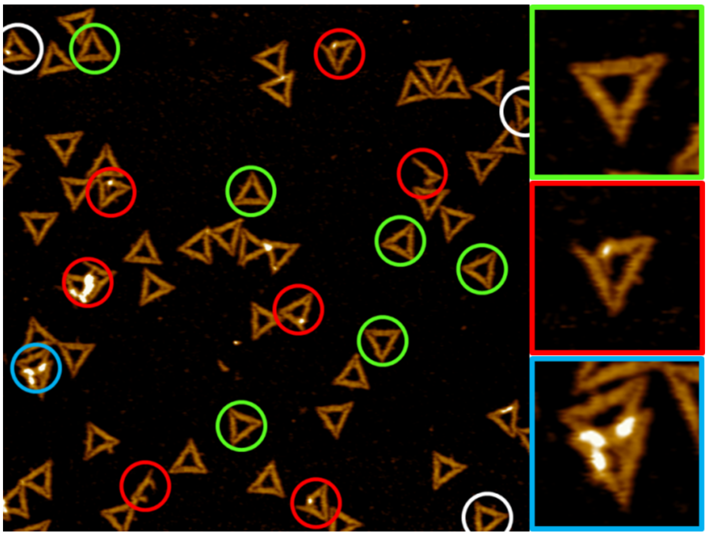

Figure 4.12: AFM image of triangular DNA origami after three filtering/washing cycles with pure water. A selection of intact (green) and damaged DNA origami (red) have been highlighted. The DNA origami indicated in white and blue have not been considered for quantification because they are not completely visible in the AFM image and lie on top of each other, respectively.

4.2 Effect of Staple Age on DNA Origami Nanostructure Assembly and Stability

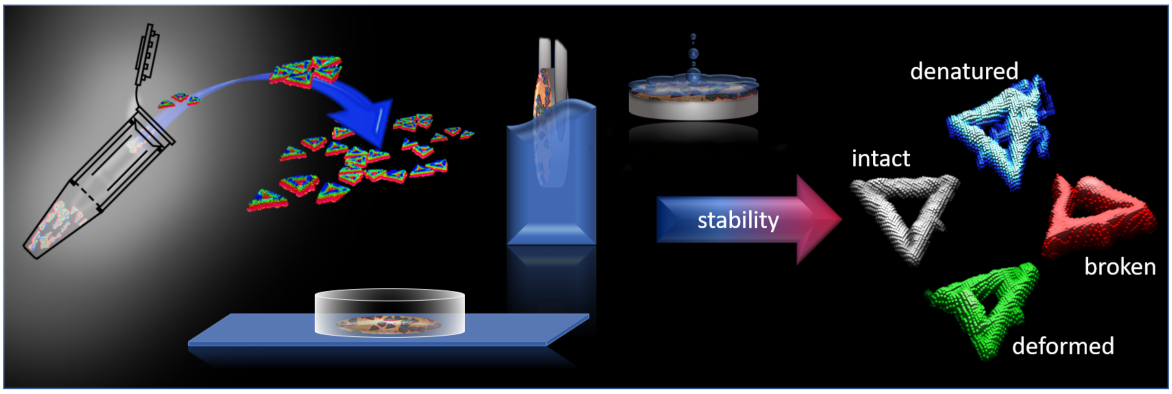

4.2.1 Introduction

While many applications for DNA origami mentioned in the introductory chapter of this work crucially rely on an intact DNA origami shape, many of them subject the employed DNA origami nanostructures to rather harsh treatments. Consequently, interest in the effects that environmental and processing conditions exert on DNA origami structural integrity has spiked in the last few years [84, 86, 89, 97, 129, 151, 162, 166, 174–178].

Another issue that is becoming more and more relevant in the context of such applications is the long-term stability of the DNA origami nanostructures under relevant storage conditions [133, 151, 179]. While it has been established that, even under low-magnesium conditions, DNA origami nanostructures remain structurally intact over a period of several months when stored at 4°C [133, 151], their storage at higher temperatures may result in quick deterioration [179]. This issue can be circumvented by the lyophilization of the DNA origami nanostructures prior to storage [179].

While the aforementioned studies have focused on the storage of readily assembled DNA origami nanostructures, this work investigates the effect of the long-term storage of the employed staple strands on DNA origami assembly and stability. AFM under liquid and dry conditions was employed to characterize the structural integrity of Rothemund triangles [23] assembled from different staple sets that have been stored at -20°C for up to 43 months. In addition to comparing liquid and dry imaging conditions, further different sample washing protocols were employed to simulate different harsh processing conditions. It was found that, while DNA origami assembly is largely unaffected by staple age, the assembled DNA origami triangles become gradually more sensitive toward harsh washing conditions as their staple age increased. Matrix-assisted laser desorption/ionization time-of-flight (MALDI-TOF) mass spectrometry investigations indicate that this is not a result of staple fragmentation but, rather, of damaged nucleobases. Finally, evidence is presented that these staple age-related effects depend on the DNA origami superstructure.

4.2.2 Results and Discussion

In order to ensure comparability between staple sets of different age, all staple strands were mixed immediately after purchase, divided into 150 μL aliquots, and stored at -20°C for 2 to 56 months as described in section 4.2.4.1. Therefore, all DNA origami samples were assembled from staple sets that have been frozen and thawed only once. For each DNA origami assembly, freshly defrosted tubes containing 10 μL of M13mp18 scaffold, aliquoted from a common stock solution, stored at -20°C were used. To minimize the influence of scaffold preparation, the differently-aged staple sets were assembled using the same scaffold stock solution originating from the same preparation. Furthermore, the age of the scaffold stock solution at the time of use was always identical for each of the differently-aged staple sets used in one sample treatment protocol and comparable to the youngest staple set in each time series (below 8 months).

Figure 4.13 b)–e) shows AFM images of Rothemund triangles assembled from staple sets of different ages. AFM imaging has been performed as described in sections 4.2.4.3 and 4.2.4.1. For comparison, a schematic representation of the duplex arrangement in the Rothemund triangle is given in Figure 4.13 a). Ideally, AFM images of the assembled DNA origami should perfectly match the scheme. The AFM images in the left column of Figure 4.13 b)–e) were recorded under liquid conditions in assembly buffer in order to assess any effects of staple age on the DNA origami assembly. Liquid imaging represents the least invasive AFM-based approach of analyzing DNA origami structural integrity at a nanometer resolution. Furthermore, it is frequently employed in DNA origami-based single-molecule studies [59, 60, 157, 180–183]. As can be seen in the inset of Figure 4.13 b) (left), the Rothemund triangle assembled from seven months old staples shows all features expected from the scheme in Figure 4.13 a). The three cavities in the corners of the triangle where the bridging staples connect the individual trapezoids are clearly visible, and even the seams in the centers of the trapezoids can be resolved. The overview image in Figure 4.13 b) (left) further suggests that the vast majority of Rothemund triangles are perfectly assembled, even though some small DNA origami fragments or broken/denatured triangles are occasionally observed. This general picture does not change significantly with increasing staple age. Even 43-month-old staples yield predominantly intact DNA origami triangles that show all the characteristic features of the design, indicating that staple age does not affect DNA origami assembly.

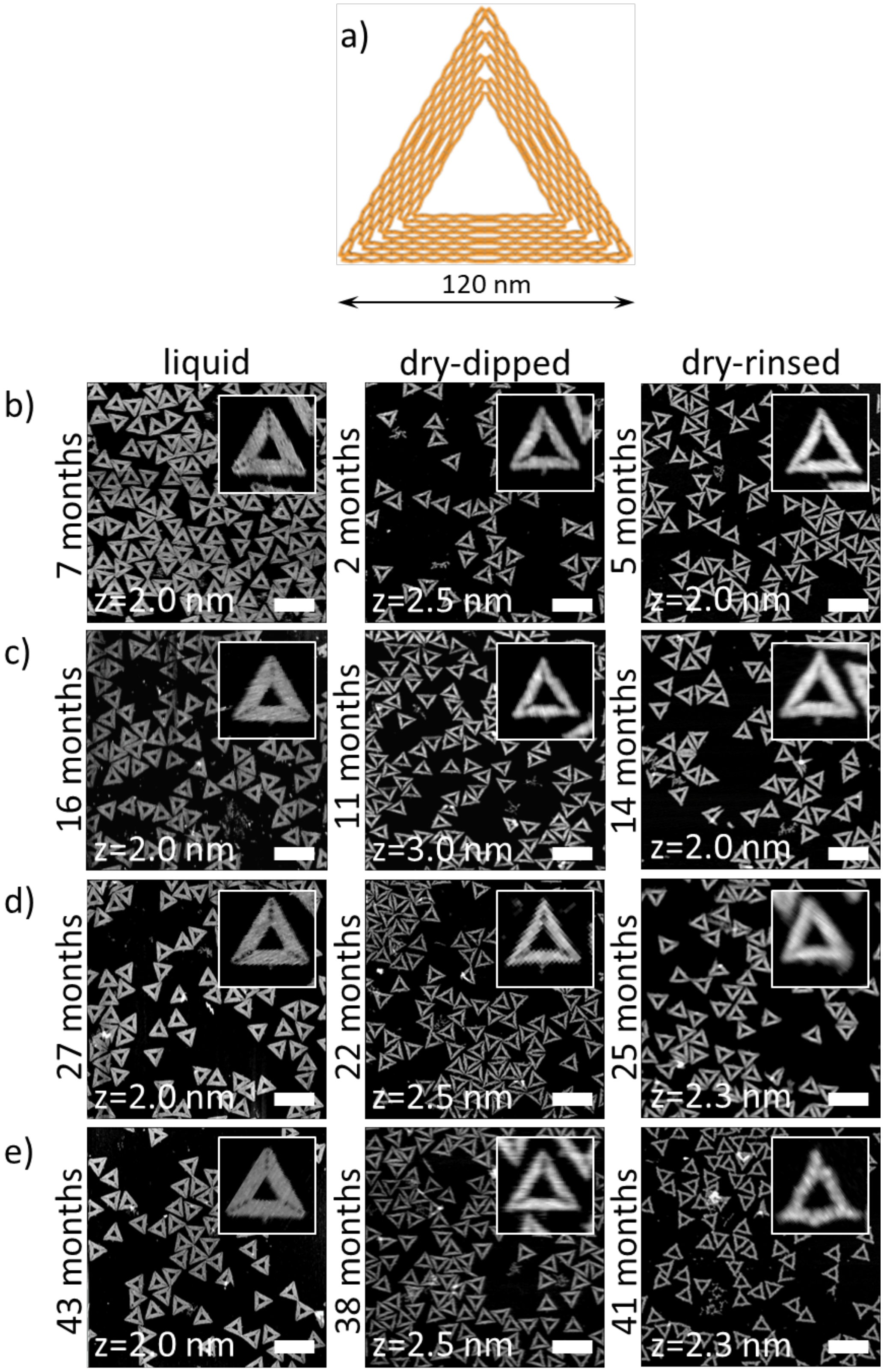
a)
120 nm
liquid
dry-dipped
dry-rinsed
b)
7 months
z=2.0 nm
2 months
z=2.5 nm
5 months
z=2.0 nm
c)
16 months
z=2.0 nm
11 months
z=3.0 nm
14 months
z=2.0 nm
d)
27 months
z=2.0 nm
22 months
z=2.5 nm
25 months
z=2.3 nm
e)
43 months
z=2.0 nm
38 months
z=2.5 nm
41 months
z=2.3 nm

Figure 4.13: AFM images of DNA origami triangles assembled from staple sets of different ages. a) Schematic illustration of the Rothemund triangle DNA origami. AFM images of DNA origami triangles assembled from staple sets aged for b) 2–7 months, (c) 11–16 months, d) 22–27 months, and e) 38–43 months. Measurements were performed either in liquid (left column) or dry conditions after gently dipping the sample into water (central column) or after harsh rinsing (right column). Scale bars represent 250 nm. Height scales are given in the individual images. The insets show zooms of individual DNA origami triangles.

For many applications, the DNA origami nanostructures have to be dried after immobilization on a substrate surface. This is in order to quench certain reactions of attached chemical species [184] or, more frequently, to enable subsequent processing steps [58, 112, 114, 119, 120, 185, 186]. In all of these cases, the substrate needs to be washed with water in order to remove residual salt from the surface. The gentlest way to do this is by dipping the sample into pure water for a couple of seconds [184]. While this dipping may result in the dislocation and rearrangement of the adsorbed DNA origami nanostructures [132, 187], it does not induce major damage of the Rothemund triangles [184].

The AFM image and the corresponding zoom of Rothemund triangles assembled from two-month-old staples shown in Figure 4.13 b) (center) reveal mostly intact DNA origami. Compared to liquid imaging, the triangular shapes appear less defined. This can be attributed both to drying-induced conformational alterations of the DNA duplexes in the DNA origami, such as B-A transitions, and minor shape distortions resulting from the removal of Mg^{2+} ions from the mica-DNA interface, which leads to a reduced strength of the interaction [138]. The latter is manifested, for example, in the decreased width of the trapezoids composing the triangles, which appear somewhat contracted or rolled up. Nevertheless, the cavities in the corners of the triangles can still be resolved, albeit not as separated cavities but as a groove. As for the measurements in solution, staple age does not seem to have a significant effect on DNA origami integrity. Even for 38-month-old staples, mostly intact triangles are observed after dipping.

For some applications of DNA origami nanostructures, gentle dipping of the substrate into water is not sufficient. This particularly concerns applications employing viscous buffer components or other molecular species that strongly adsorb to the substrate surface and need to be removed afterwards [89, 120, 162]. In such cases, the substrate surfaces are often rinsed with large amounts of water. The AFM image in Figure 4.13 b) (right) shows DNA origami triangles assembled from 5-month-old staples after such a rinsing treatment. The Rothemund triangles appear very similar to the ones subjected to dip-washing in Figure 4.13 b) (center), and there is no significant increase in the number of fragments and denatured DNA origami. Also, for Rothemund triangles assembled from 14-month-old staples(Figure 4.13 c), right), this rather harsh treatment does not seem to impair DNA origami integrity. At a staple age of 25 months, however, several Rothemund triangles with distorted shapes are observed in Figure 4.13 d) (right). The DNA origami in the corresponding inset appears somewhat swollen and has frayed edges with strongly rounded corners. It is also more difficult to identify the cavities in the corners of the triangles. These rinsing-induced shape distortions become even worse when 41-month-old staples are used for the DNA origami assembly. As can be seen in Figure 4.13 e) (right), the DNA origami still exhibits a roughly triangular shape. However, in this case, the trapezoids of many DNA origami are strongly deformed and bulging, and the cavities in the corners can no longer be identified.

In order to quantitatively evaluate the effects of staple age and treatment conditions on the structural integrity of the Rothemund triangles, the AFM images were analyzed by manually counting the fractions of intact, broken, deformed, and denatured DNA origami nanostructures. Figure 4.14 shows representative examples of these four categories. The results of the statistical analyses are shown in Figure 4.15 and Tables 4.4–4.6.

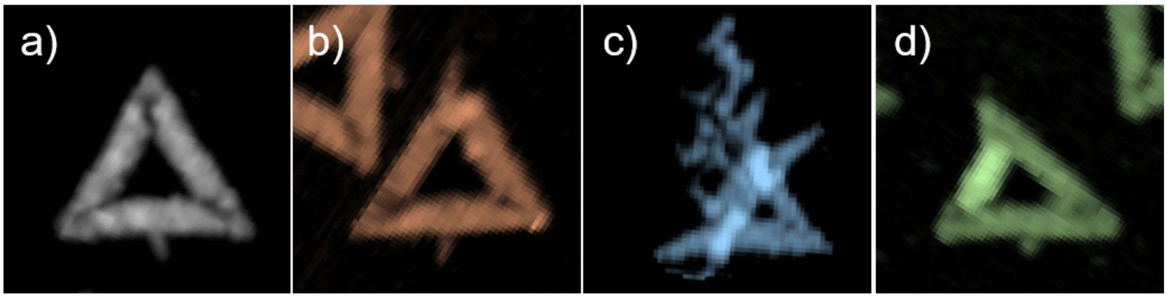

Figure 4.14: Representative AFM zooms of Rothemund triangles categorized as a) intact, b) broken, c) denatured, and d) deformed.

In the following, the general procedure for determining the yields given in Tables 4.4–4.6 is described. For dry imaging, two independent samples were analyzed per staple age. In case of liquid imaging, only one sample was analyzed per staple age. Five to ten AFM images were recorded per staple age. For each recorded AFM image, the different yields were determined by manual counting. Final yields were obtained by averaging over the yields obtained for the individual AFM images, with standard deviations as a measure of error. This is exemplified in Table 4.3 for the case of 38 months old staple strands and imaging under dry conditions after dip-washing.

Table 4.3: Number of analyzed DNA origami triangles $N_{(DNAorigami)}$ for each of the 8 AFM images recorded after dipping a sample assembled from 38 months old staples and the corresponding yields of intact, broken, deformed, and denatured DNA origami in %.

AFM image	$N_{(DNAorigami)}$	intact DNA origami / %	broken DNA origami / %	denatured DNA origami / %	deformed DNA origami / %
1	524	89.5	4.2	4.8	1.5
2	518	88.2	6.2	4.1	1.5
3	444	86.0	5.0	5.2	3.8
4	515	86.8	4.8	6.0	3.1
5	491	88.0	5.7	3.1	3.3
6	526	85.2	7.0	3.4	4.4
7	552	88.2	4.5	3.1	4.2
8	554	87.5	6.0	2.7	3.8
sum	**4124**	**87.4±1.4**	**5.4± 1.0**	**4.0±1.2**	**3.2±1.1**

Table 4.4: Yields (in %) of intact, broken, and denatured Rothemund triangles assembled from staples of different age obtained by AFM in liquid.

liquid				
months	intact	broken	denatured	$N_{DNAorigami}$
7	88.0±1.7	3.3±1.7	8.5±0.8	727
16	87.2±2.1	4.3±1.4	8.5±1.0	508
27	82.0±1.2	6.3±0.8	11.7±1.7	611
43	80.6±3.9	6.7±2.0	12.7±2.1	844

AFM imaging in liquid is the gentlest of the considered methods and, thus, expected to capture the solution state of the assembled DNA origami nanostructures. Nevertheless, Figure 4.15 a) shows that

Table 4.5: Yields (in %) of intact, broken, denatured, and deformed Rothemund triangles assembled from staples of different age obtained by AFM in the dry state after dip-washing.

dry-dipped					
months	intact	broken	denatured	deformed	$N_{DNAorigami}$
2	92.1±1.2	2.7±0.7	2.9±1.7	2.1±1.6	1967
11	90.9±0.9	4.0±1.2	3.4±1.0	1.6±1.4	3730
22	90.6±2.3	4.0±1.0	3.8±0.9	1.7±0.7	3728
38	87.5±1.4	5.4±1.0	4.0±1.1	3.2±1.1	4140

Table 4.6: Yields (in %) of intact, broken, denatured, and deformed Rothemund triangles assembled from staples of different age obtained by AFM in the dry state after rinsing.

dry-rinsed					
months	intact	broken	denatured	deformed	$N_{DNAorigami}$
5	87.8±2.9	4.4±0.8	5.1±1.1	2.7±2.1	2769
14	76.3±9.5	5.0±0.0	6.5±1.2	12.2±8.6	1880
25	64.8±17.2	5.0±2.3	5.4±1.0	24.8±18.4	2353
41	20.1±19.1	7.8±5.3	6.1±1.0	66.0±22.7	2353

the yield of intact DNA origami decreased from ∼ 88% at a staple age of 7 months to ∼ 81% at a staple age of 43 months. This is due to the slight increase in the fractions of broken and denatured DNA origami with increasing the staple age. Interestingly, this increase occurred rather suddenly at a staple age between 16 and 27 months. These data indicate that staples older than this threshold age result in slightly more damaged DNA origami nanostructures. However, it is not clear from our measurements if staple age is correlated with lower assembly yields of intact DNA origami or whether the assembled DNA origami are more easily damaged during sample handling and purification.

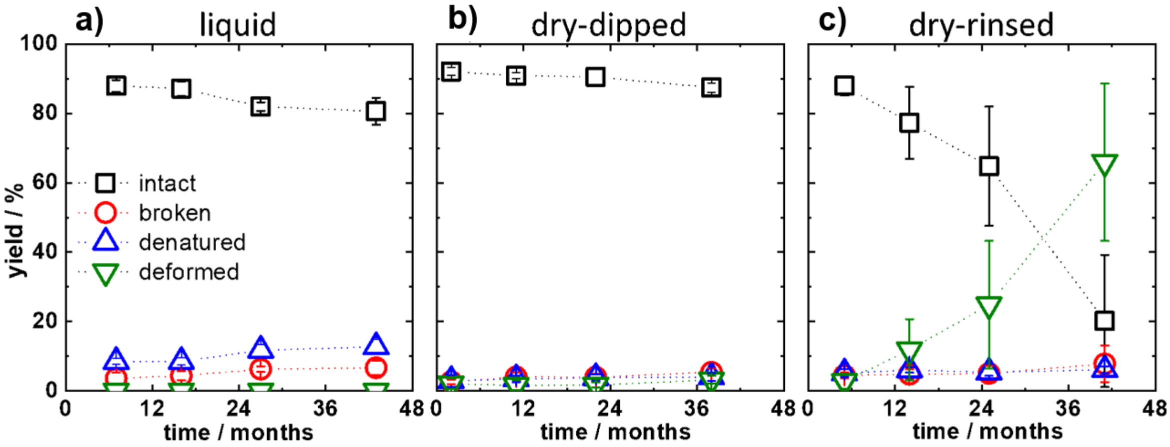

Figure 4.15: Yields of intact, broken, denatured, and deformed DNA origami depending on the age of the staple solution for a) measurements in liquid, b) measurements using the dry-dipped protocol, and c) measurements using the dry-rinsed protocol.

In Figure 4.15 b), the yields after dip-washing and drying the adsorbed DNA origami are given. Here, only a very small decrease in the fraction of intact DNA origami from 92% to 87% is observed. Interestingly, dip-washing seems to result in a higher yield of intact DNA origami adsorbed to the mica surface. This counterintuitive observation can be explained by the fact that broken and denatured DNA origami have a smaller surface and thus a smaller contact area with the mica surface. Damaged

DNA origami nanostructures are, therefore, more easily removed from the mica surface during dip-washing than intact ones, which superficially increases the measured yield of intact DNA origami.
In Figure 4.13, it was observed that substrate rinsing leads to significant shape distortions and deformations in the adsorbed Rothemund triangles at a staple age of 25 months and older. The results of the statistical analyses shown in Figure 4.15 c), however, show a significant decrease in the fraction of intact DNA origami already at a staple age of 14 months. The yield of intact DNA origami decreases from 88% at 5 months to only 76% at 14 months. At a staple age of 41 months, only 20% of the Rothemund triangles are still intact after rinsing. This is due to a strong increase in the yield of deformed DNA origami from only 3% at 5 months to 66% at 41 months staple age. Interestingly, the fractions of broken and denatured DNA origami are hardly affected by the staple age and remain in the range of 4% to 8%.
Our results indicate that the frozen staple strands are slowly degraded during storage. However, the fact that AFM imaging in liquid shows predominantly intact DNA origami even for the oldest staple sets implies that DNA origami assembly itself is only mildly affected by staple age. Rather, the assembled DNA origami nanostructures appear to become more sensitive toward environmental conditions. Therefore, it was speculated that the staple strands are not fragmented during storage as this would result in the assembly of fewer intact DNA origami, but rather experience some sort of base damage that interferes with base pairing or stacking. In order to test this hypothesis, the compositions of the complete staple mixtures has been analyzed by MALDI-TOF mass spectrometry [152]. All spectra looked identical regardless of staple age, and there was no apparent shift of individual peaks towards lower masses, thus any degradation or other fracturing of whole staple strands can be excluded.

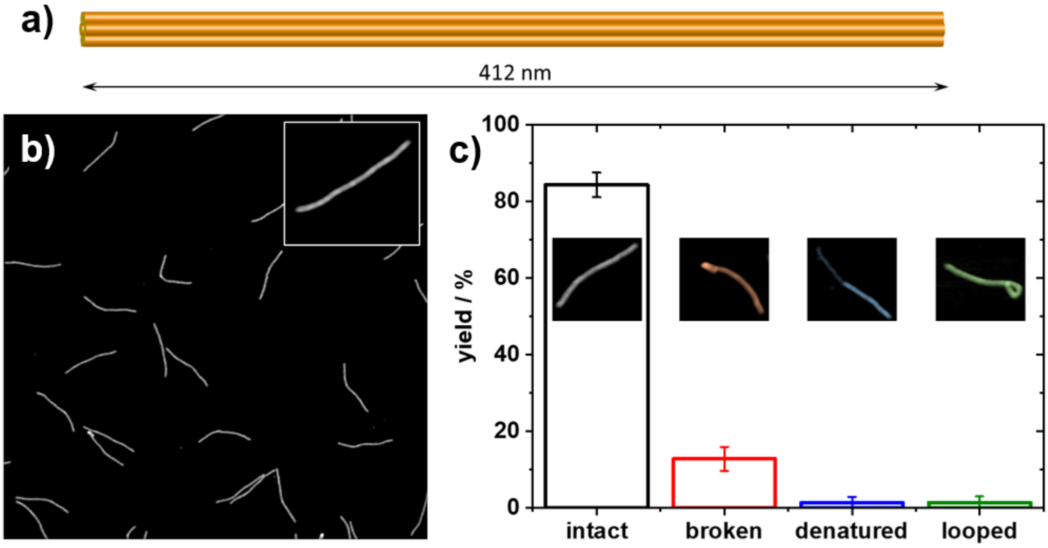

Figure 4.16: Stability results for 6HB DNA origami. Schematic illustration a) and AFM image of DNA origami 6HBs assembled from 56 months old staples after rinsing b). Scale bar and height scale is 500 nm and 2.0 nm, respectively. The inset shows a zoom of an individual 6HB. c) Corresponding yields of intact, broken, denatured, and looped DNA origami 6HBs. The insets show examples of the individual categories. Scaffold age at the time of use was one month.

Finally, it has been investigated whether these staple age-related effects also depend on DNA origami superstructure. The Rothemund triangle is designed on the square lattice and thus highly strained, and furthermore, its open, sheet-like structure offers no additional architectural stability apart from direct connections via crossovers to the neighboring helices. These two design factors may render it more susceptible to washing-induced damage than other DNA origami nanostructures. Therefore, also DNA origami 6HBs assembled from 56 months old staples have been subjected to the rinsing treatment and evaluated the effect by AFM. As can be seen in Figure 4.16, the 6HBs turn out to be much more robust than the Rothemund triangles and barely show any damage, with about 85% of the 6HBs remaining intact. This is in agreement with previous observations that these particular DNA origami nanostructures show extraordinary high stability under denaturing conditions [97, 151].

4.2.3 Conclusion

In summary, the effect of staple age on DNA origami assembly and stability using AFM under liquid and dry conditions has been investigated. DNA origami assembly is only mildly affected by staple age, yielding about 80% of intact Rothemund triangles when using a staple mixture stored for 43 months at -20°C. However, the assembled Rothemund triangles become more sensitive toward environmental conditions with increasing staple age. In particular, the older the employed staples, the more deformed triangles are observed in AFM images recorded after extensive sample washing and drying. At a staple age of 41 months, this rinsing treatment results in 66% of the DNA origami showing significant shape distortions.

Since no staple fragments could be detected in the aged staple mixtures by MALDI-TOF mass spectrometry, the increased DNA origami sensitivity can be attributed to an accumulation of damaged nucleobases which undergo weaker base-pairing interactions, resulting in reduced duplex stability. The mechanical forces acting on the adsorbed Rothemund triangles during rinsing in combination with the depletion of stabilizing Mg^{2+} salt bridges then lead to the dehybridization of some particularly weak staple strands from the scaffold and subsequent rearrangement of the remaining duplexes within a given DNA origami, which finally results in the observed shape distortions. Unfortunately, the exact nature of the storage-induced base damage is very hard to assess because of the experimental complications arising when analyzing a mixture of about 200 non-purified oligonucleotides with different sequences and lengths. However, the different reaction rates displayed by the different types of spontaneously occurring nucleobase damage may provide some indication of the predominant type of damage. For instance, hydrolytic deamination of cytosine in single-stranded DNA occurs with a half-life of about 200 years, while deamination of the other bases is much slower [188]. Hydrolytic depurination in single-stranded DNA occurs at similar half-lives around 100 years, while the loss of pyrimidine bases is slower by several orders of magnitude [188]. Because of these long reaction times, hydrolytic deamination and base loss appear rather unlikely candidates for the formation of excessive nucleobase damage in frozen oligonucleotides over a time course of a few years. On the other hand, OH radical-driven oxidative base damage such as the generation of 8-oxoguanine or ring-opened lesions in guanine and thymine occurs much faster with half-lives of the order of hours [188]. Furthermore, oxidative base damage has been shown to result in the destabilization of the DNA duplex [189, 190]. Therefore, it can be assumed that oxidative base damage is the origin of the observed increase in DNA origami sensitivity.

Our results reveal a complex interplay between staple storage, DNA origami treatment conditions, and the DNA origami superstructure. If the assembled DNA origami nanostructures are employed only in liquid under mild environmental conditions and using appropriate buffers [151], staple age will not play a significant role at all. In the case of harsh environmental conditions, such as excessive sample rinsing (as demonstrated here), exposure to denaturing buffer conditions [89, 162], or elevated temperatures, the structural integrity of the DNA origami may be seriously impaired if staples older than a few months are used. As it has been demonstrated, however, the degree of staple age-induced damage may drastically depend on the DNA origami superstructure, and this needs to be evaluated individually for each DNA origami design under the relevant conditions. Finally, should be stressed that the above experiments were conducted with staple mixtures dissolved in pure water that have been frozen and thawed only once. Repeated freezing and thawing cycles may induce more serious damage and have more devastating effects on DNA origami assembly and structural stability than observed here. On the other hand, the use of buffers instead of pure water may reduce the negative effects of long-term storage [191]. Furthermore, since oxidative base damage appears to be the most likely origin of the observed increase in DNA origami sensitivity, the addition of antioxidants may also improve the quality of the staple strands after long-term freeze storage.

4.2.4 Materials and Methods

4.2.4.1 Preparation and storage of the staple strands

Immediately upon delivery, the freshly synthesized staple strands (Metabion), dissolved at 100 μM concentration in pure water, were mixed at equal concentrations to yield the complete staple mixture. This stock solution was then divided into 150 μl aliquots and stored at -20°C in the dark.

4.2.4.2 Preparation of DNA origami samples for AFM analysis

In liquid, 10 μl of the 3 nM DNA origami solution were pipetted onto a freshly cleaved mica surface in a liquid cell and incubated for 1 minute. The DNA origami solution has been prepared as described in section 4.1.4.1. Then, the cell was filled with 1 ml of 1 x TAE/$MgCl_2$.
Under Dry-dipped, 10 μl of the 3 nM DNA origami solution were incubated for 1 min on freshly cleaved mica. The mica substrate was then vertically dipped into pure water for 10 seconds and blown dry with a stream of ultra-pure air at an angle of 45° with respect to the substrate surface.
Under Dry-rinsed, 10 μl of the 3 nM DNA origami solution were incubated for 1 min on freshly cleaved mica. The mica substrate was then rinsed 5 times with 2 ml of pure water at an angle of 45° with respect to the substrate surface using a pipette. Thereafter, the sample was blown dry with a stream of ultra-pure air at an angle of 45° with respect to the substrate surface.

4.2.4.3 AFM imaging

AFM imaging in air was carried out using a JPK Nanowizard ULTRA Speed, an Agilent 5100 and Agilent 5500 AFM, respectively, operated in intermittent contact mode. AFM imaging in liquid was carried out using a JPK Nanowizard ULTRA Speed. For measurements under dry and liquid conditions, HQ-NSC18/AlBS (MikroMasch) and USC-F0.3-k0.3 cantilevers (NanoWorld) were used, respectively.

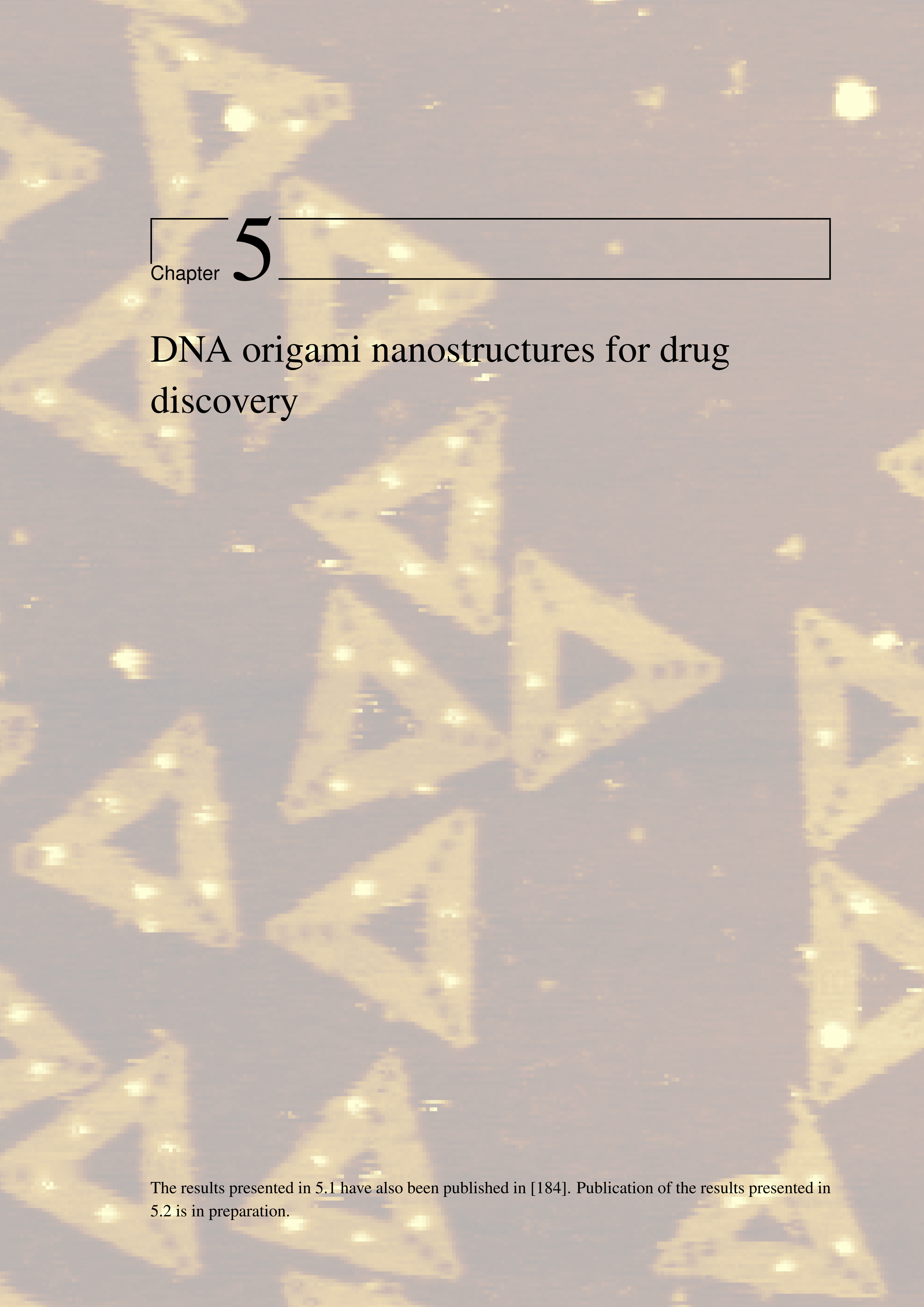

Chapter 5

DNA origami nanostructures for drug discovery

The results presented in 5.1 have also been published in [184]. Publication of the results presented in 5.2 is in preparation.

5.1 DNA origami based single-molecule assay for fragment-based drug discovery

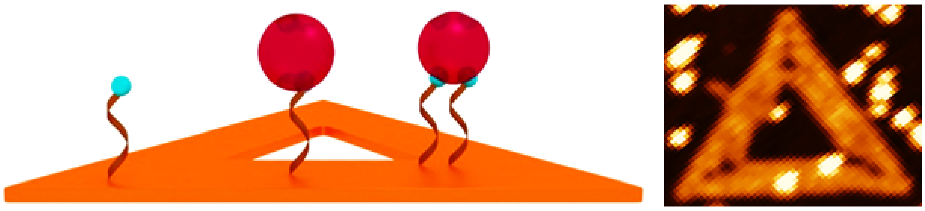

5.1.1 Introduction

The identification of small molecules that can selectively interact with protein targets of biomedical importance represents a central problem in chemical biology and drug discovery. Great advances have been made, using DNA-encoded chemical libraries (DECLs) for lead discovery [192, 193]. The DNA-conjugated chemical structures can either be assembled and probed as addressable arrays on planar surfaces [194–197] or be subjected to selection procedures as a mixture of barcoded compounds in solution [198, 199]. Moreover, the DNA-encoded compounds can be displayed either as single pharmacophores or as fragment pairs [192]. The latter is particularly attractive for fragment-based drug discovery as DNA provides a versatile platform for combining and arranging different fragments. However, selection experiments with DECLs in solution often require immobilized proteins on solid supports, causing undesired effects on protein structure and function [200]. Array technology utilizes fluorescently labelled proteins or antibodies for detecting protein binding, which can cause chemical or steric interference with protein-ligand interactions [201]. The problems associated with current methods could be circumvented by direct interrogation of protein-ligand interactions at a single-molecule level with unmodified proteins.

DNA origami [23] enables the investigation of biomolecules at a single-molecule level [57]. Here, a single-stranded DNA scaffold is folded into a nanoscale shape upon hybridization with many specifically designed oligonucleotide staple strands [23]. The specific modification of selected staples enables the spatially selective decoration of the DNA origami nanostructure with target-specific probes at nanometer precision, rendering DNA origami nanostructures excellent substrates for the detection of single biomolecular binding events.

This work is aimed at utilizing the DNA origami technique to fabricate miniaturized arrays of DNA-conjugated low-molecular-weight compounds that can be employed in screening campaigns for the discovery of small-molecule protein inhibitors. In combination with AFM as a single-molecule detection method, it will pave the way to combining the direct detection of protein-ligand interactions using the array technique with miniaturized feature size.

The binding of SAv to Bt, (see scheme 5.14) is frequently used as a model system for probing protein-ligand interactions. However, the fM affinity of SAv to Bt is not representative of protein-ligand interactions as the K_d values between target proteins and lead compounds are often in the high nM to low μM range. Iminobiotin (iBt, see scheme 5.14) on the other hand is a Bt derivative with moderate affinity to SAv ($K_d = 13\ \mu$M) [202]. Moreover, as SAv is a homotetramer, bidentate binding of two iBt assembled in close proximity by a DNA duplex has been used as a model system for fragment-based lead discovery [202, 203]. Connecting two iBt with a flexible linker resulted in a bidentate SAv binder with a K_d of 6 nM [202]. Given that many target proteins do not have symmetric binding pockets, α-1-acid glycoprotein (AGP) [204] and trypsin [205] have also been uses as model systems, which both have previously been shown to undergo bidentate binding to two different fragments assembled by a DNA duplex [203, 206].

5.1.2 Results and Discussion

Nanoarrays of various pharmacophores (scheme 5.14 in section 5.1.4.2) were constructed on triangular DNA origami nanostructures (Figure 5.1). The DNA origami triangles have an edge length of about 120 nm, are comparatively rigid, and show high stability under conditions much harsher than those commonly used in protein-ligand binding assays [89]. Pharmacophores were attached to selected staples via spacers of unpaired thymines to ensure some conformational freedom. In addition to the pharmacophores under investigation, each DNA origami carried at least one biotin modification at a specific position that was used as a reference to enable unambiguous hit identification (Figure 5.1).

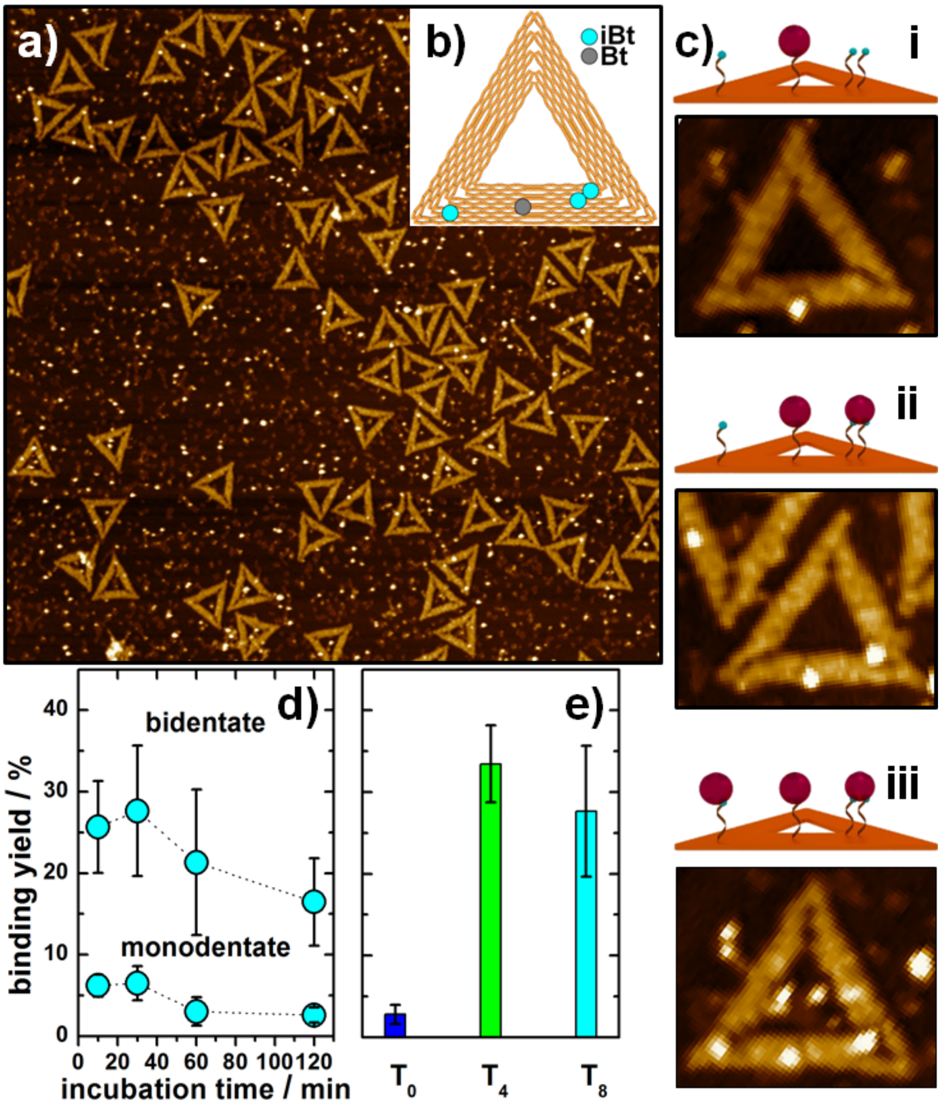

Figure 5.1: a) Representative AFM image of iBt nanoarrays (5 nM) taken after incubation with 250 nM SAv for 30 min. The image size and height scale is $1.5\times1.5\ \mu m^2$ and 4.2 nm, respectively. b) Schematic of the DNA origami substrate indicating the positions of the modified staple strands. c) Schematics and corresponding AFM zooms of single DNA origami substrates exhibiting i) no SAv bound to iBt, ii) bidentate binding of SAv to iBt, and iii) monodentate and bidentate binding of SAv to iBt. d) Binding yields for monodentate and bidentate SAv-iBt binding as a function of incubation time. e) Bidentate SAv-iBt binding yields for different spacer lengths obtained for 30 min incubation.

Table 5.1: Determined binding yields for monodentate and bidentate SAv-iBt binding depending on the incubation time as presented in Figure 5.1 d). $N_{(DNAorigami)}$ denotes the total number of DNA origami substrates considered.

Incubation time / min.	$N_{(DNAorigami)}$	Monodentate binding yield / %	Bidentate binding yield / %
10	699	6.2 ± 1.4	25.7 ± 5.6
30	760	6.5 ± 2.1	27.6 ± 8.0
60	1045	3.0± 1.7	21.3± 8.9
120	476	2.6 ± 0.9	16.5 ± 5.4

The DNA origami triangles were first decorated with three iBt molecules as shown in Figure 5.1 b). The position left of the central Bt modification exhibited a single iBt, while the position on the right featured two iBt molecules in close proximity to enable bidentate binding to SAv. The latter was realized by attaching the iBt modifications to the 5' and the 3' ends of two neighboring staples (see Figures 5.15 and 5.16). An asymmetric arrangement of the ligand-displaying sites was chosen, in which the single iBt on the left was located at the outer vertex of the triangle, while the iBt pair on the right was situated next to the vertex of the internal triangular cavity. Using the Bt site as an indicator of the outer edge position of the single iBt, different binding events can be clearly distinguished.

After incubation with SAv for different durations, the DNA origami substrates were immobilized on mica and imaged by AFM (see Figure 5.1 a)). In the following, the general procedure for the determination of the reported binding yields is described in detail for the DNA origami system carrying the modifications for mono- and bidentate binding of SAv to Bt. For each reported yield, two to three samples have been prepared under identical conditions as described in the previous sections. All samples carried one or two Bt-modifications which after SAv binding serve as an internal reference. The main purpose of this internal reference is to enable reliable distinction between specific binding events to the pharmacophore modifications and unspecific adsorption to the DNA origami substrate at random positions. Only DNA origami substrates that featured a SAv bound to the central Bt position were analyzed, to avoid false positives caused by defects of the nanostructures or promiscuous binding of target proteins. For the determination of the reported binding yields, only DNA origami substrates were considered that showed stoichiometric SAv-Bt binding, i.e., full occupation of the Bt sites. In order to account for local yield variations across the sample surface, e.g., due to inhomogeneities in sample washing, between 3 and 10 AFM images were taken at random positions on the surface of each mica sample.

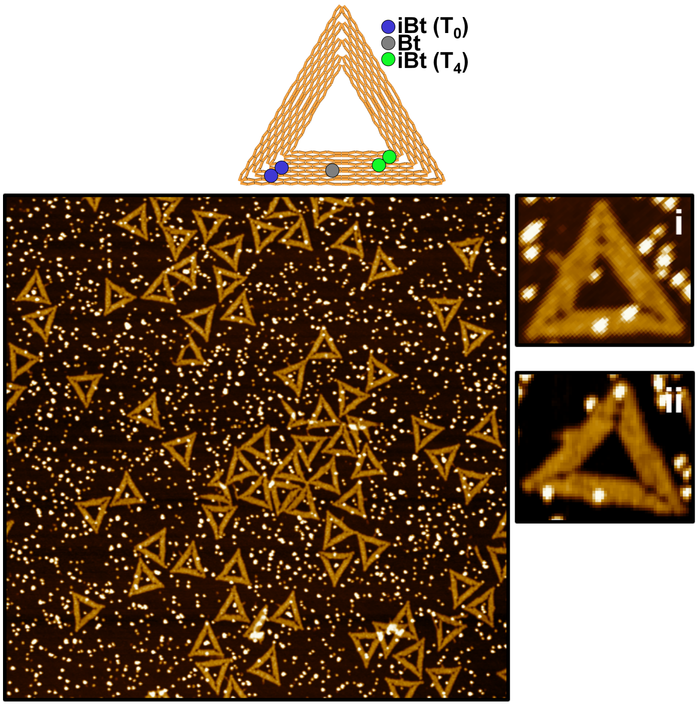

Figure 5.2: Representative AFM image of iBt nanoarrays (5 nM) with different spacer lengths as shown in the scheme, taken after incubation with 250 nM SAv for 30 min. The image size and height scale is $1.5 \times 1.5\ \mu m^2$ and 3.6 nm, respectively. i) and ii) show zooms of single DNA origami substrates exhibiting SAv bound to iBt with i) T_4 and ii) T_0 spacers.

Figure 5.2 shows a representative AFM image for a DNA origami system carrying two Bt modifications with a T_4 and a T_8 linker respectively. For each AFM image, the binding yield was determined by manual counting of the occupied pharmacophore positions relative to the number of considered DNA origami substrates. The reported yields are given as the averaged individual binding yields of the different AFM images with the standard deviation as error.

In order to unambiguously identify occupied binding sites, high quality AFM images have to be recorded that are free from obvious tip artifacts and large protein aggregates. Therefore, AFM images of low quality have been discarded and not considered in the statistical yield determination. Examples of low, medium, and high quality images are shown in Figure 5.3. Furthermore, DNA origami exhibiting visible defect such as broken corners or missing sections were not included in the analysis, even if the bound proteins could be identified.

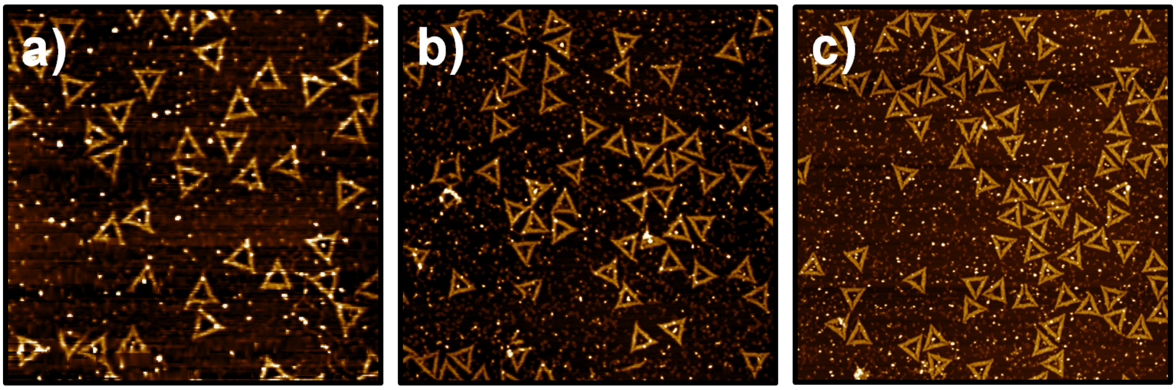

Figure 5.3: Sample AFM images of different quality. a) Poor quality image that has not been analyzed for yield determination. b) Medium quality image that allows identification of occupied binding sites and has been analyzed and included in the statistical yield determination. c) High quality image that has been analyzed and included in the statistical yield determination.

When counting proteins specifically bound to pharmacophore modifications on DNA origami substrates, one has to take into account that the absolute position of the bound protein on the DNA origami may be subject to fluctuations due to the finite length of the spacers and possible structural distortions of the adsorbed DNA origami. The resulting lateral variability is depicted in Figure 5.4.

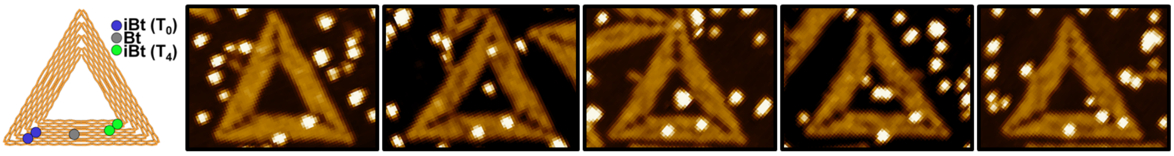

Figure 5.4: Scheme and AFM zooms of single DNA origami showing bidentate SAv-iBt binding with spacer length T_4, as well as monodentate SAv-Bt binding with spacer length T_8. The finite length of the spacers and structural distortions of the DNA origami result in variations in the absolute positions of the bound SAv molecules. The rightmost picture additionally shows an unspecifically adsorbed SAv at the lower right corner of the triangle.

As can be seen in the AFM zooms shown in Figure 5.4, sometimes also unspecific binding events can be observed on the DNA origami substrates. These predominantly occur in the seams connecting the three trapezoids that compose the triangle and feature some holes which expose the underlying mica surface. This can be avoided in future experiments by employing a different DNA origami substrate that does not have one of those holes. In some cases, however, also unspecific adsorption of proteins on the trapezoids of the triangle can be observed which probably occurs during sample drying. The contribution of such nonspecific binding events to the determined binding yields have been evaluated by employing a DNA origami design that features only the central Bt modification but no iBt modifications and counting SAv molecules nonspecifically immobilized at the iBt positions (see Figure 5.5). For the left and right position, a false-positive yield of 1.2% and 4.3% was obtained, respectively. These false-positive yields are significantly lower than the determined binding yields of 6.5% and 27.6% for mono- and bidentate SAv binding, respectively.

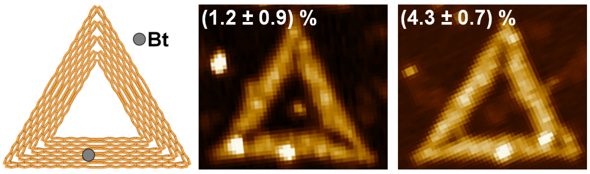

Figure 5.5: Scheme and AFM zooms of single DNA origami showing nonspecific SAv binding to the left and right iBt positions. The SAv concentration was 250 nM. The obtained false-positive yields are given in the figure.

Another point to consider is that the DNA origami can adsorb on the mica substrate in two different orientations, i.e., either face up or face down. Since protein binding is performed in bulk solution, adsorption geometry does not affect binding yields. Furthermore, as is shown in Figure 5.6, even in the face-down geometry, bound proteins can be easily resolved in the AFM images. However, care has to be taken during image analysis, as the face-down geometry results in a mirror image of the pharmacophore nanoarray. This is achieved by considering the orientation of the internal references which are arranged to break the symmetry of the DNA origami substrate (see Figure 5.6).

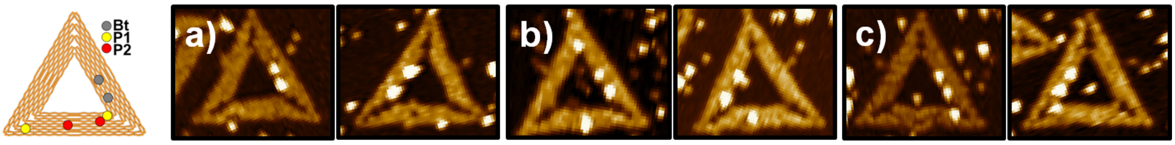

Figure 5.6: Scheme and AFM zooms of single DNA origami showing AGP binding to P1 (a), P2 (b), and P1+P2 (c), respectively. Left images show the face-up geometry, right images the mirrored face-down geometry.

As an example, the determination of binding yields for monodentate and bidentate SAv-iBt binding at an incubation time of 30 min (Figure 5.1 d) of section 5.1.2) is shown in detail. For this respective data point, five AFM images were recorded for three different samples. As already mentioned, only DNA origami showing full SAv occupation at the Bt sites were taken into account, resulting in this case in 760 analyzed DNA origami substrates. Figure 5.7 shows an AFM image from the respective sample series. In order to obtain the reported binding yields, firstly the binding yields for all of the five AFM images as shown in Table 5.2 were determined. The reported binding yields given in the last row of Table 5.2 were then obtained by averaging over the five images with the respective standard deviation as given as error. All other reported yields were determined analogously.

Table 5.2: Determination of monodentate and bidentate binding yields for SAv-iBt binding at an incubation time of 30 min (Figure 5.1 d) of the chapter 5.1.2). $N_{(DNAorigami)}$ denotes the total number of DNA origami substrates considered.

AFM-Image	$N_{DNAorigami}$	Monodentate yield / %	Bidentate yield / %
1	168	7.1	28.6
2	163	4.5	22.3
3	164	8.7	38.6
4	168	8.1	30.9
5	97	4.1	17.8
sum	**760**	**6.5 ± 2.1**	**27.6 ± 8.0**

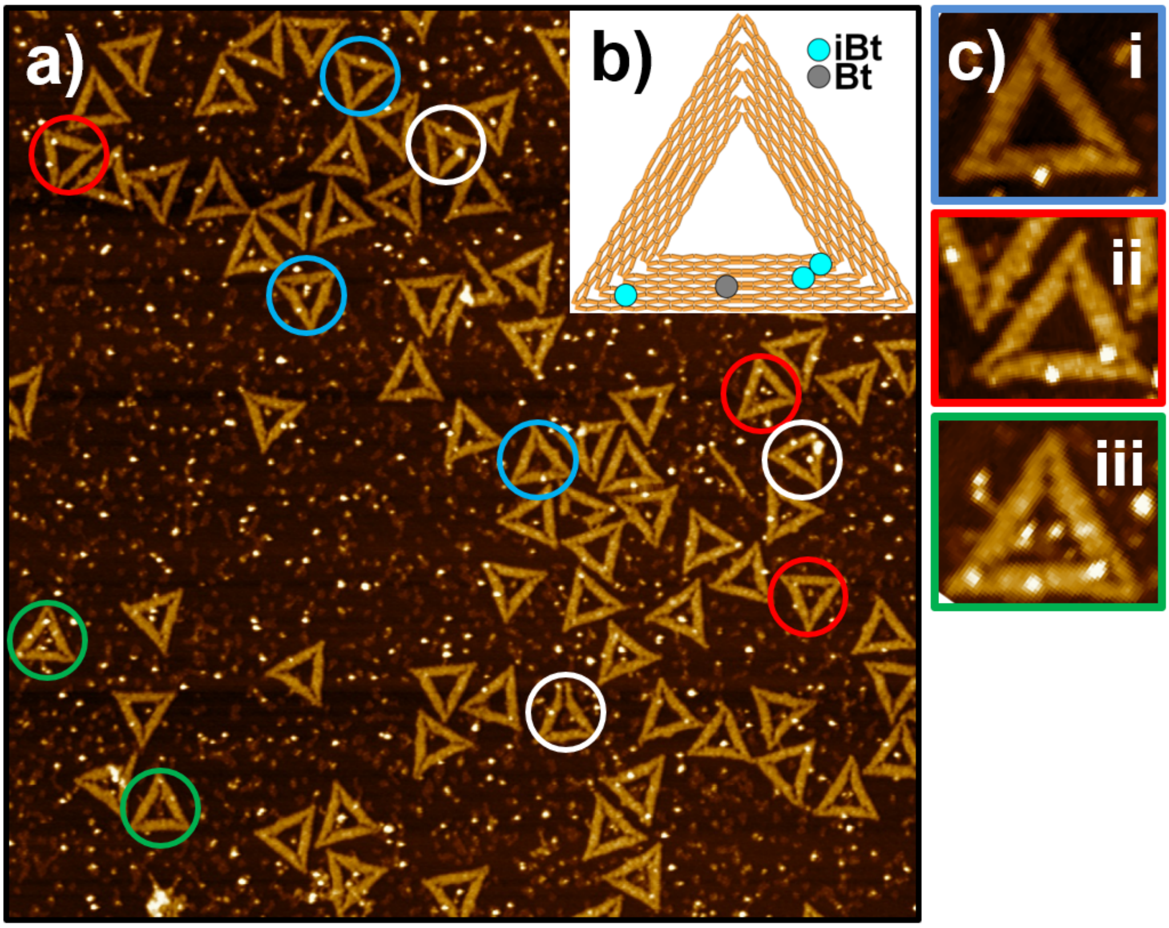

Figure 5.7: Representative AFM image used for determination of the binding yield. Several DNA origami can be found with reference only (blue circles), bidentate SAv-iBt binding only (red circles) and monodentate SAv-iBt binding (green circles). The white circles mark examples of defect DNA origami which have not been included in the statistics.

Table 5.3: Determined binding yields for bidentate SAv-iBt binding depending on the spacer lengths as presented in Figure 5.1 e). $N_{(DNAorigami)}$ denotes the total number of DNA origami substrates considered.

Spacer length	$N_{(DNAorigami)}$	Bidentate binding yield / %
T_0	1264	2.8 ± 1.2
T_4	1264	33.4 ± 4.7
T_8	760	27.6 ± 8.0

As shown in Figure 5.1 d), SAv binding to the iBt pair has higher yields than monodentate binding to the single iBt. Both yields always differ by more than a factor of three, thus indicating a dominant contribution from bidentate SAv-iBt binding. It is important to note that single-molecule measurements of spatially defined ligand pairs on DNA origami substrates do not suffer from the complications associated with avidity in conventional chip-based biosensor detection, where immobilization results in the random arrangement of fragments at an only statistically defined average distance [64]. In addition, no significant influence of incubation time on both binding yields is observed, indicating that the system reached equilibrium already after 10 min. Only after incubation for more than 60 min, a small decrease of the binding yields is visible which may be caused by denaturation and non-specific adsorption of SAv.

In the above nanoarray, the iBt modifications were attached to the staple strands via spacers of 8 thymines. However, the length of the spacers will directly affect bidentate binding yields because it controls the lateral distance between the two pharmacophores. If the spacers are too short, the two pharmacophores will not be able to bind to both pockets of the protein. The inverse effect that too large ligand distances lead to reduced binding has already been observed for bidentate thrombin-aptamer binding on DNA origami substrates [69]. Therefore, it has been investigated how different spacer lengths contribute to the bidentate binding of iBt to SAv by reducing the spacer lengths to 4 and 0 thymines, respectively (Figure 5.1 e)). For T_4 and T_8 spacers, similar bidentate SAv-iBt binding yields are observed in Figure 5.1 e). However, further reducing the spacer length to zero results in a dramatic decrease of the binding yield because the two iBt have a distance of less than 1 nm which is not sufficient for them to reach both SAv binding pockets simultaneously. Consequently, a binding yield close to that of monodentate SAv-iBt binding is obtained for this geometry. It is necessary to note that Bt shows strong monodentate SAv-binding even in the absence of any spacer, thus ruling out electrostatic repulsion or steric hindrance as the sole cause of reduced bidentate SAv-iBt binding (see Figure 5.8).

In particular, it was observed that SAv binding is efficiently suppressed in the absence of a single-stranded spacer sequence. In order to verify that this is indeed due to the spacers being too short to facilitate bidentate binding and not a result of electrostatic repulsion or steric hindrance, monodentate SAv binding to Bt attached to the DNA origami either directly without any spacer sequence (T_0) or with a T_8 spacer have been compared. As can be seen in Figure 5.8, both designs show strong SAv-Bt binding at yields comparable to those reported previously for other spacer sequences [58]. The small differences in binding yield may be attributed to different synthesis yields and different strand incorporation probabilities [207].

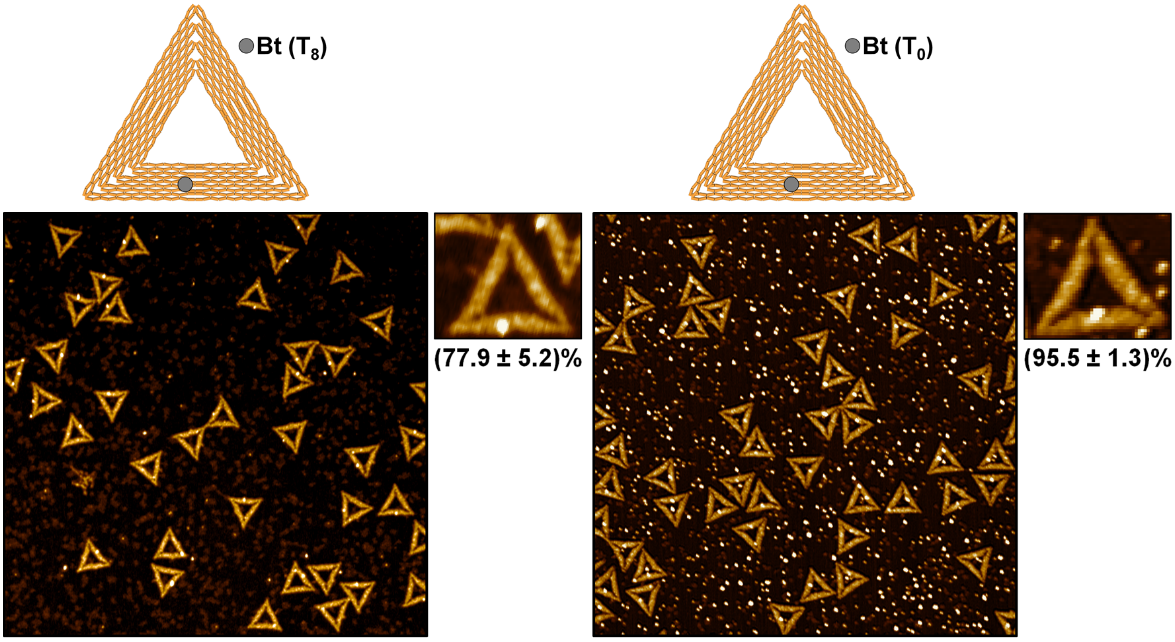

Figure 5.8: Schemes and AFM images of DNA origami triangles with single Bt modifications attached via different spacer lengths (T_8 and T_0). The SAv and DNA origami concentration was 250 nM and 5 nM, respectively. The incubation time was 30 min. The images have a size of $1.5\times1.5\ \mu m^2$ and height scales of 3.0 nm (left) and 4.2 nm (right), respectively. The obtained SAv binding yields are given in the figure.

Therefore, the existance of an optimum spacer length that results in maximum bidentate binding is proposed, whereas for shorter and also longer spacers will result in reduced bidentate binding yields (see Figure 5.9). For too short spacers, the two pharmacophores are too close for both of them simultaneously reaching their respective binding pockets in the protein (see Figure 5.9, left). In this case, binding will be monodentate and dominated by the stronger binder (the red pharmacophore in Figure 5.9). However, reduced binding will also be observed of the spacers are too long (Figure 5.9, right). This is because the ssDNA spacers used in this experiments (i) behave like entropic springs that cannot arbitrarily be compressed, (ii) are negatively charged so that neighboring spacers in a bidentate geometry will repel each other. Furthermore, (iii) spacer length directly correlates with fragment mobility and conformational freedom, so that longer spacers may reduce the probablity of both fragments simultaneously binding to two distinct binding pockets. Therefore, also for too long spacers, binding will be monodentate and dominated by the stronger binder.

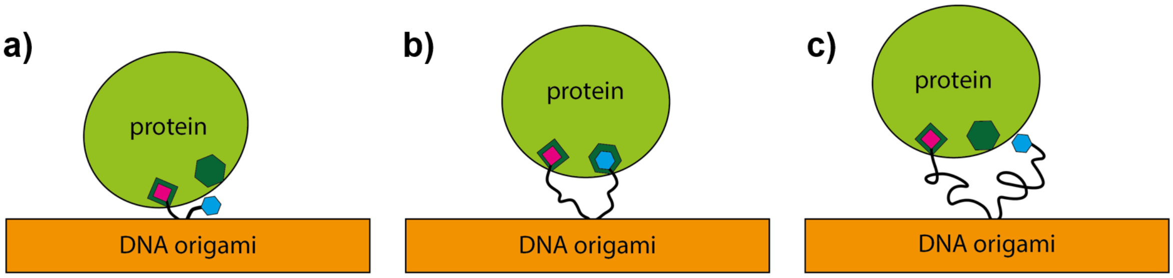

Figure 5.9: Scheme of bidentate protein binding to two pharmacophores attached to the DNA origami substrate with too short a), optimized b), and too long spacers c), respectively.

This result demonstrates that pharmacophore nanoarrays on DNA origami substrates can be used not only to identify potent fragment pairs but also their optimal spatial arrangement. The latter information is very important for transforming identified fragments into potent bidentate binders using medicinal chemistry methods.

Bidentate protein binding to two different pharmacophores was investigated using AGP as a model protein. AGP is an acute phase protein that has the ability to bind and carry numerous basic and neutral lipophilic drugs. The two AGP-binding pharmacophores P1 and P2 (scheme 5.14) have been arranged on the DNA origami substrate as shown in Figure 5.10 a). The distance between P1 on the left and P2 in the center is about 30 nm, thus preventing bidentate AGP-binding, whereas at the P1+P2 site on the right, the fragments have again been attached to neighboring staples without any gap inbetween (see Figures 5.15 and 5.16). Two Bt modifications were introduced as well to break the symmetry of the DNA origami triangle and enable binding site identification. Figure 5.10 d) shows the determined yields of AGP binding to P1, P2, and P1+P2. Monodentate binding to P2 is stronger than to P1, while binding to P1+P2 has a slightly higher yield than for P2 alone. The binding affinity of P1-DNA and P2-DNA to AGP has also been measured using microscale thermophoresis [184]. While P1-DNA was found to be a very weak AGP binder, P2-DNA has a K_d of 390 ± 170 nM. This is in qualitative agreement with the monodentate binding yields determined in Figure 5.10 d). P1+P2-DNA duplex showed a K_d of 8.2 ± 1.2 nM [184], which is close to that reported for bidentate iBt-SAv binding [202]. In contrast to what could be expected on the basis of these similar K_d values, however, the determined yields for P1+P2 binding to AGP on DNA origami and bidentate iBt-SAv binding in Figure 5.1 d) are quite different. This can be attributed to the spacer length (T_8) which has not been optimized toward maximum AGP binding. The only moderate increase of the P1+P2 binding yield compared to the drastically reduced K_d measured for the P1+P2-modified DNA duplex (which features only rather short linkers but no single-stranded spacers, see materials and methods 5.1.4) suggests that the spacers used in this nanoarray are too long to facilitate simultaneous binding of both fragments to their corresponding binding pockets in the protein (see Figure 5.9). Nevertheless, even for this non-optimized condition, significant differences in binding yield are observed as indicated in Figure 5.10 d). Figure 5.11 shows a representative AFM image taken into account for analysis. The exact binding yields are listed in Table 5.4. In addition, the binding yields reported here are not necessarily proportional to the respective K_d values since the latter always require concentration-dependent measurements. Therefore, only binding yields of one protein to different ligands should be compared, and only if they were obtained at the same protein concentration.

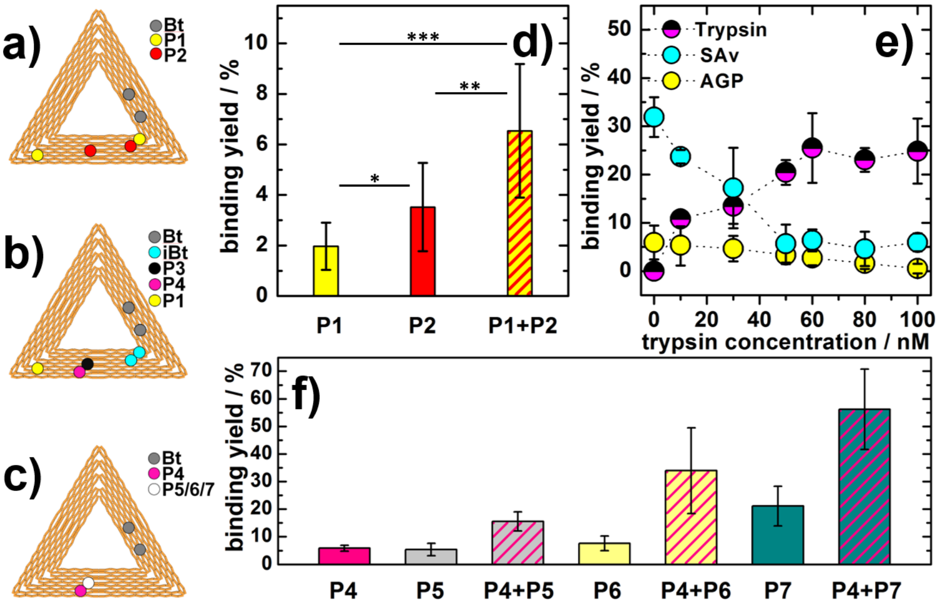

Figure 5.10: a-c) Schematics of the DNA origami substrates indicating the positions of the modified staple strands for the experiments in d) to f). d) Yields for AGP binding to P1, P2, and P1+P2. Significances were calculated using student's t-test (two-tailed distribution, heteroscedastic) and are indicated as * ($p < 0.05$), ** ($p < 0.01$), and *** ($p < 0.001$). e) Binding yields determined for three protein-pharmacophore systems in parallel as a function of trypsin concentration. f) Binding yields for mono- and bidentate trypsin binding to fragments P4 to P7. The concentrations used in these experiment were 5 nM for the nanoarrays (d, e, f), 50 nM for AGP (d, e), 60 nM (d) and 250 nM (e, f) for SAv, and 50 nM for trypsin (f). Incubation times were 30 min.

Table 5.4: Determined binding yields for monodentate and bidentate AGP binding as presented in Figure 5.10 d). $N_{(DNAorigami)}$ denotes the total number of DNA origami substrates considered.

Binder of AGP	$N_{(DNAorigami)}$	Binding yield / %
P1	1109	2.0 ± 0.9
P2	1109	3.5 ± 1.8
P1+P2	1109	6.5 ± 2.6

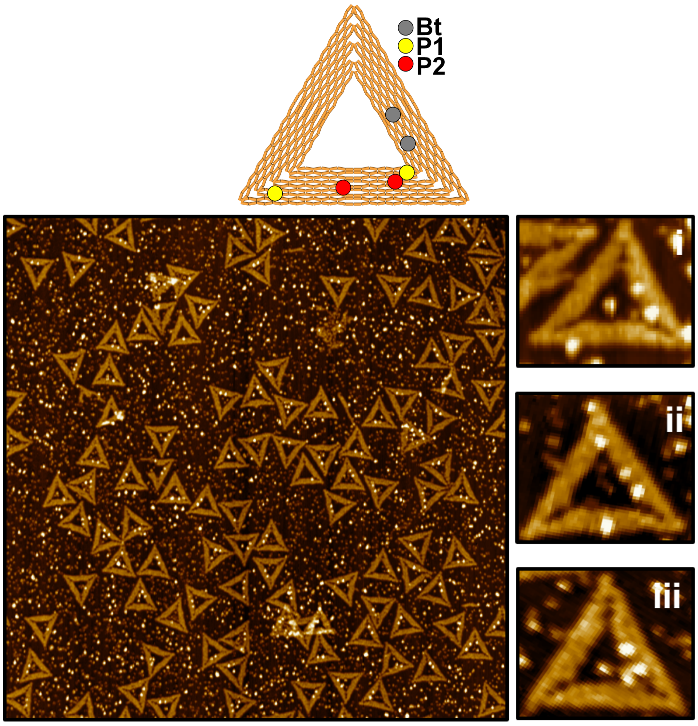

Figure 5.11: Representative AFM image of P1 and P2 nanoarrays (5 nM, see scheme) taken after incubation with 60 nM SAv and 50 nM AGP for 30 min. The image size and height scale is 1.5×1.5 μm^2 and 3.7 nm, respectively. i) – iii) show zooms of single DNA origami substrates exhibiting i) monodentate AGP binding to P1, ii) monodentate AGP binding to P2, and iii) bidentate AGP binding to P1+P2.

The next stage has been to investigate the binding of different proteins to a pharmacophore nanoarray in parallel. For this, the previously investigated proteins SAv and AGP, and the serine protease trypsin have been chosen. The latter was chosen due its ability to undergo bidentate binding to two different pharmacophores, P3 and P4 (see scheme 5.14). 4-aminobenzamidine (P4) is a weak trypsin inhibitor with an IC_{50} value of 100 μM [206]. It has been shown previously that bidentate binding of 4-aminobenzamidine in combination with 3-iodophenyl isothiocyanate (P3) can cause enhanced enzyme inhibition [206]. The pharmacophore nanoarray as shown in Figure 5.10 b) carried the weak AGP binder P1, two iBt modifications for bidentate SAv binding, and two binders P3+P4 for bidentate trypsin binding. Figure 5.12 shows representative AFM image taken into account for analysis. The determined binding yields for all three proteins are shown as a function of trypsin concentration in Figure 5.10 e) and Table 5.5.

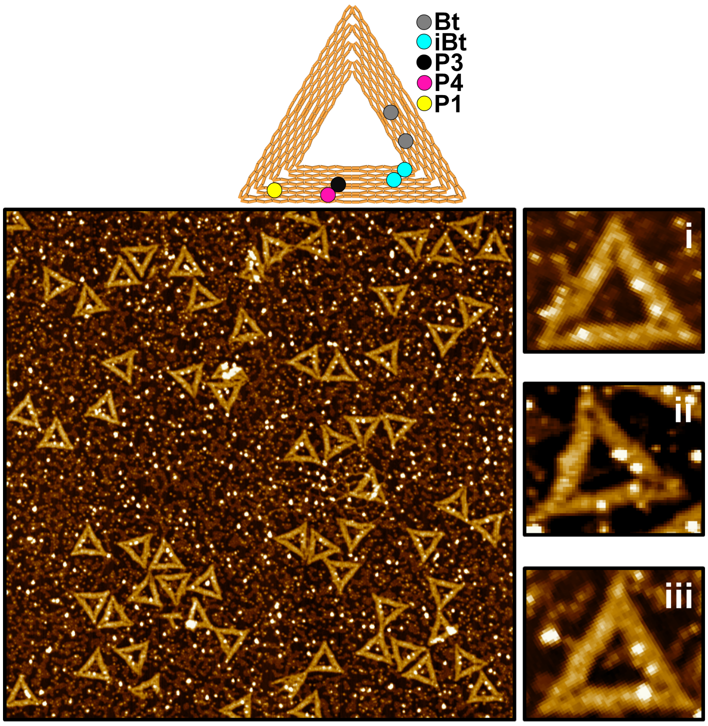

Figure 5.12: Representative AFM image of multiple pharmacophore nanoarrays (5 nM, see scheme) taken after incubation with 250 nM SAv, 50 nM AGP, and 50 nM trypsin for 30 min. The image size and height scale is 1.5×1.5 μm^2 and 3.8 nm, respectively. i) – iii) show zooms of single DNA origami substrates exhibiting i) monodentate-bound AGP, ii) bidentate-bound SAv and bidentate-bound trypsin, and iii) bidentate-bound SAv.

Table 5.5: Determined binding yields for bidentate binding of trypsin, bidentate binding of SAv and monodentate binding of AGP as presented in Figure 5.10 e). $N_{(DNAorigami)}$ denotes the total number of DNA origami substrates considered.

$c_{(trypsin)}$ / nM	$N_{(DNAorigami)}$	Binding yield of trypsin / %	Binding yield of SAv / %	Binding yield of AGP / %
0	356	0 ± 0	31.9 ± 4.1	5.9 ± 3.5
10	214	10.8 ± 1.5	23.7 ± 0.1	5.4 ± 4.2
30	224	13.5 ± 3.7	17.2 ± 8.3	4.7 ± 2.6
50	431	20.5 ± 2.6	5.7 ± 3.9	3.4 ± 1.9
60	478	25.5 ± 7.2	6.4 ± 2.3	2.8 ± 1.6
80	417	23.0 ± 2.5	4.6 ± 3.6	1.6 ± 1.2

As one would expect, the yield of trypsin binding to the P3+P4 position is monotonously increasing with trypsin concentration, until it saturates at about 50 nM. Furthermore, increasing the trypsin concentrations also results in reduced binding yields of SAv and AGP. Given that the AFM-based single-molecule detection allows us to use unmodified proteins, trypsin in its natural form can digest other proteins, thus reducing their binding to the nanoarray. Interestingly, however, the presence of trypsin has a much stronger effect on SAv binding than on AGP binding. This may be a result of the different protein concentrations which were selected to match the previous experiments (250 nM SAv vs. 50 nM AGP at 50 nM trypsin) and enable direct comparison of binding yields, or reflect substrate-specific differences in trypsin digestion. Therefore, while the parallel investigation of different protein-pharmacophore systems is possible, the presence of proteases may have drastic effects on the determined binding yields of the other proteins. In the current experiments, SAv binding to

two Bt modifications was used as a reference (Figure 5.10 b)). In future experiments with active proteases, however, the SAv-Bt reference should be replaced by other symmetry-breaking features such as dumbbell hairpins [208] or asymmetric DNA origami shapes [209].
In addition to P3, other aromatic rings can also interact with trypsin and thereby enhance the binding affinity to benzamidine in a bidentate fashion [206, 210].

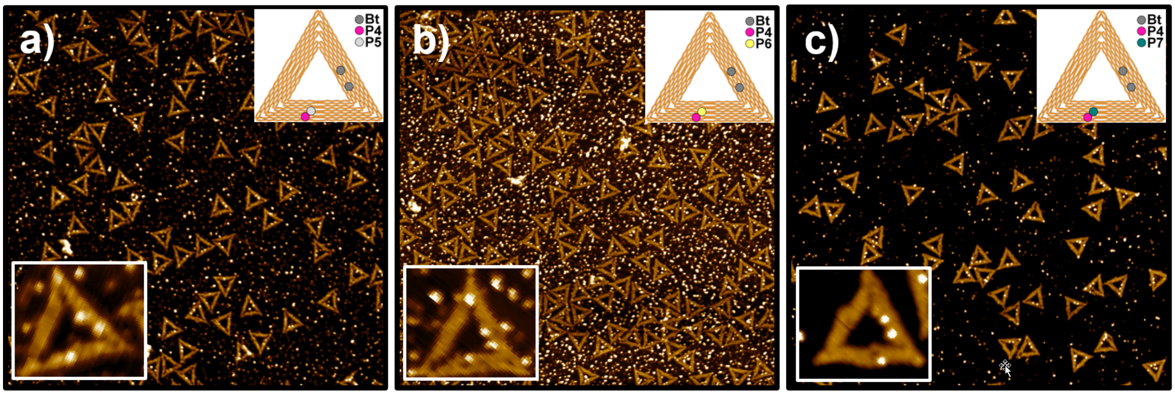

Figure 5.13: Representative AFM images of P4 + P5 a), P4 + P6 b), and P4 + P7 c) pharmacophore nanoarrays (5 nM, see schemes) taken after incubation with 250 nM SAv and 50 nM trypsin for 30 min. The image size and height scale is 2×2 μm^2 and 3.9 nm a), 4.2 nm b), and 3.8 nm c), respectively.

Therefore, in a final set of experiments, P4 was combined with three fluorescent dyes in the nanoarray to identify the best pairing fragment for P4 (Figure 5.10 c), f), and Table 5.6). Representative AFM images recorded for the different assays can are shown in Figure 5.13.

Table 5.6: Binding yield of mono- and bidentate binding of trypsin to fragments P4 to P7 as presented in Figure 5.10 f). $N_{(DNAorigami)}$ denotes the total number of DNA origami substrates considered.

Binder for trypsin	$N_{(DNAorigami)}$	Binding yield / %
P4	449	5.9 ± 1.1
P5	610	5.4 ± 2.2
P6	240	7.6 ± 2.7
P7	378	21.1 ± 7.2
P4+P5	448	15.5 ± 3.5
P4+P6	1183	34.0 ± 15.5

Pairing of cyanine 5.5 (Cy5.5) (P5) with P4 results in a two- to threefold higher trypsin binding yield compared to monodentate binding to P4 or P5 alone. In the case of fluorescein amidite (FAM) (P6), the enhancement of the binding yield due to the pairing with P4 was even stronger by a factor of about two compared to P4+P5. Monodentate trypsin binding to tetramethylrhodamine (TAMRA) (P7) already shows a binding yield considerably higher than those of the other two dyes and also P4. Remarkably, in combination with P4, the affinity to trypsin increases further, resulting in about tenfold enhancement of the binding yield compared to monodentate binding to P4 alone, and an almost threefold enhancement compared to bidentate binding to the binder pair P3+P4 (see Figure 5.10 e), f)). In order to further investigate bidentate binding of trypsin to P4+P6 and P4+P7, these pharmacophores have been conjugated either directly or with different linkers and measured the trypsin inhibition efficacy of the products (see materials and methods 5.1.4). For P4+P6, only a relatively long linker resulted in improved inhibition (IC_{50} from $\sim$ 233 μM to 86 μM). In contrast, all three conjugated P4+P7 products showed remarkably increased inhibition ($IC_{50} \sim 10$ μM), indicating that

P6 and P7 bind to different pockets of the protein. However, even the longest linker used in the inhibition assay is still considerably shorter than the distance of the pharmacophores attached to the DNA origami substrate via T_8 spacers. To further improve inhibitory efficacy, the linkers thus require further optimization, as they will not only determine the spatial arrangement of the fragments, but also interact with the protein.

5.1.3 Conclusion

These proof-of-principle experiments demonstrate the applicability of this DNA origami-based single-molecule binding assay to quantitatively study protein-pharmacophore interactions. In addition to being complementary to the current DECL technology, these pharmacophore nanoarrays could potentially achieve feature densities several orders of magnitude higher than the conventional microarray technologies (see materials and methods 5.1.4). Given that no modifications or immobilization of the target proteins are required, pharmacophore-binding in their native forms can be detected. The bidentate effect of chemical moieties can be tested combinatorically, while the spacing of fragment pairs can be fine-tuned for instance by adjusting spacer lengths, or by modifying different positions on the DNA origami [69]. DNA origami substrates thus provide a platform to display single or multiple DNA-bound ligands with nanoscale precision and represent a versatile tool for fragment-based lead discovery research.

The greatest limitation of this assay in its current form is its inability to measure binding affinities. Affinity measurements will require the determination of equilibrium binding yields at different protein concentrations [202], which is hampered by unspecific protein adsorption to the mica surface negatively affecting image quality. This challenge may be addressed in the future by performing protein binding experiments with immobilized DNA origami-based nanoarrays, which enables the passivation of the free mica surface with a protein-repelling self-assembled monolayer [125] and thereby the use of higher protein concentrations in the μM range. The use of DNA origami as substrates for the pharmacophore nanoarrays presents two additional challenges. First, different pharmacophore-labelled staple strands may be incorporated into the DNA origami with different probabilities [207], thus affecting the determined binding yields. This problem can be minimized by attaching several members of each pharmacophore species to different staples to introduce some redundancy [211]. Second, the finite surface area of the DNA origami restricts the number of pharmacophores that can be arranged and unambiguously identified in a single nanoarray. This limitation may be overcome by using single-stranded tile assemblies instead, which may enable the construction of larger pharmacophore nanoarrays displaying hundreds of different fragments [212]. Alternatively, several distinguishable DNA origami shapes carrying different pharmacophore nanoarrays can be combined in a single assay. Complex DNA origami shapes can be quickly designed using fully automated software [98], while assembly and purification have become routine procedures. Recently, biotechnological mass production of DNA origami was demonstrated, which will drastically reduce costs [75]. Therefore, the bottlenecks in the presented assay are the recording of high quality AFM images and their manual analysis. However, recent developments in high-speed and even video-rate AFM imaging [53] as well as new and automated image analysis methods [213] show great potential for driving this approach toward the realization of high throughput drug screening at the single-molecule level.

5.1.4 Material and Methods

5.1.4.1 DNA origami assembly

Triangular DNA origami [23] have been assembled from 208 staple strands (Metabion) and the M13mp18 scaffold (Tilibit) as previously described [89] in 1 x TAE (Calbiochem) containing 10 mM $MgCl_2$ (Sigma-Aldrich). Modified staples were added in 10-fold excess over the unmodified ones, so that statistically 91% of each modification site will carry the desired modification. Hybridization was carried out in a Thermocycler Primus 25 advanced (PEQLAB) by heating to 80°C and subsequent cooling to room temperature over a time of 90 min. The samples were then purified with 1 x TAE/$MgCl_2$ buffer by spin filtering using ultra-0.5 ml Centrifugal Filters with 100 kDa MWCO (Amicon). The DNA origami concentration was measured using an IMPLEN nanophotometer and adjusted to 30 nM with 1 x TAE/$MgCl_2$.

5.1.4.2 Pharmacophore modifications

Staples modified with Bt, Cy5.5 (P5), FAM (P6), and TAMRA (P7) (scheme 5.15 and Table 5.7) were purchased from Metabion. Amino-modified DNA holders were obtained from IBA either attached to CPG (Controlled Pore Glass) solid supports or HPLC (High-performance liquid chromatography) purified.

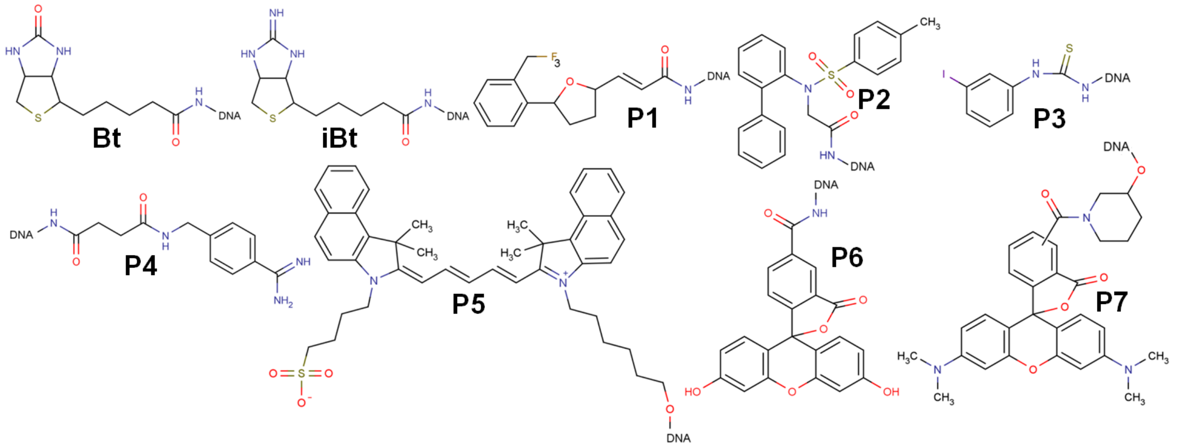

Figure 5.14: Structures of the pharmacophore modifications used in this study. **Bt**–biotin, **iBt**–iminobiotin, **P1**–(2E)-3-5-[2-(fluoromethyl)phenyl]oxolan-2-ylprop-2-enamide, **P2**–2-[N-(2-phenylphenyl)4-methylbenzen-sulfonamido]-acetamide, **P3**–3-iodophenyl isothiocyanate, **P4**–4-aminobenzamidine (with succinic anhydride at DNA), **P5**–Cy5.5, **P6**–6-carboxyfluorescein (6-FAM), **P7**–TAMRA.

Details on the synthetization of the modifications P1 through P7 may be found in the supplementary material of [138].

Table 5.7: Sequences of all pharmacophore-modified staples, using Rothemund's original notation. Thymine spacers are indicated in bold face.

Modified staples		Oligonucleotide sequences 5' → 3'
iBt (T_8)	t-7s8g	**iBt-TTTTTTTT**GCGCCTGTTATTCTAAGAACGCGATTCCAGAGCCTAATTT
iBt (T_8)	t5s4e	**iBt-TTTTTTTT**CCTTGAGTCAGACGATTGGCCTTGCGCCACCC
iBt (T_8)	t4s1g	TAGCCCGGAATAGGTGAATGCCCCCTGCCTATGGTCAGTG**TTTTTTTT-iBt**
Bt (T_8)	t-1s8g	**Bt-TTTTTTTT**TTTCCTTAGCACTCATCGAGAACAATAGCAGCCTTTACAG
Bt (T_0)	t-3s14e	**Bt-**GTTTTGTCAGGAATTGCGAATAATCCGACAAT
Bt (T_0)	t1s14i	**Bt-**GTGAGAAAATGTGTAGGTAAAGATACAACTTT
iBt (T_4)	t5s4e	**iBt-TTTT**CCTTGAGTCAGACGATTGGCCTTGCGCCACCC
iBt (T_4)	t4s1g	TAGCCCGGAATAGGTGAATGCCCCCTGCCTATGGTCAGTG**TTTT-iBt**
iBt (T_0)	t-7s8g	**iBt-**GCGCCTGTTATTCTAAGAACGCGATTCCAGAGCCTAATTT
iBt (T_0)	t-8s5f	TTCTGACCTAAAATATAAAGTACCGACTGCAGAAC**-iBt**
P1 (T_8)	t-8s5f	TTCTGACCTAAAATATAAAGTACCGACTGCAGAAC**TTTTTTTT-P1**
P1 (T_8)	t4s1g	TAGCCCGGAATAGGTGAATGCCCCCTGCCTATGGTCAGTG**TTTTTTTT-P1**
P2 (T_8)	t-1s8g	**P2-TTTTTTTT**TTTCCTTAGCACTCATCGAGAACAATAGCAGCCTTTACAG
P2 (T_8)	t5s4e	**P2-TTTTTTTT**CCTTGAGTCAGACGATTGGCCTTGCGGCCACCC
P3 (T_8)	t-1s6e	TTAGTATCGCCAACGCTCAACAGTCGGCTGTC**TTTTTTTT-P3**
P4 (T_8)	t-1s8g	**P4-TTTTTTTT**TTTCCTTAGCACTCATCGAGAACAATAGCAGCCTTTACAG
P5 (T_8)	t-1s6e	TTAGTATCGCCAACGCTCAACAGTCGGCTGTC**TTTTTTTT-P5**
P6 (T_8)	t-1s6e	TTAGTATCGCCAACGCTCAACAGTCGGCTGTC**TTTTTTTT-P6**
P7 (T_8)	t-1s6e	TTAGTATCGCCAACGCTCAACAGTCGGCTGTC**TTTTTTTT-P7**

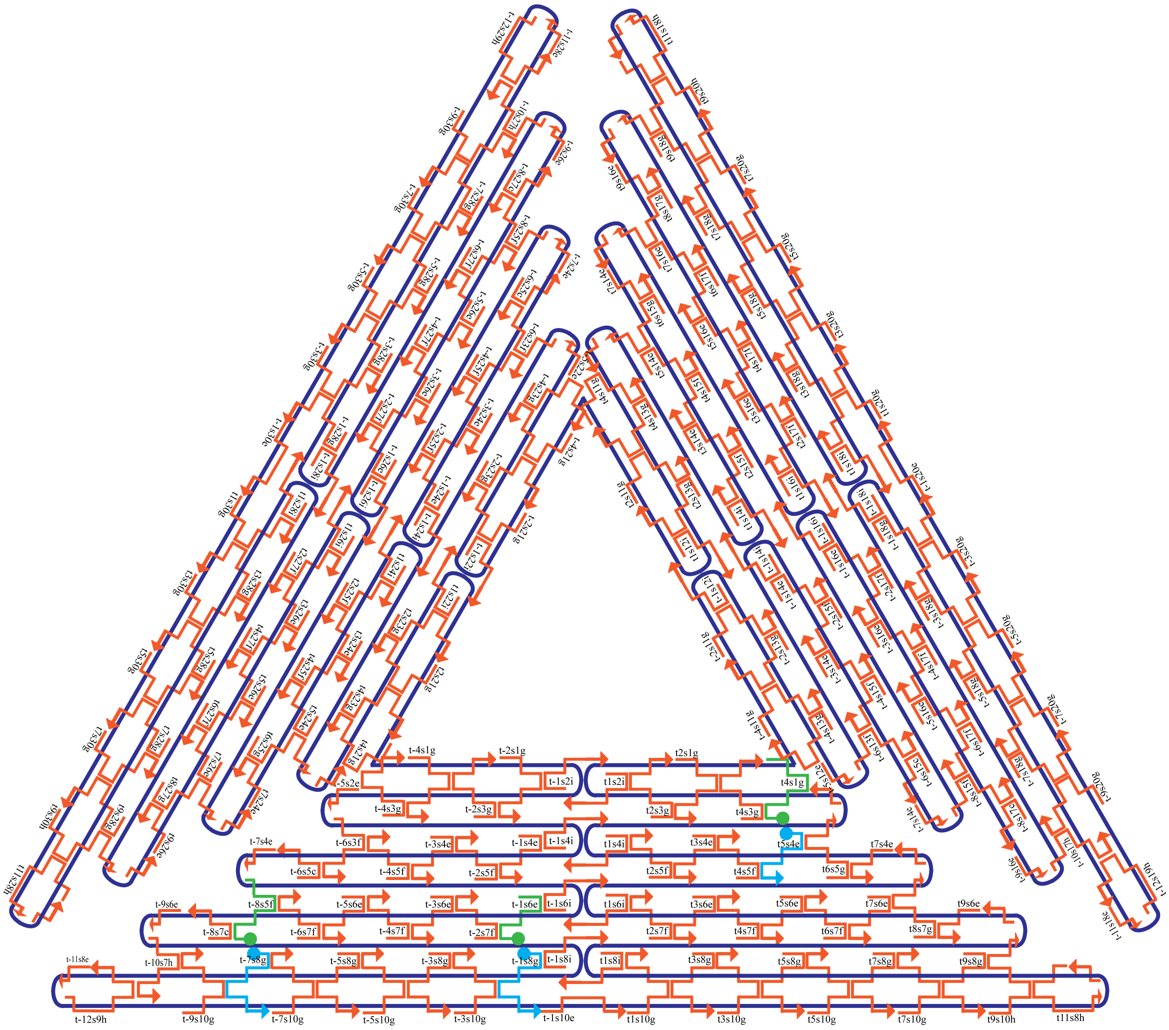
t-4s1g
t-2s1g
t2s1g
t-5s2e
t-1s2i
t1s2i
t4s1g
t-4s3g
t-2s3g
t2s3g
t4s3g
t-7s4e
t-6s3f
t-3s4e
t-1s4e
t-1s4i
t1s4i
t3s4e
t5s4e
t7s4e
t-6s5c
t-4s5f
t-2s5f
t2s5f
t4s5f
t6s5g
t-9s6e
t-8s5f
t-5s6e
t-3s6e
t-1s6e
t-1s6i
t1s6i
t3s6e
t5s6e
t7s6e
t9s6e
t-8s7c
t-6s7f
t-4s7f
t-2s7f
t2s7f
t4s7f
t6s7f
t8s7g
t-11s8c
t-10s7h
t-7s8g
t-5s8g
t-3s8g
t-1s8g
t-1s8i
t1s8i
t3s8g
t5s8g
t7s8g
t9s8g
t-12s9h
t-9s10g
t-7s10g
t-5s10g
t-3s10g
t-1s10e
t1s10g
t3s10g
t5s10g
t7s10g
t9s10h
t11s8h

Figure 5.15: Scaffold path and staple arrangement of the triangular DNA origami. Pharmacophore-modified staples are highlighted (green – 3’ modifications, cyan – 5’ modifications), with the dots indicating the positions of the attached modifications.

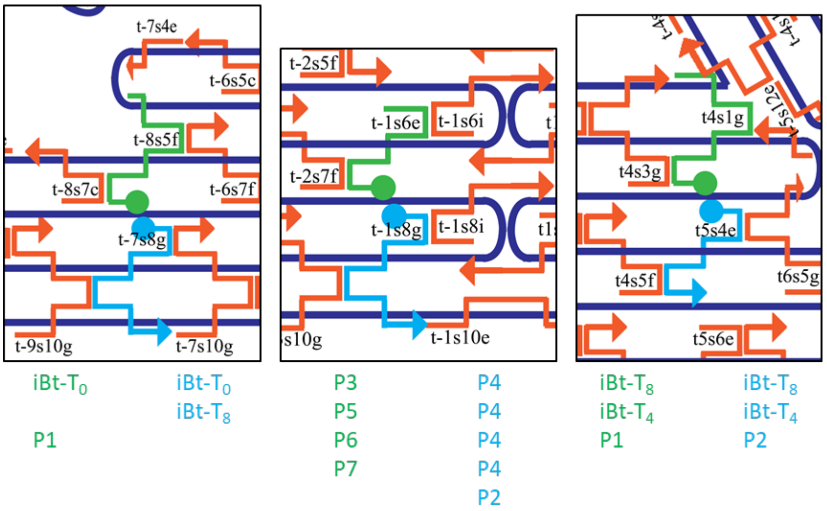
t-7s4e
t-6s5c
t-8s5f
t-8s7c
t-6s7f
t-7s8g
t-9s10g
t-7s10g
t-2s5f
t-1s6e
t-1s6i
t-2s7f
t-1s8g
t-1s8i
s10g
t-1s10e
t4s1g
t4s3g
t5s4e
t4s5f
t6s5g
t5s6e
iBt-T_0
iBt-T_0
iBt-T_8
P1
P3
P5
P6
P7
P4
P4
P4
P4
P2
iBt-T_8
iBt-T_4
P1
iBt-T_8
iBt-T_4
P2

Figure 5.16: Zooms of the individual pharmacophore-modified staples (green – 3’ modifications, cyan – 5’ modifications) from Figure 5.15 and the attached fragments and fragment pairs.

5.1.4.3 Protein binding experiments

SAv (Sigma-Aldrich) and α-1-acid glycoprotein (AGP from human plasma, Sigma-Aldrich) both were dissolved in HPLC-grade water (VWR) to yield a concentration of 123 μM. Trypsin (type I from bovine pancreas, Sigma-Aldrich) was dissolved in 0.1 M HCl (Stockmeier Chemie) to yield a concentration of 125 μM. Stock solutions were diluted to the desired concentrations using 1 x TAE/$MgCl_2$ with the pH adjusted to 7.5 with 0.1 M HCl (Stockmeier Chemie). The protein samples were then incubated at the final concentrations with 5 nM DNA origami nanostructures at room temperature for 10 to 120 min.

5.1.4.4 AFM imaging

After incubation, 10 μl of the protein-DNA origami samples were incubated on freshly cleaved mica surfaces for 1 min. Subsequently, the mica sample was vertically dipped into HPLC-grade water (VWR) for 10 seconds and blow-dried in a stream of ultrapure air. AFM measurements were carried out in air using a JPK Nanowizard II, an Agilent 5100, and Agilent 5500 AFM, respectively, operated in intermittent contact mode and silicon cantilevers (NSC18/AlBS and NSC18/NoAl) from MikroMasch. Images were recorded with scan sizes ranging from 2×2 μm^2 to 3×3 μm^2 with a resolution of 1024 px×1024 px. AFM imaging under dry instead of liquid conditions was employed for two reasons. First, the single-stranded spacers carrying the individual pharmacophores are comparatively long and can be moved around by the AFM tip during imaging in liquid, resulting in a reduced resolution when determining the position of a bound protein. Second, and more importantly, the samples were dried in order to quench the protein binding reaction in equilibrium and avoid any post-immobilization binding or dissociation due to changes in protein or DNA origami concentration.

5.2 Quantitative assessment of tip effects in single-molecule High-Speed AFM

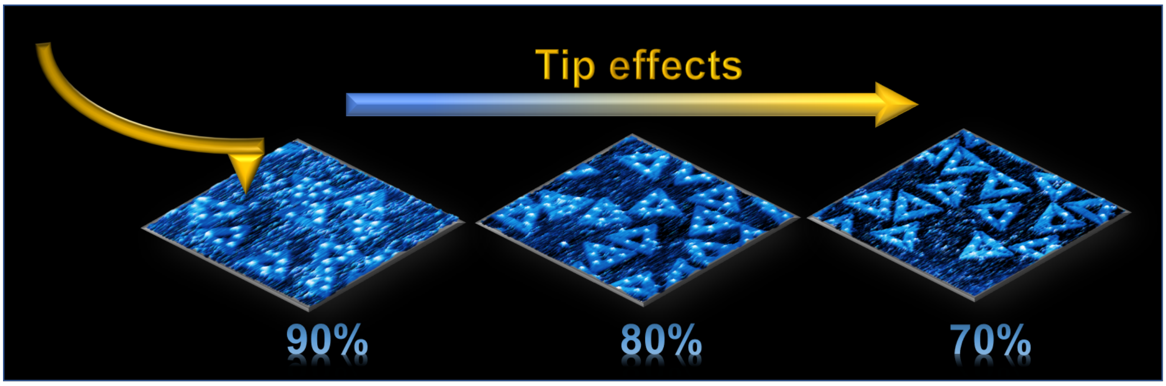

5.2.1 Introduction

For the drug discovery assays presented in section 5.1, a relatively large number of DNA origami have to be counted to get meaningful statistics. To achieve this, in general, several AFM images have to be recorded. Considering the used image sizes and resolutions, acquisition of a single image takes roughly 17 minutes at a line rate of 1 Hz. However, high-throughput screening is highly desirable to speed up the data acquisition and evaluation. A promising measurement technique to improve the sample throughput is HS-AFM.

HS-AFM has become a powerful tool for studying the dynamics of biomolecular processes at the single-molecule level [136, 214]. HS-AFM, with its temporal resolution of less than 1 second per image, enables the real-time visualization of numerous biological phenomena such as the motion of molecular motors [215], the self-assembly of protein complexes [216], membrane-transforming proteins [217–219] and the activity of enzymes such as cas9 [220], proteasomes [221], nucleases [178], and protein disulfide isomerase [222] as well as the dynamics of bacterial microcompartments [223], and the visualization of membrane protein-embedded nanodiscs [224] and DNA origami lattice formation [120].

The tip effects on systems under investigation that are characterized by relatively strong interactions with dissociation constants (K_d) in the nM range, such as actin-myosin complexes with a K_d of 0.5–10 nM [216], are generally considered to be of lesser importance [225]. Weaker interactions can, however, be significantly disturbed by the forces exerted on the sample during scanning. Thus, systems with high dissociation constants such as homodimers of SAS-6 with a K_d of 60 μM suffer from strong tip effects and require a gentle measurement setting [216]. However, also for strongly bound systems it cannot be ruled out that the rapidly scanning tip has a disturbing influence. For strongly binding systems, the quantification of the tip effects is more difficult because the tip effects are not that strong. In the literature, it is proposed to carefully investigate the protein-protein or DNA-protein binding depending on the HS-AFM scan parameters since the scanning AFM tip exerts forces onto the sample which may cause artificial dissociation events and falsify the desired results [225]. However, a system that allows the effects of the tip to be quantitatively determined for an existing installation has not yet been demonstrated.

To quantitatively investigate the role of tip effects during HS-AFM measurement, one of the strongest known noncovalently binding biomolecular systems, SAv-Bt with a dissociation constant in the fM range [226], is used for visualization using a DNA origami-based single-molecule assay [184]. DNA origami substrates are excellently suited for this, since molecular-defined arrangements that are easy to track under the AFM can be created relatively easy. In the given experiment, Bt modifications are arranged on the DNA origami substrate such that a mono- and bidentate bond to SAv can be achieved. The influence of line rate and amplitude setpoint are investigated by means of steady state binding yields determined from the AFM recordings.

5.2.2 Results and Discussion

Here the DNA origami are used to quantify the effect of the AFM tip on the system under investigation. The DNA origami are functionalized with Bt and bind with SAv. As can be seen in Figure 5.17, the occupation of Bt-modified positions on the DNA origami substrate with SAv was examined over a longer period of time to see whether there is any influence on this strongly binding system. From literature a stable binding should have been observable [59, 182, 226–228], however, if a mono- and bidentate position is tracked on a single DNA origami over a period of 20 minutes at a line rate of 15 Hz, the occupancy of the mono- and bidentate positions fluctuates as can be seen in Figure 5.17 b). For the bidentate binding of SAv to Bt, fluctuations can be observed throughout the experiment. For the monodentate binding, however, occupation drops to zero after about 600 s and remains at this value until the end of the measurement. These fluctuations show that SAv tends to dissociate from the Bt ligands, which, however, can then be occupied by another free SAv from solution. Since the bidentate Bt-position allows a higher binding probability with at least one to two of the four pockets of the SAv, a position on the DNA origami with two Bt-modifications should have a very low K_d (for monodentate binding K_d is on the order of 10^{-14} M [229]). Thus the affinity for the SAv to bind at a bidentate position is much higher than for a monodentate position.

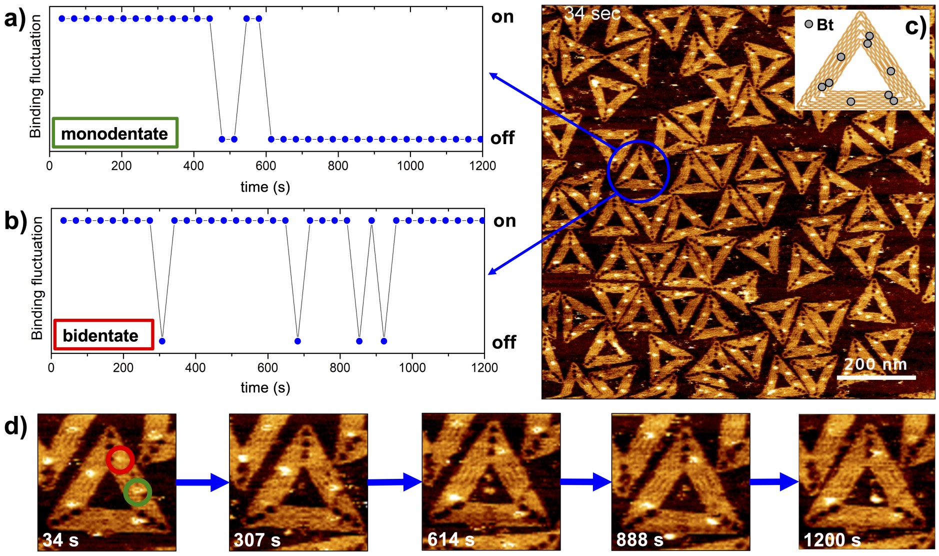

Figure 5.17: Occupation of Bt modified positions over a time of 20 minutes for both mono- and bidentate binding to SAv. a) Monodentate (green) and b) bidentate (red) Bt-position on a single DNA origami (marked blue) from the AFM image in c). The image covers an area of 1×1 μm^2 at a resolution of 512 px×512 px and was recorded at a line rate of 15 Hz. The inset shows a schematic of the Bt modifications on the DNA origami. d) Zoom of the tracked DNA origami with the selected binding of SAv at the monodentate (green) and bidentate (red) Bt position at selected times between 34 s and 1200 s.

Figure 5.18 clearly shows that after 600 seconds the number of occupied positions for monodentate binding on the measured sample area have strongly decreased such that after 1200 s many monodentate positions are unoccupied.

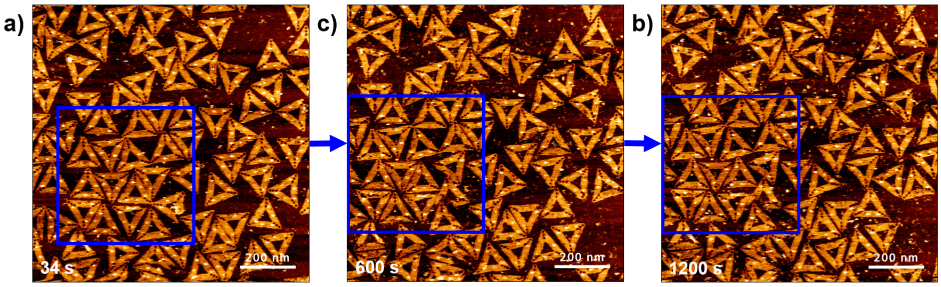

Figure 5.18: Selected images taken from a 20 minute HS-AFM video. Individual pictures were taken at 34 s a), 600 s b), and 1200 s c) respectively. The total scan area was 1×1 μm^2 with a line rate of 15 Hz. The blue frame indicates the area containing the DNA origami tracked for the statistics.

The AFM pictures presented so far were recorded using a dynamic imaging mode. Within this mode the device dynamically adjusts its scanning parameters for optimal image quality. In this mode, however, it is quite hard to get a reasonable estimate of the tip effects. For further investigations, a static imaging mode, i.e. image acquisition with a fixed set of parameters has been used. To quantify the tip effects HS-AFM videos using amplitude setpoints between 70% and 90% and line rates ranging from 10 Hz to 70 Hz have been recorded. The total size of the scanned area was chosen as $1\times1\mu$m^2 at a resolution of 512×512 pixels with a constant free amplitude of 3.3 nm.

Figures 5.20–5.22 show the time resolved binding yields for mono- and bidentate SAv-Bt binding at amplitude setpoints of 70%, 80%, and 90%, respectively, for different line rates. An almost universal qualitative finding for all three considered amplitude setpoints is a changing image quality with increasing line rate as can be seen in the representative AFM images in the left most panels in Figures 5.20–5.22. In case of the 70% amplitude setpoint, the observed steady state binding yield for the monodentate SAv-Bt binding drops from 100% at a line rate of 10 Hz to roughly 40% at a line rate of 70 Hz. Simultaneously a significant decrease in image quality is observable. A similar, but not as drastic, decrease is observed for the steady state binding yield of the bidentate SAv-Bt binding which drops down to about 70% at a line rate of 40 Hz and rises back to about 90% at a line rate of 70 Hz. A possible explanation for the decrease image quality is that the AFM tip is picking up SAv from the sample surface and from the solution. At least the streaks in the AFM image clearly indicate a contamination of the AFM tip [230]. Due to the rapid scanning, the tip may collect a lot of SAv before it is stripped off at the sample surface.

From a qualitative point of view, one finds the inverse situation at an amplitude setpoint of 90%. Here, the image quality actually increases with increasing line rate. A possible explanation is that, on average, the distance between the AFM tip and the sample surface is larger, such that the measurement is less sensitive for SAv diffusion at the sample surface. The falling trend for the steady state binding yield is, however, also present for this amplitude setpoint. For monodentate SAv-Bt binding one finds a final steady state binding yield of 64% and for the bidentate binding one of 74% at 70 Hz.

The images for the amplitude setpoint of 80% lie somewhere in between. For this setpoint a more or less constant image quality can be observed which is visible in AFM pictures in Figure 5.21 and 5.23. The binding yields presented in the top panel of Figure 5.23 have been determined by averaging over the mono- and bidentate binding sites of all five tracked DNA origami for a single AFM image taking the standard error of the mean as an error measure. The final steady state binding yields at 70 Hz are given by roughly 33% and 71% for mono- and bidentate binding, respectively. Figure 5.24 exemplarily shows AFM images and the time resolved binding yields for mono- and bidentate binding at selected times for all considered amplitude setpoints recorded at a line rate of 50 Hz. This line rate has been chosen since for the monodentate binding the observed steady state binding yield exhibits a sudden drop of about 50% indicating strong tip effects at this particular line rate at a setpoint of 70%.

From the quantitative point of view, the results for all amplitude setpoints are consistent. At each considered setpoint a clear decrease of the steady state binding yield with increasing line rate is observable.

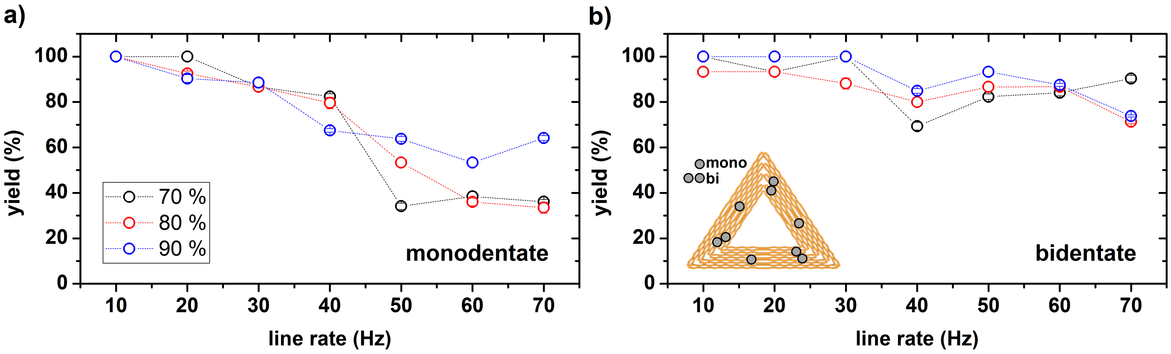

Figure 5.19: Determined steady state binding yields for mono- and bidentate SAv-Bt binding depending on the line rate and amplitude setpoint.

Table 5.8: Stationary binding yield determined from the last 100 s of 500 to 600 s by linear regression for a constant function of the mono- and bidentate positions on the DNA origami at 70, 80, and 90% setpoint and 10–70 Hz line rate.

	monodentate			**bidentate**		
	70%	80%	90%	70%	80%	90%
10 Hz	100.0±0.0	100.0±0.0	100.0±0.0	100.0±0.0	93.3±0.0	100.0±0.0
20 Hz	100.0±0.0	92.5±1.1	90.4±1.7	93.3±0.0	93.3±0.0	100.0±0.0
30 Hz	86.7±0.0	86.7±0.0	88.5±2.0	100.0±0.0	88.2±2.4	100.0±0.0
40 Hz	82.4±1.3	79.6±2.5	67.5±0.8	69.4±1.7	80.0±0.0	84.9±1.0
50 Hz	34.1±1.4	53.3±0.0	63.8±1.0	82.4±1.2	86.7±0.0	93.3±0.0
60 Hz	38.4±2.2	35.9±1.7	53.3±0.0	84.1±1.4	86.7±1.8	87.6±0.6
70 Hz	36.1±1.0	33.5±2.4	64.2±1.1	90.4±1.4	71.3±0.8	73.9±0.5

An overview over the determined steady state binding yields depending on the set point and the line rate is given in Figure 5.19 and Table 5.8. For both, monodentate and bidentate SAv-Bt binding, a decrease of the steady state binding yield can be observed for increasing line rates. A possible explanation for the observed decrease of the steady state binding yield is that on the one hand, the AFM tip is acting in an abrasive manner and rips off SAv that is already bound on the DNA origami. On the other hand, the rapidly scanning tip is probably also inhibiting a rebinding. In literature, the lateral forces due to the finite speed of the feedback loop occurring during HS-AFM have been suggested as the disturbing factor for protein-protein interactions resulting in a decreased self-assembly rate of SAS-6 rings by Nievergelt *et al.* [216]. However, a direct transfer of their results to the experiment presented here is not possible, since another measurement mode is used. Nevertheless, increased lateral forces at sudden changes of the sample topography, such as a protein bound to a DNA origami, may not be ruled out completely for HS-AFM measurements in intermittent contact mode as well. On basis of the obtained data it remains unclear whether the abrasive behavior of the AFM tip is caused be lateral or vertical forces exerted onto the samples.

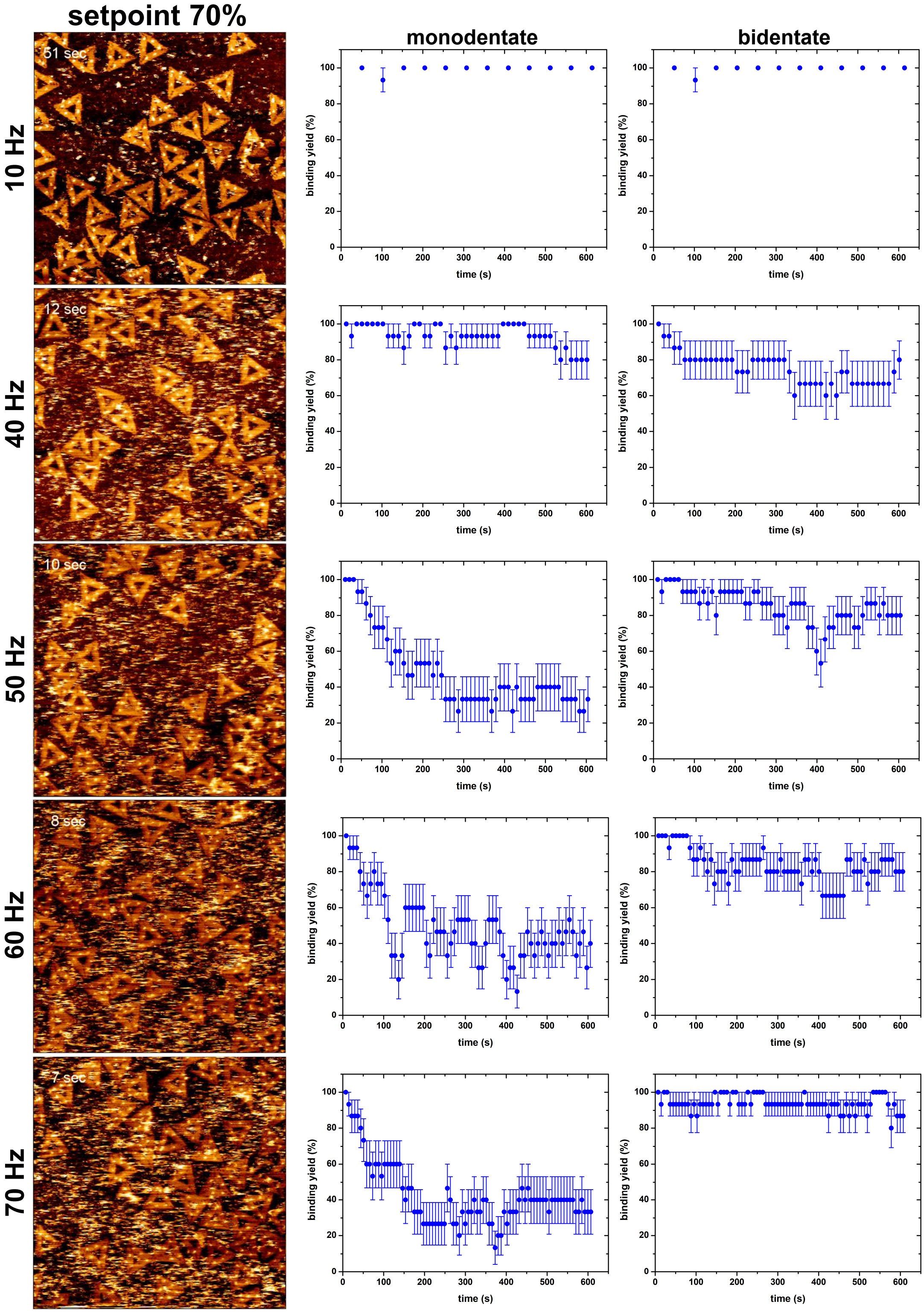

Figure 5.20: Steady state binding yields obtained at different line rates using a setpoint of 70%. On the left site is the first AFM image of the scanned sample area with a setpoint of 70% and selected line rates of 10, 40, 50, 60, 70 Hz and the associated statistics of the mono and bidentate binding yields over the entire measurement time of 10 min. The AFM images have a size of 1×1 μm^2 with a resolution of 512×512 pixel and a free amplitude of 3.3 nm.

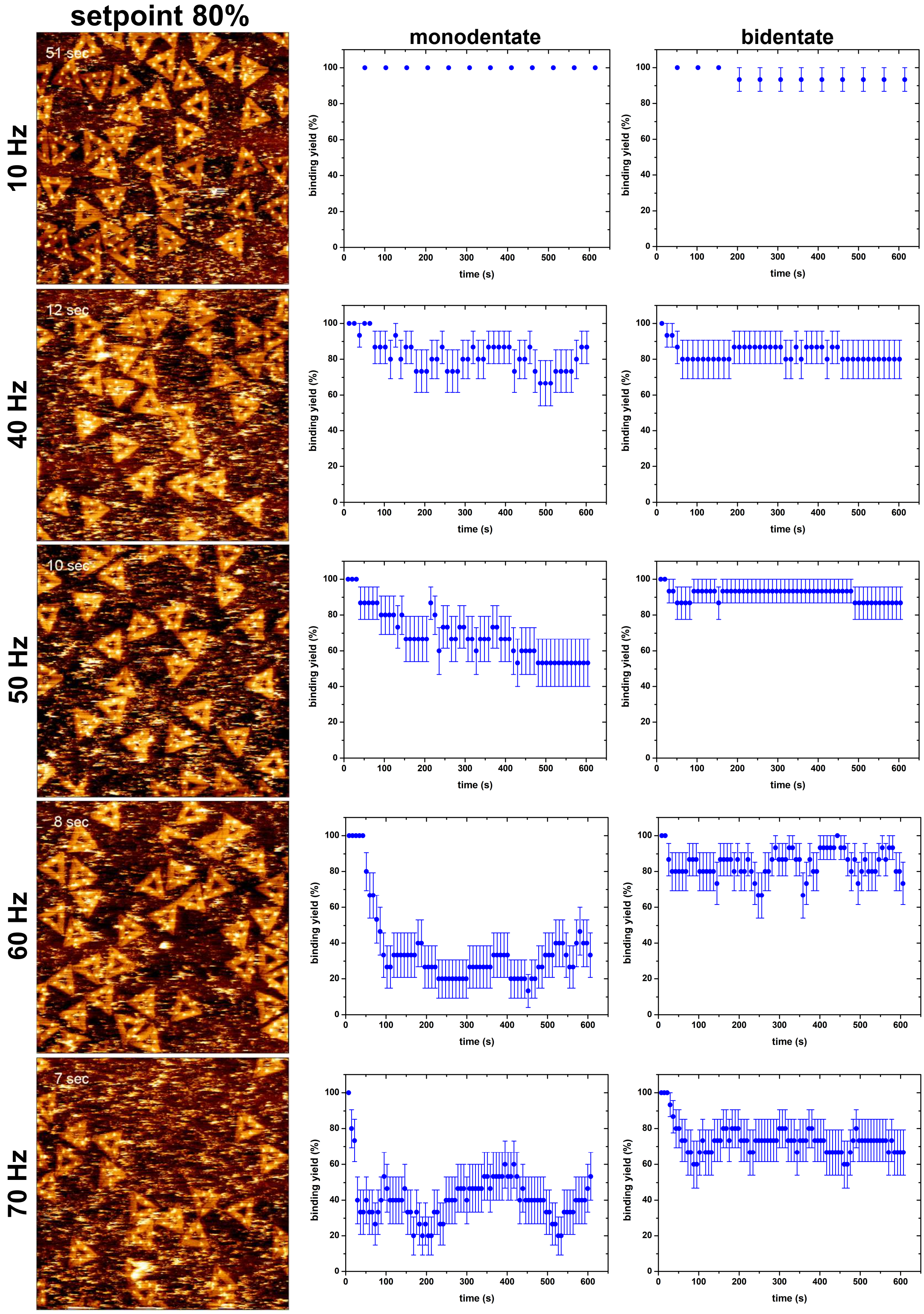

Figure 5.21: Steady state binding yields obtained at different line rates using a setpoint of 80%. On the left site is the first AFM image of the scanned sample area with a setpoint of 80% and selected line rates of 10, 40, 50, 60, 70 Hz and the associated statistics of the mono and bidentate binding yields over the entire measurement time of 10 min. The AFM images have a size of 1×1 μm^2 with a resolution of 512×512 pixel and a free amplitude of 3.3 nm.

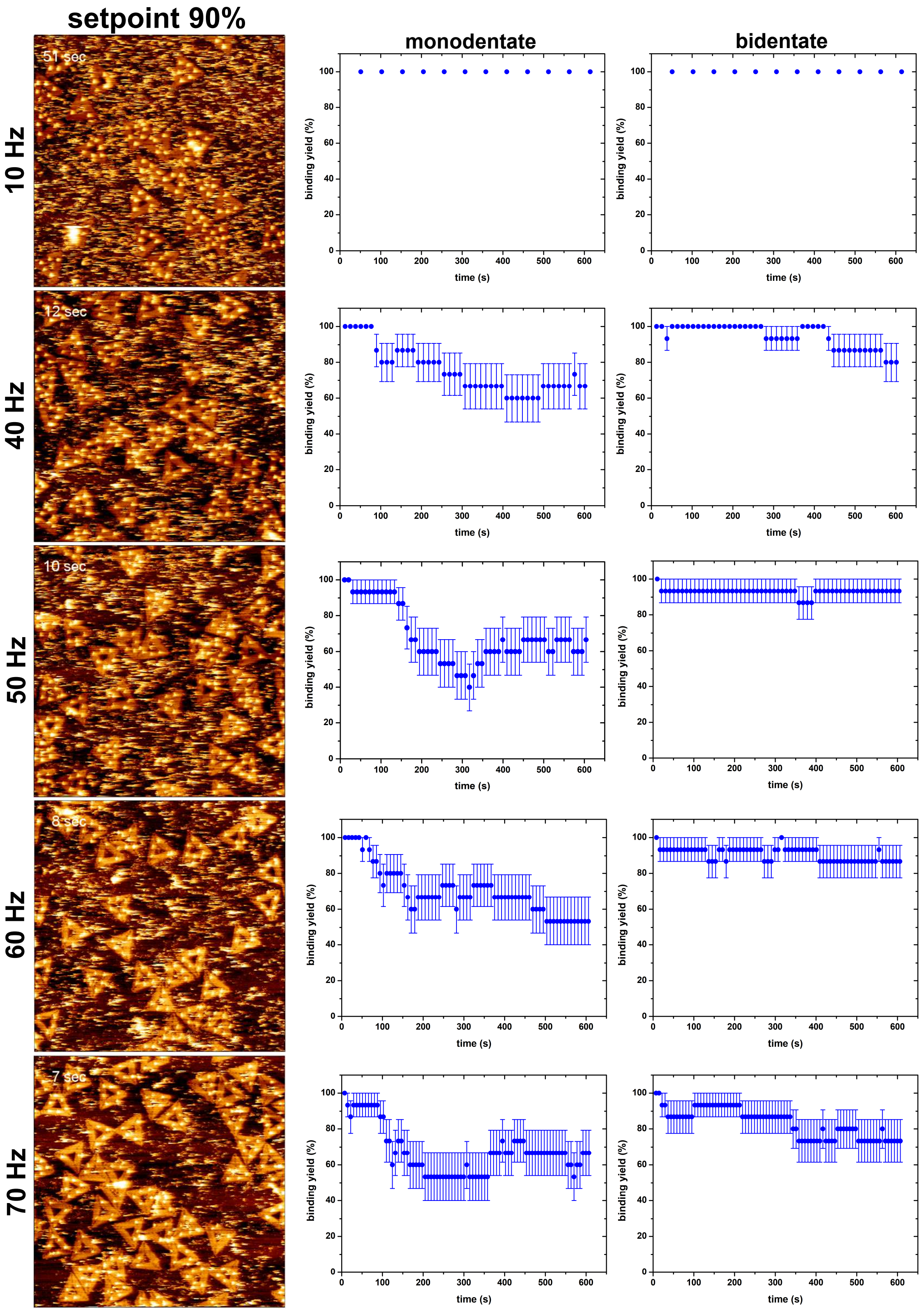

Figure 5.22: Steady state binding yields obtained at different line rates using a setpoint of 90%. On the left site is the first AFM image of the scanned sample area with a setpoint of 90% and selected line rates of 10, 40, 50, 60, 70 Hz and the associated statistics of the mono and bidentate binding yields over the entire measurement time of 10 min. The AFM images have a size of 1×1 μm^2 with a resolution of 512×512 pixel and a free amplitude of 3.3 nm.

Considering the set point, a clear trend is observable neither for the monodentate binding nor for the bidentate binding. This result is, at least to some extend, surprising. In general higher set points are advised for sensitive samples since the forces exerted onto the sample are smaller. Therefore a decreasing steady state binding yield with decreasing set point could have been expected.

	Binding yield after run time of 51 s		Binding yield after run time of 307 s		Binding yield after run time of ~ 600 s	
Hz	monodentate	bidentate	monodentate	bidentate	monodentate	bidentate
10	100.0 ± 0.0 %		100.0 ± 0.0 %	93.3 ± 6.7 %	100.0 ± 0.0 %	93.3 ± 6.7 %
40	100.0 ± 0.0 %	86.7 ± 9.1 %	80.0 ± 10.7 %	86.7 ± 9.1 %	86.7 ± 9.1 %	80.0 ± 10.7 %
70	40.0 ± 13.1 %	80.0 ± 10.7 %	46.7 ± 13.3 %	80 ± 10.7 %	53.3 ± 13.3 %	66.7 ± 12.6 %

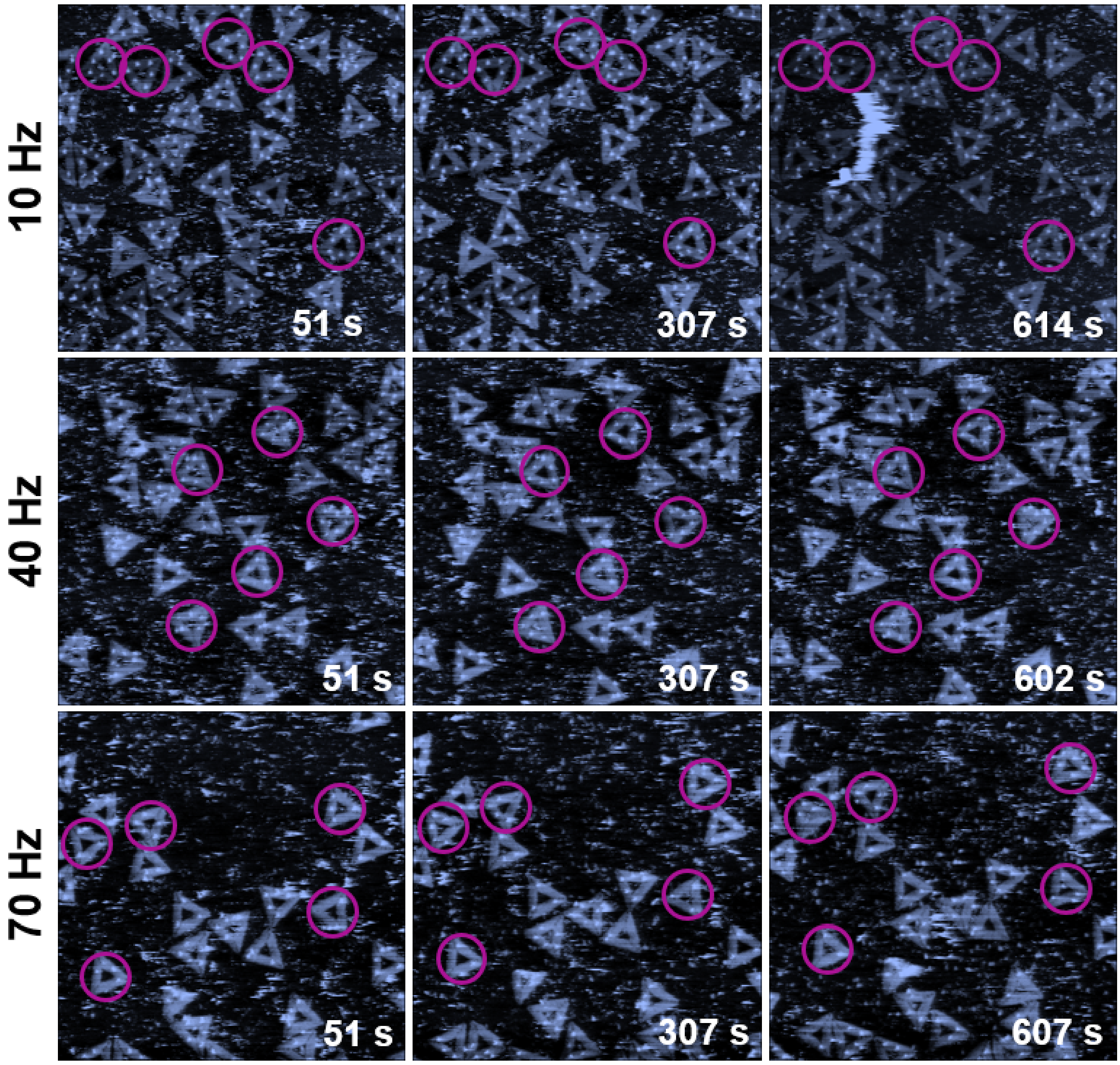

Figure 5.23: Selected AFM images recorded at a setpoint of 80% and different line rates. Here some selected HS-AFM images recorded at line rates of 10, 40, and 70 Hz are shown. Five DNA origami are marked in pink, which were observed and evaluated for the statistics of this work over the time of 10 minutes. The statistics of the selected DNA origami are also shown in tabular form for the respective mono- and bidentate binding. Binding yields presented in the top panel have been determined from a single image.

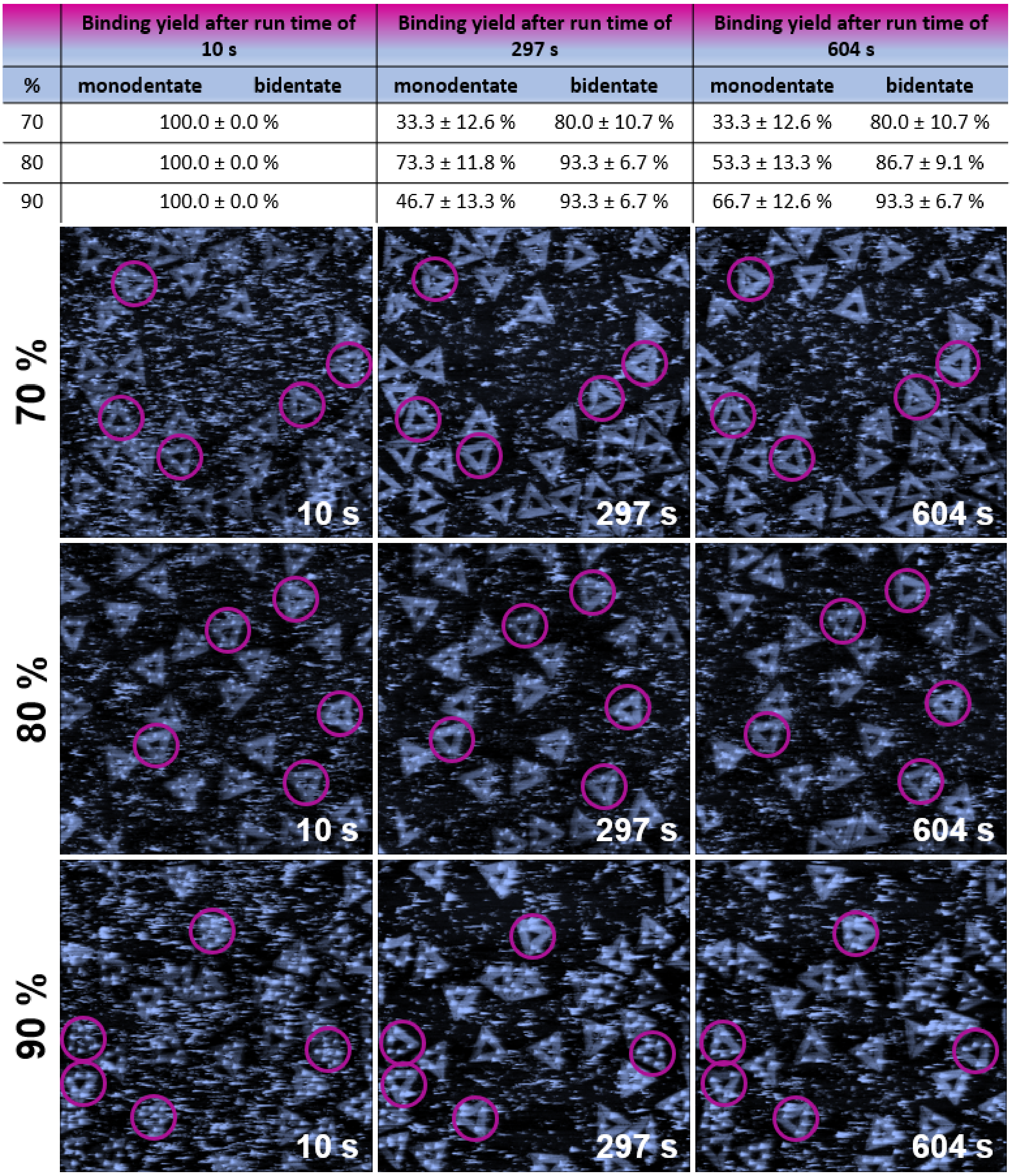

	Binding yield after run time of 10 s		Binding yield after run time of 297 s		Binding yield after run time of 604 s	
%	monodentate	bidentate	monodentate	bidentate	monodentate	bidentate
70	100.0 ± 0.0 %		33.3 ± 12.6 %	80.0 ± 10.7 %	33.3 ± 12.6 %	80.0 ± 10.7 %
80	100.0 ± 0.0 %		73.3 ± 11.8 %	93.3 ± 6.7 %	53.3 ± 13.3 %	86.7 ± 9.1 %
90	100.0 ± 0.0 %		46.7 ± 13.3 %	93.3 ± 6.7 %	66.7 ± 12.6 %	93.3 ± 6.7 %

Figure 5.24: Selected AFM images taken from an HS-AFM video recorded at 50 Hz line rate and setpoints of 70%, 80%, and 90%. The tracked DNA origami are marked in pink. Binding yields presented in the top panel have been determined from a single image.

5.2.3 Conclusion and outlook

It has been successfully demonstrated that a DNA origami single-molecule binding assay may be used as a platform to quantify the effects of the rapidly scanning tip during HS-AFM measurements. In literature it has been argued that the rapid scanning affects the system under investigation. However, for strongly bound systems such as SAv-Bt it has been argued, that the tip effects are of minor importance and do not disturb the system significantly.

In the presented results, the influence of the rapidly scanning tip is two-fold. On the purely qualitative side, a significant change in image quality with increasing line rate is visible for amplitude setpoints of 70% and 90%, whereas on the quantitative side it has been shown, that the tip effects are sizeable, in case of the monodentate binding even drastic, even for the SAv-Bt system which belongs to the strongest known non-covalently binding systems. The obtained data clearly show that the studied system is driven away from equilibrium into a steady state which depends on both, the amplitude setpoint and the selected scan rate. The influence of an increasing line rate is, however, more prominent and a clear trend towards decreased steady state binding yields with increasing line rate is visible. Regarding the chosen amplitude setpoint, no clear trend is visible in the obtained results. From a practical point of view, higher amplitude setpoints should be less invasive since the dynamic forces exerted onto the sample are smaller. In future experiments it could be further investigated whether the abrasive behavior of the AFM tip is caused by vertical or lateral forces exerted onto the bound proteins.

Since the binding chemistry of the SAv-Bt bindings will not change when switching AFMs, the given assay could be used to actually benchmark the tip effects from different devices and tips. This would allow a quantitative comparison of different HS-AFM devices using a well known binding system which is relatively easy to handle in experiment. Also, as the general idea behind the given assay does not rely on the exact type of binding, it should be readily extendable to other binding systems as well. Furthermore, this assay could be used to ’compile’ a library of HS-AFM settings which allow sufficiently unbiased measurements on a number of binding systems.

Considering the assay presented in 5.1, it has been shown that HS-AFM can significantly speed up data acquisition compared to conventional AFM imaging. Even at a setpoint of 70% and a line rate of 70 Hz, the first images of the recorded videos showed full occupancy on the tracked origami. Thus, high-throughput screening using HS-AFM should be possible, at least for relatively strong binding systems. Keeping in mind the abrasive behavior of the rapidly scanning tip, HS-AFM can also be used to directly benchmark different protein ligand systems against each other since the target protein will almost immediately be ripped off weak binders or binder combinations by the rapidly scanning tip.

5.2.4 Materials and Methods

5.2.4.1 DNA origami assembly

The triangle DNA origami were assembled as described in chapter 5.1.4.1 using the same modified staple strands. The modified staple strands are added in a 10-fold excess to the unmodified staple strands of the solution to be assembled. After concentration of the purified DNA origami solution with the IMPLEN nanophotometer, the solution is diluted to 10 mM with 1 x TAE/$MgCl_2$.

5.2.4.2 The biotin modifications for the DNA origami substrates

DNA origami substrates were decorated with molecularly defined arrangements of 9 Bt modifications (Metabion) to allow the mono- and bidentate binding of SAv in Table 5.9 for the HS-AFM measurement.

Table 5.9: Sequences of all Bt-modified staple strands for the mono- and bidentate binding with four thymine spacers indicated in bold face, using Rothemund's original notation.

Modified staples		Oligonucleotide sequences 5' $\rightarrow$ 3'
Bt (T_4)	t-1s6e	**Bt-TTTT**TTAGTATCGCCAACGCTCAACAGTCGGCTGTC
Bt (T_4)	t-1s16e	**Bt-TTTT**ATTCGGTCTGCGGGATCGTCACCCGAAATCCG
Bt (T_4)	t-1s26e	**Bt-TTTT**GCCAGTGCGATCCCCGGGTACCGAGTTTTTCT
Bt (T_4)	t6s5g	**Bt-TTTT**CAGAGCCAGGAGGTTGAGGCAGGTAACAGTGCCCG
Bt (T_4)	t6s15g	**Bt-TTTT**ATAAAGCCTTTGCGGGAGAAGCCTGGAGAGGGTAG
Bt (T_4)	t6s25g	**Bt-TTTT**TCAATAGATATTAAATCCTTTGCCGGTTAGAACCT
Bt (T_4)	t6s7f	ATTAAAGGCCGTAATCAGTAGCGAGCCACCCT**TTTT-Bt**
Bt (T_4)	t6s17f	TAAGAGGTCAATTCTGCGAACGAGATTAAGCA**TTTT-Bt**
Bt (T_4)	t6s27f	CAATATTTGCCTGCAACAGTGCCATAGAGCCG**TTTT-Bt**

5.2.4.3 Sample preparation for HS-AFM measurement

In preparation for HS-AFM imaging, a total of 20 μl DNA origami solution with a concentration of 5 μM is pipetted onto mica in the sample chamber (Figure 5.25) and incubated for 2 minutes. Subsequently, the sample chamber is washed with 1 ml of a pH 7.5 adjusted 1 x TAE buffer (10 x TAE buffer, Roth) containing 10 mM $MgCl_2$ solution and again filled directly with 1 ml of a 20 nM SAv (Sigma-Aldrich) solution. The SAv solution is prepared and diluted as described in chapter 5.1.4.3. The sample chamber is clamped directly into the HS-AFM and after 1 h of incubation time the sample is ready for measurement at room temperature.

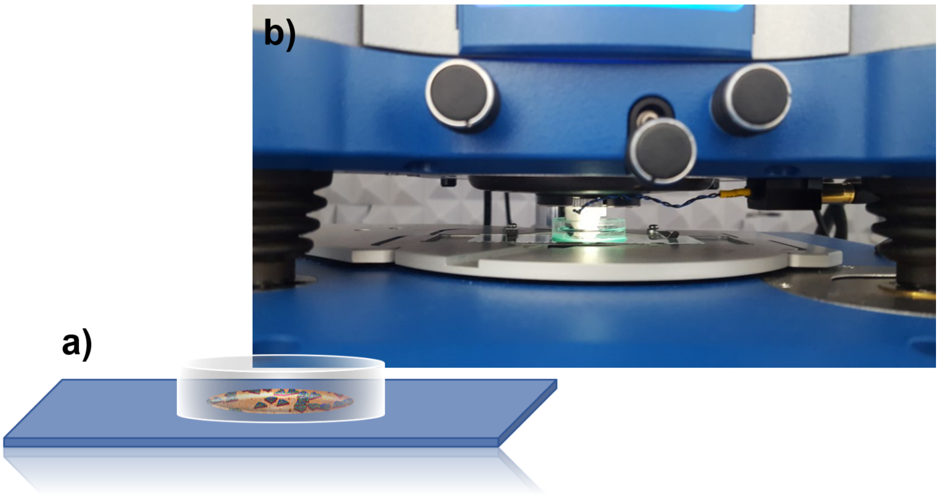

Figure 5.25: HS-AFM measuring stage. In a), the sample chamber for the HS-AFM measurement in liquid is shown schematically. The chamber consists of a glass substrate on which a plastic ring is glued. The circular mica sample is stuck in the chamber on the glass. b) shows the sample holder of the HS-AFM in which the sample chamber is clamped and the measuring head with clamped cantilever as it is immersed in the sample liquid.

5.2.4.4 HS-AFM imaging

HS-AFM imaging was performed using a JPK Nanowizard ULTRA Speed using a USC-F0.3-k0.3 cantilever (NanoWorld). The images were taken with scan sizes of 1×1 μm^2 and with a resolution of 512 px$\times$512 px. To quantify the tip effects, measurements were taken at amplitude setpoints of

70%, 80% and 90% using a series of selected line rates between 10 Hz and 70 Hz and a constant free amplitude of 3.3 nm.

5.2.4.5 Determination of binding yields from the recorded HS-AFM images

Time resolved binding yields were determined by manually counting the occupation of five selected origami on each recorded frame, averaging over a total of 15 monodentate and 15 bidentate SAv-Bt binding sites. The presented steady state binding yields have been determined by performing a linear fit with slope zero on the data for the last 100 s (from 500 s to 600 s) from each AFM video.

a)

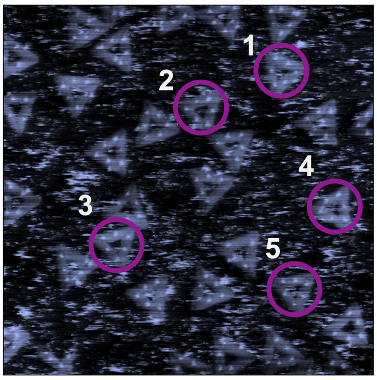

b)

Possible combinatons of				
2 origami		3 origami		4 origami
1 + 2	2 + 4	1 + 2 + 3	1 + 3 + 5	2 + 3 + 4 + 5
1 + 3	2 + 5	1 + 2 + 4	2 + 3 + 4	1 + 3 + 4 + 5
1 + 4	3 + 4	1 + 2 + 5	2 + 4 + 5	1 + 2 + 4 + 5
1 + 5	3 + 5	1 + 4 + 5	3 + 4 + 5	1 + 2 + 3 + 5
2 + 3	4 + 5	1 + 3 + 4	2 + 3 + 5	1 + 2 + 3 + 4

Figure 5.26: Possible origami combinations taking into account two, three, and four out of five origami, respectively. In a) a AFM image is shown with circles indicating the tracked origami. The table in b) lists all possible origami combinations for taking into account two, three, and four out of five origami, respectively.

To decide whether five DNA origami per parameter setting are sufficient for a statistics, the averaged steady state binding yield considering only two, three, and four of the five tracked DNA origami were calculated as well. Figure 5.26 a) shows a single AFM image indicating the five tracked DNA origami. The table in Figure 5.26 b) shows all possible combinations for a given number of DNA origami taken into account for determination of the steady state binding yield. In order to get a reasonable measure of the steady state binding yield obtained from tracking a given number of DNA origami, for each of the possible combinations, the steady state binding yield has been determined as described above. Then the average of the resulting yields has been taken with the standard deviation as an error measure. Figure 5.27 a) shows the averaged steady state binding yield depending on the number of evaluated origami. In case of the data point for four DNA origami, for example, the presented yield is the average of the steady state binding yield for all five possible combinations resulting from picking four out of five DNA origami. Figure 5.28 shows the time resolved binding yields for both, mono- and bidentate binding, for all possible combinations of four out of five origami. The determined steady state binding yields for the individual combinations are listed in Table 5.10. The data point for five tracked origami is somewhat special since there is only one possibility to pick five out of five origami. In this case, the exact error is in principle unknown. However, the decreasing trend of the determined errors suggests that the actual error here should be on the order of $\sim$5% for both, mono- and bidentate binding.

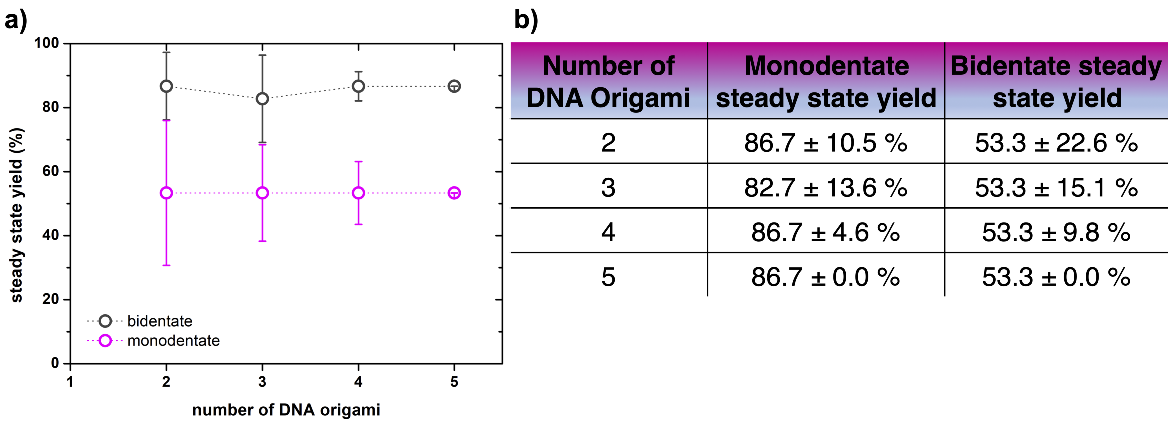

Number of DNA Origami	Monodentate steady state yield	Bidentate steady state yield
2	86.7 ± 10.5 %	53.3 ± 22.6 %
3	82.7 ± 13.6 %	53.3 ± 15.1 %
4	86.7 ± 4.6 %	53.3 ± 9.8 %
5	86.7 ± 0.0 %	53.3 ± 0.0 %

Figure 5.27: Steady state binding yields determined from different numbers of origami at an amplitude setpoint of 80% and a line rate of 50 Hz. a) the averages of the steady state binding yields for mono- and bidentate binding for 2, 3, 4 and 5 DNA origami. b) the corresponding data points of the averaged steady state binding yields of the DNA origami.

Table 5.10: Determined steady state binding yields for all possible combinations of four out of five DNA origami.

Combination	Monodentate yield / %	Bidentate yield / %
1 + 2 + 3 + 4	53.8 ± 1.3	91.7 ± 0.0
1 + 2 + 3 + 5	$58.3 \pm 2.8{\cdot}10^{-7}$	$83.3 \pm 4.9{\cdot}10^{-7}$
1 + 2 + 4 + 5	42.4 ± 0.8	91.7 ± 0.0
1 + 3 + 4 + 5	45.5 ± 1.3	$83.3 \pm 4.9{\cdot}10^{-7}$
2 + 3 + 4 + 5	66.7 ± 0.0	$83.3 \pm 4.9{\cdot}10^{-7}$

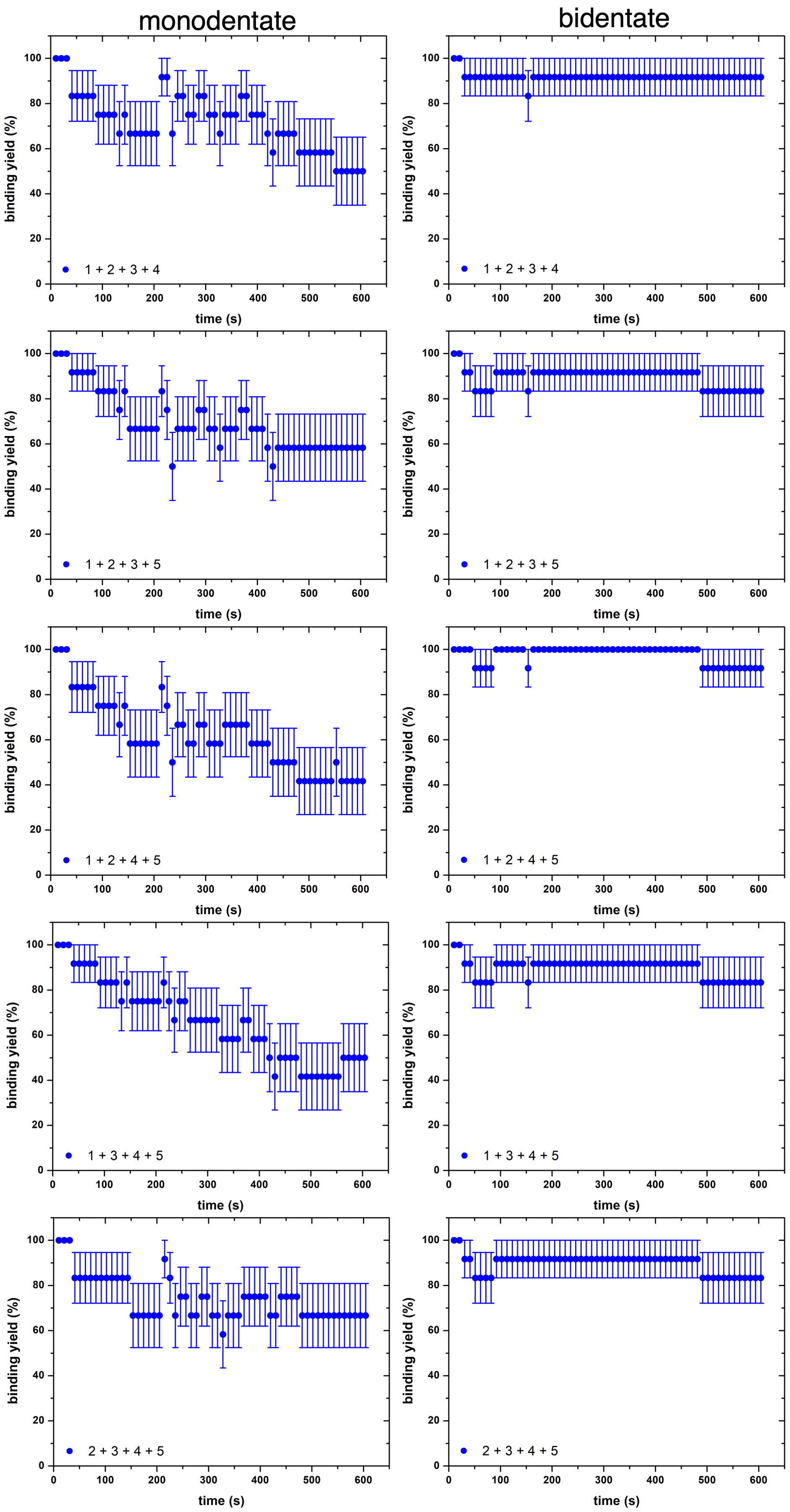

Figure 5.28: Time resolved binding yields for mono- and bidentate SAv-Bt binding for all possible combinations considering four out of the five tracked origami.

Chapter 6

Summary and Outlook

The first part of this thesis was devoted to the structural stability of DNA origami nanostructures in low Mg^{2+} buffer solutions and after long-term cryo storage of the staple strands used for assembly of the DNA origami. Both are important aspects for drug-delivery and drug-discovery applications as well. Considering drug delivery, the high magnesium concentrations typically used during assembly of the DNA origami are an issue since the magnesium concentrations under physiological conditions are much lower. Within this work, the structural stability in different low magnesium buffers has been investigated. It was demonstrated that, employing rationally selected buffers, high Mg^{2+} concentrations are by no means a prerequisite for maintaining DNA origami stability [151]. Considering applications which are not compatible with high Mg^{2+} concentrations such as fluorescence or enzyme activity analysis, the presented results show a number of valid alternative buffer solutions with a much lower Mg^{2+} concentration in the low μM range. Focusing on the second addressed problem, namely the long-term storage of the staple strands, the effects of staple age on the self-assembly and stability of DNA origami triangles, 6HBs, and 24HBs were investigated [152]. The results have shown that the respective staple solution may be stored at -20°C for several years without significantly affecting DNA origami assembly. At the same time, however, staple age may have drastic effects on DNA origami stability under mildly denaturing conditions, as exemplified here for the washing of surface-immobilized DNA origami with water. Nucleobase damage has been identified as a probable explanation for the decreased stability, as MALDI-TOF spectra of the used staple strands recorded at different ages did not indicate fragmentation of the staple strands due to the cryo-storage. Furthermore, these effects were found to depend on DNA origami shape and structure [152]. Keeping in mind that for medical applications long-term storage may be an issue, the presented results can give reasonable estimates about the storability of the investigated DNA origami structures. However, as the results have also shown, the negative effects depend on the structure of the used DNA origami. To this end, no universal guidance can be given on the maximum storage duration. For DNA origami structures used in actual applications, similar stability studies will have to be performed separately.

The second part of this work was concerned with applications of DNA origami nanostructures in the context of fragment–based drug-discovery. Here, results of a DNA origami-based single-molecule binding assay to quantitatively study mono- and multidentate protein-ligand interactions were presented. Compared to conventional screening methods used for drug discovery [39, 46] the assay can handle low protein concentrations in the nM range and does not require target immobilization on solid supports. Additionally it was shown, that different protein-ligand systems may be studied on the same DNA origami simultaneously which allows a direct comparison of different fragments using the results from a single experiment. By extending this approach to medically relevant protein-ligand systems, the detailed investigation of the effect of the geometric arrangement of multiple pharmacophores on their inhibitory effect becomes possible. Thus, the used single-molecule binding assay may not only be used for fragment optimization but also to aid the discovery of Lead components to design drug molecules with an optimal inhibitory effect.

As image acquisition using AFM and manual evaluation of the recorded images are time consuming tasks, the applicability of HS-AFM imaging to accelerate the data collection process has also been investigated by determining mono- and bidentate binding yields in dependence of various scan parameters, such as scan rate and amplitude set point. It has been demonstrated that a DNA origami system similar to the one used for the single-molecule binding assay is suitable to quantify tip effects arising in HS-AFM measurements. The results show, that even for one of the strongest non-covalently bound systems, the rapidly scanning AFM tip significantly affects the imaged system. It was also demonstrated that under reasonable conditions HS-AFM may be employed to drastically speed up image acquisition which allows a much faster screening experiments. Considering such strongly bound systems line rates below 30 Hz were found to have almost negligible effects on the imaged system. On the other hand, for less strongly bound system, the situation may change significantly. However, the presented assay may easily be adjusted to other binding systems which would allow a compilation of HS-AFM parameter sets for unbiased measurements depending on the observed system. In addition the given assay can be used to benchmark a given AFM device since the binding chemistry of the SAv-Bt system does not change when switching the imaging device.

List of Figures

2.1 Overview of the first DNA origami created by Rothemund. 8
2.2 3D-DNA origami 9
2.3 Schematic of two processes to prepare DNA origami with attached proteins [12]. . . 10
2.4 Structural representation of Bt and its derivatives 11
2.5 Schematic illustration of modified DNA origami rectangles with two sorts of modifications. 11
2.6 Schematic illustration of a DNA origami with selectively removable modifications [59]. 12
2.7 Illustration of an EMSA experiment to demonstrate successful binding of SAv to DNA strands modified with Bt-derivates [53]. 13
2.8 Illustration of a switchable protein pattern on a DNA origami. 13
2.9 Schematic illustration of the formation of individual Bt-SAv bonds at different positions on the DNA origami. 14
2.10 DNA origami systems which retain their structural integrity under biochemical and biophysical conditions. 16
2.11 Origami doxorubicin delivery system 17

3.1 Schematic of the measurement technique of an AFM. 22
3.2 Schematic curve of the force between the AFM tip and the sample indicating the regions of the most commonly used AFM modes. 23
3.3 Examples for perfectly sinusoidal surfaces in 1D and 2D 27
3.4 Schematic representation of parachuting [136]. 27
3.5 USC Cantilever used for HS-AFM [147]. 29
3.6 A schematic of the OBD detection system [142]. 30
3.7 Different setups to minimize undesired vibrations cause by the piezoelectric actuators. 31
3.8 Schematic layout of the HS-AFM and AFM. 32

4.1 AFM images of triangular DNA origami before and after spin filtering 37
4.2 AGE results for DNA origami triangles and 6HBs 37
4.3 AFM images of DNA origami triangles, 24HBs, and 6HBs in 1 x TAE containing 10 mM $MgCl_2$ for different numbers of filtering/washing cycles with pure water. 38
4.4 AFM images of DNA origami triangles, 24HBs, and 6HBs after transfer into different buffers. 40
4.5 AFM images of triangular DNA origami in 10 mM Na_2HPO_4 + 200 mM NaCl. . . . 40
4.6 AGE results for different DNA origami structures before and after transfer into water from different buffers. 41
4.7 AFM images of triangular DNA origami in water after different numbers of filtering/washing cycles at the day of preparation, after 84 days, and after 147 days. 42
4.8 Fraction of intact DNA origami triangles in water after different numbers of filtering/washing cycles as a function of time. 43

4.9 AFM images of triangular DNA origami in 10 mM Tris after two filtering/washing cycles at the day of preparation, after 70 days, and after 126 days. 43
4.10 AFM images of triangular DNA origami in different low Mg^{2+} buffer solutions after two filtering/washing cycles at the day of preparation, after 28 days, and after 56 days. 44
4.11 Fraction of intact DNA origami triangles in different buffers after two filtering/washing cycles as a function of time. 44
4.12 AFM image of triangular DNA origami after three filtering/washing cycles with pure water. 47
4.13 AFM images of DNA origami triangles assembled from staple sets of different ages. 49
4.14 Representative AFM zooms of Rothemund triangles categorized as a) intact, b) broken, c) denatured, and d) deformed. 51
4.15 Yields of intact, broken, denatured, and deformed DNA origami depending on the age of the staple solution for measurements in liquid, measurements using the dry-dipped protocol, and measurements using the dry-rinsed protocol. 52
4.16 Stability results for 6HB DNA origami. 53

5.1 Representative AFM image of iBt nanoarrays (5 nM) taken after incubation with 250 nM SAv for 30 min. 59
5.2 Representative AFM image of iBt nanoarrays (5 nM) with different spacer lengths as shown in the scheme, taken after incubation with 250 nM SAv for 30 min. 61
5.3 Sample AFM images of different quality. 62
5.4 Scheme and AFM zooms of single DNA origami showing bidentate SAv-iBt binding with spacer length T_4, as well as monodentate SAv-Bt binding with spacer length T_8. 62
5.5 Scheme and AFM zooms of single DNA origami showing nonspecific SAv binding to the left and right iBt positions. 63
5.6 Scheme and AFM zooms of single DNA origami showing AGP binding to P1, P2, and P1+P2, respectively. 63
5.7 Representative AFM image used for determination of the binding yield. 64
5.8 Schemes and AFM images of DNA origami triangles with single Bt modifications attached via different spacer lengths (T_8 and T_0). 65
5.9 Scheme of bidentate protein binding to two pharmacophores attached to the DNA origami substrate with too short a), optimized b), and too long spacers c), respectively. 66
5.10 Schematics of the DNA origami substrates indicating the positions of the modified staple strands for the experiments using trypsin, SAv, and AGP. 67
5.11 Representative AFM image of P1 and P2 nanoarrays (5 nM, see scheme) taken after incubation with 60 nM SAv and 50 nM AGP for 30 min. 68
5.12 Representative AFM image of multiple pharmacophore nanoarrays (5 nM, see scheme) taken after incubation with 250 nM SAv, 50 nM AGP, and 50 nM trypsin for 30 min. 69
5.13 Representative AFM images of P4 + P5 a), P4 + P6 b), and P4 + P7 c) pharmacophore nanoarrays (5 nM, see schemes) taken after incubation with 250 nM SAv and 50 nM trypsin for 30 min. 70
5.14 Structures of the pharmacophore modifications used in this study. 72
5.15 Scaffold path and staple arrangement of the triangular DNA origami. 74
5.16 Zooms of the individual pharmacophore-modified staples. 74
5.17 Occupation of Bt modified positions over a time of 20 minutes for both mono- and bidentate binding to SAv. 77

5.18 Selected images taken from a 20 minute HS-AFM video. 78
5.19 Determined steady state binding yields for mono- and bidentate SAv-Bt binding depending on the line rate and amplitude setpoint. 79
5.20 Steady state binding yields obtained at different line rates using a setpoint of 70%. . . 80
5.21 Steady state binding yields obtained at different line rates using a setpoint of 80%. . . 81
5.22 Steady state binding yields obtained at different line rates using a setpoint of 90%. . . 82
5.23 Selected AFM images recorded at a setpoint of 80% and different line rates. 83
5.24 Selected AFM images taken from an HS-AFM video recorded at 50 Hz line rate and setpoints of 70%, 80%, and 90%. 84
5.25 HS-AFM measuring stage. 86
5.26 Possible origami combinations taking into account two, three, and four out of five origami, respectively. 87
5.27 Steady state binding yields determined from different numbers of origami at an amplitude setpoint of 80% and a line rate of 50 Hz. 88
5.28 Time resolved binding yields for mono- and bidentate SAv-Bt binding for all possible combinations considering four out of the five tracked origami. 89

List of Tables

3.1 Comparison of the AFM against HS-AFM with some key data of the systems and used cantilever tips. 33

4.1 Average concentrations (in μM) of residual Mg^{2+} for each DNA origami after each filtering/washing cycle. 46
4.2 Buffer solutions and their respective pH value considered for the stability studies. . . 46
4.3 Number of analyzed DNA origami triangles $N_{(DNAorigami)}$ for each of the 8 AFM images recorded after dipping a sample assembled from 38 months old staples and the corresponding yields of intact, broken, deformed, and denatured DNA origami in %. 51
4.4 Yields (in %) of intact, broken, and denatured Rothemund triangles assembled from staples of different age obtained by AFM in liquid. 51
4.5 Yields (in %) of intact, broken, denatured, and deformed Rothemund triangles assembled from staples of different age obtained by AFM in the dry state after dip-washing. 52
4.6 Yields (in %) of intact, broken, denatured, and deformed Rothemund triangles assembled from staples of different age obtained by AFM in the dry state after rinsing. 52

5.1 Determined binding yields for monodentate and bidentate SAv-iBt binding depending on the incubation time as presented in Figure 5.1 d). 60
5.2 Determination of monodentate and bidentate binding yields for SAv-iBt binding at an incubation time of 30 min (Figure 5.1 d) of the chapter 5.1.2). 63
5.3 Determined binding yields for bidentate SAv-iBt binding depending on the spacer lengths as presented in Figure 5.1 e). 64
5.4 Determined binding yields for monodentate and bidentate AGP binding as presented in Figure 5.10 d). 67
5.5 Determined binding yields for bidentate binding of trypsin, bidentate binding of SAv and monodentate binding of AGP as presented in Figure 5.10 e). 69
5.6 Binding yield of mono- and bidentate binding of trypsin to fragments P4 to P7 as presented in Figure 5.10 f). 70
5.7 Sequences of all pharmacophore-modified staples, using Rothemund's original notation. 73
5.8 Stationary binding yield determined from the last 100 s of 500 to 600 s by linear regression for a constant function of the mono- and bidentate positions on the DNA origami at 70, 80, and 90% setpoint and 10–70 Hz line rate. 79
5.9 Sequences of all Bt-modified staple strands for the mono- and bidentate binding with four thymine spacers indicated in bold face, using Rothemund's original notation. . . 86
5.10 Determined steady state binding yields for all possible combinations of four out of five DNA origami. 88

Bibliography

[1] Nadrian C. Seeman. Nucleic acid junctions and lattices. *Journal of Theoretical Biology*, 99(2):237–247, 1982.

[2] N. C. Seeman and N. R. Kallenbach. Design of immobile nucleic acid junctions. *Biophysical Journal*, 44(2):201–209, 1983.

[3] J. H. Chen and N. C. Seeman. Synthesis from DNA of a molecule with the connectivity of a cube. *Nature*, 350(6319):631–633, 1991.

[4] Nadrian C. Seeman. The design and engineering of nucleic acid nanoscale assemblies. *Current opinion in structural biology*, 6(4):519–526, 1996.

[5] Xiaojun Li, Xiaoping Yang, Jing Qi, and Nadrian C. Seeman. Antiparallel DNA Double Crossover Molecules As Components for Nanoconstruction. *Journal of the American Chemical Society*, 118(26):6131–6140, 1996.

[6] E. Winfree, F. Liu, L. A. Wenzler, and N. C. Seeman. Design and self-assembly of two-dimensional DNA crystals. *Nature*, 394(6693):539–544, 1998.

[7] Dage Liu, Mingsheng Wang, Zhaoxiang Deng, Richard Walulu, and Chengde Mao. Tensegrity: construction of rigid DNA triangles with flexible four-arm DNA junctions. *Journal of the American Chemical Society*, 126(8):2324–2325, 2004.

[8] Paul W. K. Rothemund, Nick Papadakis, and Erik Winfree. Algorithmic self-assembly of DNA Sierpinski triangles. *PLoS biology*, 2(12):e424, 2004.

[9] Kyle Lund, Yan Liu, Stuart Lindsay, and Hao Yan. Self-assembling a molecular pegboard. *Journal of the American Chemical Society*, 127(50):17606–17607, 2005.

[10] Sung Ha Park, Constantin Pistol, Sang Jung Ahn, John H. Reif, Alvin R. Lebeck, Chris Dwyer, and Thomas H. LaBean. Finite-size, fully addressable DNA tile lattices formed by hierarchical assembly procedures. *Angewandte Chemie (International ed. in English)*, 45(5):735–739, 2006.

[11] Arkadiusz Chworos, Isil Severcan, Alexey Y. Koyfman, Patrick Weinkam, Emin Oroudjev, Helen G. Hansma, and Luc Jaeger. Building programmable jigsaw puzzles with RNA. *Science (New York, N.Y.)*, 306(5704):2068–2072, 2004.

[12] Kimmo T Laitinen Anton Kuzyk and P. Törmä. DNA origami as a nanoscale template for protein assembly. *Nanotechnology*, 20:235305 (5pp), 2009.

[13] Suchetan Pal, Zhengtao Deng, Baoquan Ding, Hao Yan, and Yan Liu. DNA-origami-directed self-assembly of discrete silver-nanoparticle architectures. *Angewandte Chemie (International ed. in English)*, 49(15):2700–2704, 2010.

[14] C. Mao, W. Sun, Z. Shen, and N. C. Seeman. A nanomechanical device based on the B-Z transition of DNA. *Nature*, 397(6715):144–146, 1999.

[15] B. Yurke, A. J. Turberfield, A. P. Mills, F. C. Simmel, and J. L. Neumann. A DNA-fuelled molecular machine made of DNA. *Nature*, 406(6796):605–608, 2000.

[16] A. P. Alivisatos, K. P. Johnsson, X. Peng, T. E. Wilson, C. J. Loweth, M. P. Bruchez, and P. G. Schultz. Organization of 'nanocrystal molecules' using DNA. *Nature*, 382(6592):609–611, 1996.

[17] Jiwen Zheng, Pamela E. Constantinou, Christine Micheel, A. Paul Alivisatos, Richard A. Kiehl, and Nadrian C. Seeman. Two-dimensional nanoparticle arrays show the organizational power of robust DNA motifs. *Nano letters*, 6(7):1502–1504, 2006.

[18] Barbara Saccà, Rebecca Meyer, Michael Erkelenz, Kathrin Kiko, Andreas Arndt, Hendrik Schroeder, Kersten S. Rabe, and Christof M. Niemeyer. Orthogonal protein decoration of DNA origami. *Angewandte Chemie (International ed. in English)*, 49(49):9378–9383, 2010.

[19] Sung Yong Park, Abigail K. R. Lytton-Jean, Byeongdu Lee, Steven Weigand, George C. Schatz, and Chad A. Mirkin. DNA-programmable nanoparticle crystallization. *Nature*, 451(7178):553–556, 2008.

[20] Christian Heck, Julia Prinz, André Dathe, Virginia Merk, Ondrej Stranik, Wolfgang Fritzsche, Janina Kneipp, and Ilko Bald. Gold Nanolenses Self-Assembled by DNA Origami. *ACS photonics*, 4(5):1123–1130, 2017.

[21] Anton Kuzyk, Robert Schreiber, Zhiyuan Fan, Günther Pardatscher, Eva-Maria Roller, Alexander Högele, Friedrich C. Simmel, Alexander O. Govorov, and Tim Liedl. DNA-based self-assembly of chiral plasmonic nanostructures with tailored optical response. *Nature*, 483(7389):311–314, 2012.

[22] Shawn M. Douglas, James J. Chou, and William M. Shih. DNA-nanotube-induced alignment of membrane proteins for NMR structure determination. *Proceedings of the National Academy of Sciences of the United States of America*, 104(16):6644–6648, 2007.

[23] Paul W. K. Rothemund. Folding DNA to create nanoscale shapes and patterns. *Nature*, 440:297, 2006.

[24] Ebbe S. Andersen, Mingdong Dong, Morten M. Nielsen, Kasper Jahn, Ramesh Subramani, Wael Mamdouh, Monika M. Golas, Bjoern Sander, Holger Stark, Cristiano L. P. Oliveira, Jan Skov Pedersen, Victoria Birkedal, Flemming Besenbacher, Kurt V. Gothelf, and Jørgen Kjems. Self-assembly of a nanoscale DNA box with a controllable lid. *Nature*, 459(7243):73–76, 2009.

[25] Akinori Kuzuya and Makoto Komiyama. Design and construction of a box-shaped 3D-DNA origami. *Chemical communications (Cambridge, England)*, (28):4182–4184, 2009.

[26] Yonggang Ke, Jaswinder Sharma, Minghui Liu, Kasper Jahn, Yan Liu, and Hao Yan. Scaffolded DNA origami of a DNA tetrahedron molecular container. *Nano letters*, 9(6):2445–2447, 2009.

[27] Masayuki Endo, Kumi Hidaka, Takayuki Kato, Keiichi Namba, and Hiroshi Sugiyama. DNA prism structures constructed by folding of multiple rectangular arms. *Journal of the American Chemical Society*, 131(43):15570–15571, 2009.

[28] Masayuki Endo, Kumi Hidaka, and Hiroshi Sugiyama. Direct AFM observation of an opening event of a DNA cuboid constructed via a prism structure. *Organic & biomolecular chemistry*, 9(7):2075–2077, 2011.

[29] Shawn M. Douglas, Hendrik Dietz, Tim Liedl, Björn Högberg, Franziska Graf, and William M. Shih. Self-assembly of DNA into nanoscale three-dimensional shapes. *Nature*, 459(7245):414–418, 2009.

[30] Hendrik Dietz, Shawn M. Douglas, and William M. Shih. Folding DNA into twisted and curved nanoscale shapes. *Science (New York, N.Y.)*, 325(5941):725–730, 2009.

[31] Yonggang Ke, Shawn M. Douglas, Minghui Liu, Jaswinder Sharma, Anchi Cheng, Albert Leung, Yan Liu, William M. Shih, and Hao Yan. Multilayer DNA origami packed on a square lattice. *Journal of the American Chemical Society*, 131(43):15903–15908, 2009.

[32] Hua Yang, Christopher K. McLaughlin, Faisal A. Aldaye, Graham D. Hamblin, Andrzej Z. Rys, Isabelle Rouiller, and Hanadi F. Sleiman. Metal-nucleic acid cages. *Nature chemistry*, 1(5):390–396, 2009.

[33] Bryan Wei, Mingjie Dai, and Peng Yin. Complex shapes self-assembled from single-stranded DNA tiles. *Nature*, 485(7400):623–626, 2012.

[34] Shawn M. Douglas, Ido Bachelet, and George M. Church. A logic-gated nanorobot for targeted transport of molecular payloads. *Science (New York, N.Y.)*, 335(6070):831–834, 2012.

[35] Pik Kwan Lo, Pierre Karam, Faisal A. Aldaye, Christopher K. McLaughlin, Graham D. Hamblin, Gonzalo Cosa, and Hanadi F. Sleiman. Loading and selective release of cargo in DNA nanotubes with longitudinal variation. *Nature chemistry*, 2(4):319–328, 2010.

[36] Qian Zhang, Qiao Jiang, Na Li, Luru Dai, Qing Liu, Linlin Song, Jinye Wang, Yaqian Li, Jie Tian, Baoquan Ding, and Yang Du. DNA origami as an in vivo drug delivery vehicle for cancer therapy. *ACS nano*, 8(7):6633–6643, 2014.

[37] Suping Li, Qiao Jiang, Shaoli Liu, Yinlong Zhang, Yanhua Tian, Chen Song, Jing Wang, Yiguo Zou, Gregory J. Anderson, Jing-Yan Han, Yung Chang, Yan Liu, Chen Zhang, Liang Chen, Guangbiao Zhou, Guangjun Nie, Hao Yan, Baoquan Ding, and Yuliang Zhao. A DNA nanorobot functions as a cancer therapeutic in response to a molecular trigger in vivo. *Nature biotechnology*, 36(3):258–264, 2018.

[38] Yang Yang, Jing Wang, Hideki Shigematsu, Weiming Xu, William M. Shih, James E. Rothman, and Chenxiang Lin. Self-assembly of size-controlled liposomes on DNA nanotemplates. *Nature chemistry*, 8(5):476–483, 2016.

[39] D. A. Erlanson, R. S. McDowell, and Tom O'Brian. Fragment-Based Drug Discovery. *Journal of Medicinal Chemistry*, 47(14):3463–3482, 2004.

[40] Xiao Qing Lewell, Duncan B. Judd, Stephen P. Watson, and Michael M. Hann. RECAP – Retrosynthetic Combinatorial Analysis Procedure: A Powerful New Technique for Identifying Privileged Molecular Fragments with Useful Applications in Combinatorial Chemistry. *Journal of Chemical Information and Computer Sciences*, 38(3):511–522, 1998.

[41] Philip J. Hajduk, Mark Bures, Jens Praestgaard, and Stephen W. Fesik. Privileged Molecules for Protein Binding Identified from NMR-Based Screening. *Journal of Medicinal Chemistry*, 43(18):3443–3447, 2000.

[42] Michal Vieth, Miles G. Siegel, Richard E. Higgs, Ian A. Watson, Daniel H. Robertson, Kenneth A. Savin, Gregory L. Durst, and Philip A. Hipskind. Characteristic Physical Properties and Structural Fragments of Marketed Oral Drugs. *Journal of Medicinal Chemistry*, 47(1):224–232, 2004. PMID: 14695836.

[43] Hans-Joachim Böhm. A novel computational tool for automated structure-based drug design. *Journal of Molecular Recognition*, 6(3):131–137, 1993.

[44] C. L. M. J. Verlinde, G. Rudenko, and W. G. J. Hol. In search of new lead compounds for trypanosomiasis drug design: A protein structure-based linked-fragment approach. *Journal of Computer-Aided Molecular Design*, 6(2):131–147, 1992.

[45] P.-L. Chau and P. M. Dean. Automated site-directed drug design: The generation of a basic set of fragments to be used for automated structure assembly. *Journal of Computer-Aided Molecular Design*, 6(4):385–396, 1992.

[46] D. J. Maly, I. C. Choong, and J. A. Ellman. Combinatorial target-guided ligand assembly: Identification of potent subtype-selective c-Src inhibitors. *Proceedings of the National Academy of Sciences*, 97(6):2419–2424, 2000.

[47] S. A. Hofstadler and R. H. Griffey. Analysis of Noncovalent Complexes of DNA and RNA by Mass Spectrometry. *Chemical Reviews*, 101(2):377–390, 2001.

[48] A. Sharff and H. Jhoti. High-throughput crystallography to enhance drug discovery. *Current Opinion in Chemical Biology*, 7(3):340–345, 2003.

[49] Philip J. Hajduk, Jürgen Dinges, Jeffrey M. Schkeryantz, David Janowick, Michele Kaminski, Michael Tufano, David J. Augeri, Andrew Petros, Vicki Nienaber, Ping Zhong, Rachel Hammond, Michael Coen, Bruce Beutel, Leonard Katz, and Stephen W. Fesik. Novel Inhibitors of Erm Methyltransferases from NMR and Parallel Synthesis. *Journal of Medicinal Chemistry*, 42(19):3852–3859, 1999.

[50] A. Ganesan. Strategies for the Dynamic Integration of Combinatorial Synthesis and Screening. *Angewandte Chemie International Edition*, 37(20):2828–2831, 1998.

[51] O. Ramström and J.-M. Lehn. Drug discovery by dynamic combinatorial libraries. *Nature Reviews Drug Discovery*, 1(1):26–36, 2002.

[52] Arivazhagan Rajendran, Masayuki Endo, and Hiroshi Sugiyama. Single-molecule analysis using DNA origami. *Angewandte Chemie (International ed. in English)*, 51(4):874–890, 2012.

[53] Arivazhagan Rajendran, Masayuki Endo, Kumi Hidaka, and Hiroshi Sugiyama. Direct and single-molecule visualization of the solution-state structures of G-hairpin and G-triplex intermediates. *Angewandte Chemie (International ed. in English)*, 53(16):4107–4112, 2014.

[54] Zhen-Gang Wang and Baoquan Ding. Engineering DNA Self-Assemblies as Templates for Functional Nanostructures. *Accounts of Chemical Research*, 47(6):1654–1662, 2014.

[55] Yuhe R. Yang, Yan Liu, and Hao Yan. DNA Nanostructures as Programmable Biomolecular Scaffolds. *Bioconjugate chemistry*, 26(8):1381–1395, 2015.

[56] T. Tørring, N. V. Voigt, J. Nangreave, H. Yan, and K. V. Gothelf. DNA origami: a quantum leap for self-assembly of complex structures. *Chemical Society Reviews*, 40:5636–5646, 2011.

[57] Ilko Bald and Adrian Keller. Molecular processes studied at a single-molecule level using DNA origami nanostructures and atomic force microscopy. *Molecules (Basel, Switzerland)*, 19(9):13803–13823, 2014.

[58] Adrian Keller, Ilko Bald, Alexandru Rotaru, Emilie Cauët, Kurt V. Gothelf, and Flemming Besenbacher. Probing electron-induced bond cleavage at the single-molecule level using DNA origami templates. *ACS Nano*, 6(5):4392–4399, 2012.

[59] Niels V. Voigt, Thomas Tørring, Alexandru Rotaru, Mikkel F. Jacobsen, Jens B. Ravnsbaek, Ramesh Subramani, Wael Mamdouh, Jørgen Kjems, Andriy Mokhir, Flemming Besenbacher, and Kurt Vesterager Gothelf. Single-molecule chemical reactions on DNA origami. *Nature nanotechnology*, 5(3):200–203, 2010.

[60] S. Helmig, A. Rotaru, D. Arian, L. Kovbasyuk, J. Arnbjerg, P. R. Ogilby, J. Kjems, A. Mokhir, F. Besenbacher, and K. V. Gothelf. Single Molecule Atomic Force Microscopy Studies of Photosensitized Singlet Oxygen Behavior on a DNA Origami Template. *ACS Nano*, 4(12):7475–7480, 2010. PMID: 21090671.

[61] C. Steinhauer, R. Jungmann, T. L. Sobey, F. C. Simmel, and P. Tinnefeld. DNA Origami as a Nanoscopic Ruler for Super-Resolution Microscopy. *Angewandte Chemie International Edition*, 48(47):8870–8873, 2009.

[62] Erik Benson, Abdulmelik Mohammed, Johan Gardell, Sergej Masich, Eugen Czeizler, Pekka Orponen, and Björn Högberg. DNA rendering of polyhedral meshes at the nanoscale. *Nature*, 523:441 EP –, 2015.

[63] L. T. Mazzola and S. P. A. Fodor. Imaging Biomolecule Arrays by Atomic Force Microscopy. *Biophysical Journal*, 68:1653–1660, May 1995.

[64] Weilin Lin, Francesco V. Reddavide, Veselina Uzunova, Fatih Nadi Gür, and Yixin Zhang. Characterization of DNA-conjugated compounds using a regenerable chip. *Analytical chemistry*, 87(2):864–868, 2015.

[65] N. Y. Wong, H. Xing, L. H. Tan, and Yi Lu. Nano-Encrypted Morse Code: A Versatile Approach to Programmable an Reversible Nanoscale Assembly and Disassembly. *J. Am. Chem. Soc.*, 135:2931–2934, 2012.

[66] Anders Holmberg, Anna Blomstergren, Olof Nord, Morten Lukacs, Joakim Lundeberg, and Mathias Uhlén. The biotin-streptavidin interaction can be reversibly broken using water at elevated temperatures. *Electrophoresis*, 26(3):501–510, 2005.

[67] N. M. Green. Spectrophotometric determination of avidin and biotin. In *Vitamins and Coenzymes*, volume 18 of *Methods in Enzymology*, pages 418–424. Academic Press, 1970.

[68] Marc P. Raphael, Catherine A. Rappole, Lynn K. Kurihara, Joseph A. Christodoulides, Syed N. Qadri, and Jeff M. Byers. Iminobiotin binding induces large fluorescent enhancements in avidin and streptavidin fluorescent conjugates and exhibits diverging pH-dependent binding affinities. *Journal of fluorescence*, 21(2):647–652, 2011.

[69] Sherri Rinker, Yonggang Ke, Yan Liu, Rahul Chhabra, and Hao Yan. Self-assembled DNA nanostructures for distance-dependent multivalent ligand-protein binding. *Nature nanotechnology*, 3(7):418–422, 2008.

[70] A. Kuzuya *et al.* Nanomechanical DNA origami 'single-molecule beacons' directly imaged by atomic force microscopy. *Nature Comm.*, 2(449), 2011.

[71] Ping Zhang, Fei Wang, Wenjing Liu, Xiuhai Mao, Changchun Hao, Yi Zhang, Chunhai Fan, Jun Hu, Lihua Wang, and Bin Li. Quantitative Measurement of Spatial Effects of DNA Origami on Molecular Binding Reactions Detected using Atomic Force Microscopy. *ACS applied materials & interfaces*, 11(24):21973–21981, 2019.

[72] Dongran Han, Suchetan Pal, Jeanette Nangreave, Zhengtao Deng, Yan Liu, and Hao Yan. DNA origami with complex curvatures in three-dimensional space. *Science (New York, N.Y.)*, 332(6027):342–346, 2011.

[73] Denis Selnihhin and Ebbe Sloth Andersen. Computer-aided design of DNA origami structures. *Methods in molecular biology (Clifton, N.J.)*, 1244:23–44, 2015.

[74] Ebbe S. Andersen, Mingdong Dong, Morten M. Nielsen, Kasper Jahn, Allan Lind-Thomsen, Wael Mamdouh, Kurt V. Gothelf, Flemming Besenbacher, and Jørgen Kjems. DNA origami design of dolphin-shaped structures with flexible tails. *ACS nano*, 2(6):1213–1218, 2008.

[75] Florian Praetorius, Benjamin Kick, Karl L. Behler, Maximilian N. Honemann, Dirk Weuster-Botz, and Hendrik Dietz. Biotechnological mass production of DNA origami. *Nature*, 552(7683):84–87, 2017.

[76] Liwei Hui, Qinmei Zhang, Wei Deng, and Haitao Liu. DNA-Based Nanofabrication: Pathway to Applications in Surface Engineering. *Small (Weinheim an der Bergstrasse, Germany)*, 15(26):e1805428, 2019.

[77] Na Liu and Tim Liedl. DNA-Assembled Advanced Plasmonic Architectures. *Chemical reviews*, 118(6):3032–3053, 2018.

[78] Pengfei Wang, Travis A. Meyer, Victor Pan, Palash K. Dutta, and Yonggang Ke. The Beauty and Utility of DNA Origami. *Chem*, 2(3):359–382, 2017.

[79] Sunaina Surana, Avinash R. Shenoy, and Yamuna Krishnan. Designing DNA nanodevices for compatibility with the immune system of higher organisms. *Nature nanotechnology*, 10(9):741–747, 2015.

[80] Veikko Linko, Ari Ora, and Mauri A. Kostiainen. DNA Nanostructures as Smart Drug-Delivery Vehicles and Molecular Devices. *Trends in biotechnology*, 33(10):586–594, 2015.

[81] Anton Kuzyk, Ralf Jungmann, Guillermo P. Acuna, and Na Liu. DNA Origami Route for Nanophotonics. *ACS photonics*, 5(4):1151–1163, 2018.

[82] Anupama J. Thubagere, Wei Li, Robert F. Johnson, Zibo Chen, Shayan Doroudi, Yae Lim Lee, Gregory Izatt, Sarah Wittman, Niranjan Srinivas, Damien Woods, Erik Winfree, and Lulu Qian. A cargo-sorting DNA robot. *Science (New York, N.Y.)*, 357(6356), 2017.

[83] Heini Ijäs, Sami Nummelin, Boxuan Shen, Mauri A. Kostiainen, and Veikko Linko. Dynamic DNA Origami Devices: from Strand-Displacement Reactions to External-Stimuli Responsive Systems. *International journal of molecular sciences*, 19(7), 2018.

[84] Saminathan Ramakrishnan, Heini Ijäs, Veikko Linko, and Adrian Keller. Structural stability of DNA origami nanostructures under application-specific conditions. *Computational and structural biotechnology journal*, 16:342–349, 2018.

[85] D. R. Duckett, A. I. Murchie, and D. M. Lilley. The role of metal ions in the conformation of the four-way DNA junction. *The EMBO Journal*, 9(2):583–590, 1990.

[86] Dianming Wang, Ziran Da, Bohan Zhang, Mark Antonin Isbell, Yuanchen Dong, Xu Zhou, Huajie Liu, Jerry Yong Yew Heng, and Zhongqiang Yang. Stability study of tubular DNA origami in the presence of protein crystallisation buffer. *RSC Advances*, 5(72):58734–58737, 2015.

[87] Benjamin Schuler and Hagen Hofmann. Single-molecule spectroscopy of protein folding dynamics–expanding scope and timescales. *Current opinion in structural biology*, 23(1):36–47, 2013.

[88] Pierandrea Lo Nostro and Barry W. Ninham. Hofmeister phenomena: an update on ion specificity in biology. *Chemical reviews*, 112(4):2286–2322, 2012.

[89] Saminathan Ramakrishnan, Georg Krainer, Guido Grundmeier, Michael Schlierf, and Adrian Keller. Structural stability of DNA origami nanostructures in the presence of chaotropic agents. *Nanoscale*, 8(19):10398–10405, 2016.

[90] Thomas Gerling, Massimo Kube, Benjamin Kick, and Hendrik Dietz. Sequence-programmable covalent bonding of designed DNA assemblies. *Science advances*, 4(8):eaau1157, 2018.

[91] Arivazhagan Rajendran, Masayuki Endo, Yousuke Katsuda, Kumi Hidaka, and Hiroshi Sugiyama. Photo-cross-linking-assisted thermal stability of DNA origami structures and its application for higher-temperature self-assembly. *Journal of the American Chemical Society*, 133(37):14488–14491, 2011.

[92] Haorong Chen, Ruixin Li, Shiming Li, Joakim Andréasson, and Jong Hyun Choi. Conformational Effects of UV Light on DNA Origami. *Journal of the American Chemical Society*, 139(4):1380–1383, 2017.

[93] Qiao Jiang, Chen Song, Jeanette Nangreave, Xiaowei Liu, Lin Lin, Dengli Qiu, Zhen-Gang Wang, Guozhang Zou, Xingjie Liang, Hao Yan, and Baoquan Ding. DNA origami as a carrier for circumvention of drug resistance. *Journal of the American Chemical Society*, 134(32):13396–13403, 2012.

[94] Jianhua Zhang and Ming Xu. Apoptotic DNA fragmentation and tissue homeostasis. *Trends in Cell Biology*, 12(2):84–89, 2002.

[95] Kumiko Samejima and William C. Earnshaw. Trashing the genome: the role of nucleases during apoptosis. *Nature reviews. Molecular cell biology*, 6(9):677–688, 2005.

[96] Carlos Ernesto Castro, Fabian Kilchherr, Do-Nyun Kim, Enrique Lin Shiao, Tobias Wauer, Philipp Wortmann, Mark Bathe, and Hendrik Dietz. A primer to scaffolded DNA origami. *Nature methods*, 8(3):221–229, 2011.

[97] Jaeseung Hahn, Shelley F. J. Wickham, William M. Shih, and Steven D. Perrault. Addressing the instability of DNA nanostructures in tissue culture. *ACS nano*, 8(9):8765–8775, 2014.

[98] Rémi Veneziano, Sakul Ratanalert, Kaiming Zhang, Fei Zhang, Hao Yan, Wah Chiu, and Mark Bathe. Designer nanoscale DNA assemblies programmed from the top down. *Science (New York, N.Y.)*, 352(6293):1534, 2016.

[99] Yasaman Ahmadi, Elisa de Llano, and Ivan Barišić. (Poly)cation-induced protection of conventional and wireframe DNA origami nanostructures. *Nanoscale*, 10(16):7494–7504, 2018.

[100] Zaixing Jiang, Shuai Zhang, Chuanxu Yang, Jørgen Kjems, Yudong Huang, Flemming Besenbacher, and Mingdong Dong. Serum-induced degradation of 3D DNA box origami observed with high-speed atomic force microscopy. *Nano Research*, 8(7):2170–2178, 2015.

[101] Xibo Shen, Qiao Jiang, Jinye Wang, Luru Dai, Guozhang Zou, Zhen-Gang Wang, Wei-Qiang Chen, Wei Jiang, and Baoquan Ding. Visualization of the intracellular location and stability of DNA origami with a label-free fluorescent probe. *Chemical communications (Cambridge, England)*, 48(92):11301–11303, 2012.

[102] Joona Mikkilä, Antti-Pekka Eskelinen, Elina H. Niemelä, Veikko Linko, Mikko J. Frilander, Päivi Törmä, and Mauri A. Kostiainen. Virus-encapsulated DNA origami nanostructures for cellular delivery. *Nano letters*, 14(4):2196–2200, 2014.

[103] Steven D. Perrault and William M. Shih. Virus-inspired membrane encapsulation of DNA nanostructures to achieve in vivo stability. *ACS nano*, 8(5):5132–5140, 2014.

[104] Aurélie Lacroix, Thomas G. W. Edwardson, Mark A. Hancock, Michael D. Dore, and Hanadi F. Sleiman. Development of DNA Nanostructures for High-Affinity Binding to Human Serum Albumin. *Journal of the American Chemical Society*, 139(21):7355–7362, 2017.

[105] Armando Hernandez-Garcia, Nicole A. Estrich, Marc W. T. Werten, Johan R. C. van der Maarel, Thomas H. LaBean, Frits A. de Wolf, Martien A. Cohen Stuart, and Renko de Vries. Precise Coating of a Wide Range of DNA Templates by a Protein Polymer with a DNA Binding Domain. *ACS nano*, 11(1):144–152, 2017.

[106] Nicole A. Estrich, Armando Hernandez-Garcia, Renko de Vries, and Thomas H. LaBean. Engineered Diblock Polypeptides Improve DNA and Gold Solubility during Molecular Assembly. *ACS nano*, 11(1):831–842, 2017.

[107] Henni Auvinen, Hongbo Zhang, Nonappa, Alisa Kopilow, Elina H. Niemelä, Sami Nummelin, Alexandra Correia, Hélder A. Santos, Veikko Linko, and Mauri A. Kostiainen. Protein Coating of DNA Nanostructures for Enhanced Stability and Immunocompatibility. *Advanced healthcare materials*, 6(18), 2017.

[108] Nayan P. Agarwal, Michael Matthies, Fatih N. Gür, Kensuke Osada, and Thorsten L. Schmidt. Block Copolymer Micellization as a Protection Strategy for DNA Origami. *Angewandte Chemie (International ed. in English)*, 56(20):5460–5464, 2017.

[109] Aradhana Chopra, Swati Krishnan, and Friedrich C. Simmel. Electrotransfection of Polyamine Folded DNA Origami Structures. *Nano letters*, 16(10):6683–6690, 2016.

[110] Jenny K. Kiviaho, Veikko Linko, Ari Ora, Tony Tiainen, Erika Järvihaavisto, Joona Mikkilä, Heikki Tenhu, Nonappa, and Mauri A. Kostiainen. Cationic polymers for DNA origami coating - examining their binding efficiency and tuning the enzymatic reaction rates. *Nanoscale*, 8(22):11674–11680, 2016.

[111] Nandhini Ponnuswamy, Maartje M. C. Bastings, Bhavik Nathwani, Ju Hee Ryu, Leo Y. T. Chou, Mathias Vinther, Weiwei Aileen Li, Frances M. Anastassacos, David J. Mooney, and William M. Shih. Oligolysine-based coating protects DNA nanostructures from low-salt denaturation and nuclease degradation. *Nature communications*, 8:15654, 2017.

[112] Boxuan Shen, Veikko Linko, Kosti Tapio, Siim Pikker, Tibebe Lemma, Ashwin Gopinath, Kurt V. Gothelf, Mauri A. Kostiainen, and J. Jussi Toppari. Plasmonic nanostructures through DNA-assisted lithography. *Science advances*, 4(2):eaap8978, 2018.

[113] Xiaoguo Liu, Fei Zhang, Xinxin Jing, Muchen Pan, Pi Liu, Wei Li, Bowen Zhu, Jiang Li, Hong Chen, Lihua Wang, Jianping Lin, Yan Liu, Dongyuan Zhao, Hao Yan, and Chunhai Fan. Complex silica composite nanomaterials templated with DNA origami. *Nature*, 559(7715):593–598, 2018.

[114] Bezu Teschome, Stefan Facsko, Tommy Schönherr, Jochen Kerbusch, Adrian Keller, and Artur Erbe. Temperature-Dependent Charge Transport through Individually Contacted DNA Origami-Based Au Nanowires. *Langmuir : the ACS journal of surfaces and colloids*, 32(40):10159–10165, 2016.

[115] Yanli Geng, Anthony C. Pearson, Elisabeth P. Gates, Bibek Uprety, Robert C. Davis, John N. Harb, and Adam T. Woolley. Electrically conductive gold- and copper-metallized DNA origami nanostructures. *Langmuir : the ACS journal of surfaces and colloids*, 29(10):3482–3490, 2013.

[116] Sumedh P. Surwade, Shichao Zhao, and Haitao Liu. Molecular lithography through DNA-mediated etching and masking of SiO2. *Journal of the American Chemical Society*, 133(31):11868–11871, 2011.

[117] Sumedh P. Surwade, Feng Zhou, Bryan Wei, Wei Sun, Anna Powell, Christina O'Donnell, Peng Yin, and Haitao Liu. Nanoscale growth and patterning of inorganic oxides using DNA nanostructure templates. *Journal of the American Chemical Society*, 135(18):6778–6781, 2013.

[118] Zhong Jin, Wei Sun, Yonggang Ke, Chih-Jen Shih, Geraldine L. C. Paulus, Qing Hua Wang, Bin Mu, Peng Yin, and Michael S. Strano. Metallized DNA nanolithography for encoding and transferring spatial information for graphene patterning. *Nature communications*, 4:1663, 2013.

[119] Boxuan Shen, Veikko Linko, Kosti Tapio, Mauri A. Kostiainen, and J. Jussi Toppari. Custom-shaped metal nanostructures based on DNA origami silhouettes. *Nanoscale*, 7(26):11267–11272, 2015.

[120] Saminathan Ramakrishnan, Sivaraman Subramaniam, A. Francis Stewart, Guido Grundmeier, and Adrian Keller. Regular Nanoscale Protein Patterns via Directed Adsorption through Self-Assembled DNA Origami Masks. *ACS applied materials & interfaces*, 8(45):31239–31247, 2016.

[121] Hüsnü Aslan, Abhichart Krissanaprasit, Flemming Besenbacher, Kurt V. Gothelf, and Mingdong Dong. Protein patterning by a DNA origami framework. *Nanoscale*, 8(33):15233–15240, 2016.

[122] Katerina Busuttil, Alexandru Rotaru, Mingdong Dong, Flemming Besenbacher, and Kurt V. Gothelf. Transfer of a protein pattern from self-assembled DNA origami to a functionalized substrate. *Chemical communications (Cambridge, England)*, 49(19):1927–1929, 2013.

[123] M. Sajfutdinow, K. Uhlig, A. Prager, C. Schneider, B. Abel, and D. M. Smith. Nanoscale patterning of self-assembled monolayer (SAM)-functionalised substrates with single molecule contact printing. *Nanoscale*, 9(39):15098–15106, 2017.

[124] Cheng Tian, Hyojeong Kim, Wei Sun, Yunah Kim, Peng Yin, and Haitao Liu. DNA Nanostructures-Mediated Molecular Imprinting Lithography. *ACS nano*, 11(1):227–238, 2017.

[125] S. P. Surwade, F. Zhou, Z. Li, A. Powell, C. O'Donnell, and H. Liu. Nanoscale patterning of self-assembled monolayers using DNA nanostructure templates. *Chemical communications (Cambridge, England)*, 52(8):1677–1680, 2016.

[126] Zhen-Gang Wang, Qing Liu, and Baoquan Ding. Shape-Controlled Nanofabrication of Conducting Polymer on Planar DNA Templates. *Chemistry of Materials*, 26(11):3364–3367, 2014.

[127] Jakob Bach Knudsen, Lei Liu, Anne Louise Bank Kodal, Mikael Madsen, Qiang Li, Jie Song, Johannes B. Woehrstein, Shelley F. J. Wickham, Maximilian T. Strauss, Florian Schueder, Jesper Vinther, Abhichart Krissanaprasit, Daniel Gudnason, Anton Allen Abbotsford Smith, Ryosuke Ogaki, Alexander N. Zelikin, Flemming Besenbacher, Victoria Birkedal, Peng Yin, William M. Shih, Ralf Jungmann, Mingdong Dong, and Kurt V. Gothelf. Routing of individual polymers in designed patterns. *Nature nanotechnology*, 10(10):892–898, 2015.

[128] Michelle A. Pillers and Marya Lieberman. Thermal stability of DNA origami on mica. *Journal of Vacuum Science & Technology B, Nanotechnology and Microelectronics: Materials, Processing, Measurement, and Phenomena*, 32(4):040602, 2014.

[129] Hyojeong Kim, Sumedh P. Surwade, Anna Powell, Christina O'Donnell, and Haitao Liu. Stability of DNA Origami Nanostructure under Diverse Chemical Environments. *Chemistry of Materials*, 26(18):5265–5273, 2014.

[130] Ashwin Gopinath and Paul W. K. Rothemund. Optimized assembly and covalent coupling of single-molecule DNA origami nanoarrays. *ACS nano*, 8(12):12030–12040, 2014.

[131] Ryan J. Kershner, Luisa D. Bozano, Christine M. Micheel, Albert M. Hung, Ann R. Fornof, Jennifer N. Cha, Charles T. Rettner, Marco Bersani, Jane Frommer, Paul W. K. Rothemund, and Gregory M. Wallraff. Placement and orientation of individual DNA shapes on lithographically patterned surfaces. *Nature nanotechnology*, 4(9):557–561, 2009.

[132] Bezuayehu Teshome, Stefan Facsko, and Adrian Keller. Topography-controlled alignment of DNA origami nanotubes on nanopatterned surfaces. *Nanoscale*, 6(3):1790–1796, 2014.

[133] Veikko Linko, Boxuan Shen, Kosti Tapio, J. Jussi Toppari, Mauri A. Kostiainen, and Sampo Tuukkanen. One-step large-scale deposition of salt-free DNA origami nanostructures. *Scientific reports*, 5:15634, 2015.

[134] G. Binning, C. F. Quate, and Ch. Gerber. Atomic Force Microscope. *Physical Review Letters*, 56:930, 1986.

[135] R. Wiesendanger. *Scanning Probe Microscopy and Spectroscopy: Methods and Applications*. Cambridge University Press, 1994.

[136] Toshio Ando, Takayuki Uchihashi, and Noriyuki Kodera. High-speed AFM and applications to biomolecular systems. *Annual review of biophysics*, 42:393–414, 2013.

[137] Sungwook Woo and Paul W. K. Rothemund. Self-assembly of two-dimensional DNA origami lattices using cation-controlled surface diffusion. *Nature Communications*, 5(1):4889, 2014.

[138] Charlotte Kielar, Saminathan Ramakrishnan, Sebastian Fricke, Guido Grundmeier, and Adrian Keller. Dynamics of DNA Origami Lattice Formation at Solid-Liquid Interfaces. *ACS applied materials & interfaces*, 10(51):44844–44853, 2018.

[139] D. M. Czajkowsky and Z. Shao. Inhibition of protein adsorption to muscovite mica by monovalent cations. *Journal of microscopy*, 211(Pt 1):1–7, 2003.

[140] Marie-Paule Mingeot-Leclercq, Magali Deleu, Robert Brasseur, and Yves F. Dufrêne. Atomic force microscopy of supported lipid bilayers. *Nature Protocols*, 3(10):1654–1659, 2008.

[141] Pilar Cea, Luz Marina Ballesteros, and Santiago Martín. Nanofabrication techniques of highly organized monolayers sandwiched between two electrodes for molecular electronics. *Nanofabrication*, 1(1), 2014.

[142] Toshio Ando, Takayuki Uchihashi, and Takeshi Fukuma. High-speed atomic force microscopy for nano-visualization of dynamic biomolecular processes. *Progress in Surface Science*, 83(7):337–437, 2008.

[143] T. Sulchek, G. G. Yaralioglu, C. F. Quate, and S. C. Minne. Characterization and optimization of scan speed for tapping-mode atomic force microscopy. *Review of Scientific Instruments*, 73(8):2928–2936, 2002.

[144] János Kokavecz, Othmar Marti, Péter Heszler, and Ádám Mechler. Imaging bandwidth of the tapping mode atomic force microscope probe. *Physical Review B*, 73(15):026118, 2006.

[145] Georg E. Fantner, Georg Schitter, Johannes H. Kindt, Tzvetan Ivanov, Katarina Ivanova, Rohan Patel, Niels Holten-Andersen, Jonathan Adams, Philipp J. Thurner, Ivo W. Rangelow, and Paul K. Hansma. Components for high speed atomic force microscopy. *Ultramicroscopy*, 106(8):881–887, 2006.

[146] T. R. Albrecht, P. Grütter, D. Horne, and D. Rugar. Frequency modulation detection using high– Q cantilevers for enhanced force microscope sensitivity. *Journal of Applied Physics*, 69(2):668–673, 1991.

[147] NanoWorld AG. SPM AND AFM PROBES. `https://www.nanoworld.com/`.

[148] T. E. Schäffer, J. P. Cleveland, F. Ohnesorge, D. A. Walters, and P. K. Hansma. Studies of vibrating atomic force microscope cantilevers in liquid. *Journal of Applied Physics*, 80(7):3622–3627, 1996.

[149] Daniel Y. Abramovitch, Sean B. Andersson, Lucy Y. Pao, and Georg Schitter. A Tutorial on the Mechanisms, Dynamics, and Control of Atomic Force Microscopes. In *2007 American Control Conference*, pages 3488–3502. I E E E, 2007.

[150] Bruker Corporation. High Speed AFM Imaging: Survey, Screening, and Dynamics with Bruker's Revolutionary FastScan Atomic Force Microscope. `https://www.bruker.com/fileadmin/user_upload/8-PDF-Docs/SurfaceAnalysis/AFM/Webinars/High_Speed_AFM_Imaging_with_the_Dimension_FastScan_Atomic_Force_Microscope.pdf`.

[151] Charlotte Kielar, Yang Xin, Boxuan Shen, Mauri A. Kostiainen, Guido Grundmeier, Veikko Linko, and Adrian Keller. On the Stability of DNA Origami Nanostructures in Low-Magnesium Buffers. *Angewandte Chemie (International ed. in English)*, 57(30):9470–9474, 2018.

[152] Charlotte Kielar, Yang Xin, Xiaodan Xu, Siqi Zhu, Nelli Gorin, Guido Grundmeier, Christin Möser, David M. Smith, and Adrian Keller. Effect of Staple Age on DNA Origami Nanostructure Assembly and Stability. *Molecules (Basel, Switzerland)*, 24(14), 2019.

[153] Sami Nummelin, Juhana Kommeri, Mauri A. Kostiainen, and Veikko Linko. Evolution of Structural DNA Nanotechnology. *Advanced materials (Deerfield Beach, Fla.)*, 30(24):e1703721, 2018.

[154] Fan Hong, Fei Zhang, Yan Liu, and Hao Yan. DNA Origami: Scaffolds for Creating Higher Order Structures. *Chemical reviews*, 117(20):12584–12640, 2017.

[155] Philipp C. Nickels, Bettina Wünsch, Phil Holzmeister, Wooli Bae, Luisa M. Kneer, Dina Grohmann, Philip Tinnefeld, and Tim Liedl. Molecular force spectroscopy with a DNA origami-based nanoscopic force clamp. *Science (New York, N.Y.)*, 354(6310):305–307, 2016.

[156] Jonas J. Funke, Philip Ketterer, Corinna Lieleg, Sarah Schunter, Philipp Korber, and Hendrik Dietz. Uncovering the forces between nucleosomes using DNA origami. *Science advances*, 2(11):e1600974, 2016.

[157] J. Chao, P. Zhang, Q. Wang, N. Wu, F. Zhang, J. Hu, C. H. Fan, and B. Li. Single-molecule imaging of DNA polymerase I (Klenow fragment) activity by atomic force microscopy. *Nanoscale*, 8(11):5842–5846, 2016.

[158] Xiaoxi Zhuang, Xiaowei Ma, Xiangdong Xue, Qiao Jiang, Linlin Song, Luru Dai, Chunqiu Zhang, Shubin Jin, Keni Yang, Baoquan Ding, Paul C. Wang, and Xing-Jie Liang. A Photosensitizer-Loaded DNA Origami Nanosystem for Photodynamic Therapy. *ACS nano*, 10(3):3486–3495, 2016.

[159] Ari Ora, Erika Järvihaavisto, Hongbo Zhang, Henni Auvinen, Hélder A. Santos, Mauri A. Kostiainen, and Veikko Linko. Cellular delivery of enzyme-loaded DNA origami. *Chemical communications (Cambridge, England)*, 52(98):14161–14164, 2016.

[160] Yi Chen, Ping Wang, Yang Liu, Ting Liu, Yan Xu, Shanshan Zhu, Jun Zhu, Kai Ye, Guang Huang, and He Dannong. Stability and recovery of DNA origami structure with cation concentration. *Nanotechnology*, 29(3):035102, 2018.

[161] Qian Mei, Xixi Wei, Fengyu Su, Yan Liu, Cody Youngbull, Roger Johnson, Stuart Lindsay, Hao Yan, and Deirdre Meldrum. Stability of DNA origami nanoarrays in cell lysate. *Nano letters*, 11(4):1477–1482, 2011.

[162] Saminathan Ramakrishnan, Georg Krainer, Guido Grundmeier, Michael Schlierf, and Adrian Keller. Cation-Induced Stabilization and Denaturation of DNA Origami Nanostructures in Urea and Guanidinium Chloride. *Small (Weinheim an der Bergstrasse, Germany)*, 13(44), 2017.

[163] Aleksandar Matković, Borislav Vasić, Jelena Pešić, Julia Prinz, Ilko Bald, Aleksandar R. Milosavljević, and Radoš Gajić. Enhanced structural stability of DNA origami nanostructures by graphene encapsulation. *New Journal of Physics*, 18(2):025016, 2016.

[164] Hieu Bui, Craig Onodera, Carson Kidwell, YerPeng Tan, Elton Graugnard, Wan Kuang, Jeunghoon Lee, William B. Knowlton, Bernard Yurke, and William L. Hughes. Programmable periodicity of quantum dot arrays with DNA origami nanotubes. *Nano letters*, 10(9):3367–3372, 2010.

[165] Lars Opherden, Jana Oertel, Astrid Barkleit, Karim Fahmy, and Adrian Keller. Paramagnetic decoration of DNA origami nanostructures by Eu^{3+} coordination. *Langmuir : the ACS journal of surfaces and colloids*, 30(27):8152–8159, 2014.

[166] Stefan Fischer, Caroline Hartl, Kilian Frank, Joachim O. Rädler, Tim Liedl, and Bert Nickel. Shape and Interhelical Spacing of DNA Origami Nanostructures Studied by Small-Angle X-ray Scattering. *Nano letters*, 16(7):4282–4287, 2016.

[167] S. Nakano, M. Fujimoto, H. Hara, and N. Sugimoto. Nucleic acid duplex stability: influence of base composition on cation effects. *Nucleic Acids Research*, 27(14):2957–2965, 1999.

[168] Richard Owczarzy, Bernardo G. Moreira, Yong You, Mark A. Behlke, and Joseph A. Walder. Predicting stability of DNA duplexes in solutions containing magnesium and monovalent cations. *Biochemistry*, 47(19):5336–5353, 2008.

[169] N. Korolev, A. P. Lyubartsev, A. Rupprecht, and L. Nordenskiold. Competitive binding of Mg(2+), Ca(2+), Na(+), and K(+) ions to DNA in oriented DNA fibers: experimental and monte carlo simulation results. *Biophysical Journal*, 77(5):2736–2749, 1999.

[170] I. A. Kuznetsov, V. I. Gorshkov, V. A. Ivanov, S. I. Kargov, N. I. Korolev, S. M. Fillippov, and R.Kh. Khamisov. Ion-exchange properties of immobilized DNA. *Reactive Polymers, Ion Exchangers, Sorbents*, 3(1):37–49, 1984.

[171] M. Louise Bleam, Charles F. Anderson, and M. Thomas Record. Relative binding affinities of monovalent cations for double-stranded DNA. *Proceedings of the National Academy of Sciences of the United States of America*, 77(6):3085–3089, 1980.

[172] V. P. Denisov and B. Halle. Sequence-specific binding of counterions to B-DNA. *Proceedings of the National Academy of Sciences*, 97(2):629–633, 2000.

[173] Yuhua Cheng, Nikolay Korolev, and Lars Nordenskiöld. Similarities and differences in interaction of K+ and Na+ with condensed ordered DNA. A molecular dynamics computer simulation study. *Nucleic Acids Research*, 34(2):686–696, 2006.

[174] Hale Bila, Eva E. Kurisinkal, and Maartje M. C. Bastings. Engineering a stable future for DNA-origami as a biomaterial. *Biomaterials science*, 7(2):532–541, 2019.

[175] Yi Chen, Ping Wang, Yan Xu, Xiaodi Li, Yuanjie Zhu, Ying Zhang, Jun Zhu, Gang Huang, and Dannong He. Different Stability of DNA Origami Nanostructure between on Interface and in Bulk Solution. *ACS Applied Bio Materials*, 1(5):1424–1429, 2018.

[176] Felix Kroener, Lukas Traxler, Andreas Heerwig, Ulrich Rant, and Michael Mertig. Magnesium-Dependent Electrical Actuation and Stability of DNA Origami Rods. *ACS applied materials & interfaces*, 11(2):2295–2301, 2019.

[177] Megan C. Engel, David M. Smith, Markus A. Jobst, Martin Sajfutdinow, Tim Liedl, Flavio Romano, Lorenzo Rovigatti, Ard A. Louis, and Jonathan P. K. Doye. Force-Induced Unravelling of DNA Origami. *ACS Nano*, 12(7):6734–6747, 2018.

[178] Saminathan Ramakrishnan, Boxuan Shen, Mauri A. Kostiainen, Guido Grundmeier, Adrian Keller, and Veikko Linko. Real-Time Observation of Superstructure-Dependent DNA Origami Digestion by DNase I Using High-Speed Atomic Force Microscopy. *Chembiochem : a European journal of chemical biology*, 2019.

[179] Bing Zhu, Yan Zhao, Jiangbing Dai, Jianbang Wang, Shu Xing, Linjie Guo, Nan Chen, Xiangmeng Qu, Li Li, Juwen Shen, Jiye Shi, Jiang Li, and Lihua Wang. Preservation of DNA Nanostructure Carriers: Effects of Freeze-Thawing and Ionic Strength during Lyophilization and Storage. *ACS applied materials & interfaces*, 9(22):18434–18439, 2017.

[180] Masayuki Endo, Yousuke Katsuda, Kumi Hidaka, and Hiroshi Sugiyama. A versatile DNA nanochip for direct analysis of DNA base-excision repair. *Angewandte Chemie (International ed. in English)*, 49(49):9412–9416, 2010.

[181] Seigi Yamamoto, Debojyoti De, Kumi Hidaka, Kyeong Kyu Kim, Masayuki Endo, and Hiroshi Sugiyama. Single molecule visualization and characterization of Sox2-Pax6 complex formation on a regulatory DNA element using a DNA origami frame. *Nano letters*, 14(5):2286–2292, 2014.

[182] Na Wu, Xingfei Zhou, Daniel M. Czajkowsky, Ming Ye, Dongdong Zeng, Yanming Fu, Chunhai Fan, Jun Hu, and Bin Li. In situ monitoring of single molecule binding reactions with time-lapse atomic force microscopy on functionalized DNA origami. *Nanoscale*, 3(6):2481–2484, 2011.

[183] Arivazhagan Rajendran, Masayuki Endo, Kumi Hidaka, Phong Lan Thao Tran, Jean-Louis Mergny, and Hiroshi Sugiyama. Controlling the stoichiometry and strand polarity of a tetramolecular G-quadruplex structure by using a DNA origami frame. *Nucleic acids research*, 41(18):8738–8747, 2013.

[184] Charlotte Kielar, Francesco V. Reddavide, Stefan Tubbenhauer, Meiying Cui, Xiaodan Xu, Guido Grundmeier, Yixin Zhang, and Adrian Keller. Pharmacophore Nanoarrays on DNA Origami Substrates as a Single-Molecule Assay for Fragment-Based Drug Discovery. *Angewandte Chemie (International ed. in English)*, 57(45):14873–14877, 2018.

[185] Basu R. Aryal, Tyler R. Westover, Dulashani R. Ranasinghe, Diana G. Calvopiña, Bibek Uprety, John N. Harb, Robert C. Davis, and Adam T. Woolley. Four-Point Probe Electrical Measurements on Templated Gold Nanowires Formed on Single DNA Origami Tiles. *Langmuir : the ACS journal of surfaces and colloids*, 34(49):15069–15077, 2018.

[186] Jenny Rackwitz, Janina Kopyra, Iwona Dabkowska, Kenny Ebel, MiloŠ Lj Ranković, Aleksandar R. Milosavljević, and Ilko Bald. Sensitizing DNA Towards Low-Energy Electrons with 2-Fluoroadenine. *Angewandte Chemie (International ed. in English)*, 55(35):10248–10252, 2016.

[187] Bezu Teschome, Stefan Facsko, Kurt V. Gothelf, and Adrian Keller. Alignment of Gold Nanoparticle-Decorated DNA Origami Nanotubes: Substrate Prepatterning versus Molecular Combing. *Langmuir : the ACS journal of surfaces and colloids*, 31(46):12823–12829, 2015.

[188] Kent S. Gates. An overview of chemical processes that damage cellular DNA: spontaneous hydrolysis, alkylation, and reactions with radicals. *Chemical research in toxicology*, 22(11):1747–1760, 2009.

[189] Supat Jiranusornkul and Charles A. Laughton. Destabilization of DNA duplexes by oxidative damage at guanine: implications for lesion recognition and repair. *Journal of the Royal Society, Interface*, 5 Suppl 3:S191–8, 2008.

[190] Sreelekha K. Singh, Marta W. Szulik, Manjori Ganguly, Irine Khutsishvili, Michael P. Stone, Luis A. Marky, and Barry Gold. Characterization of DNA with an 8-oxoguanine modification. *Nucleic acids research*, 39(15):6789–6801, 2011.

[191] Barbara Röder, Karin Frühwirth, Claus Vogl, Martin Wagner, and Peter Rossmanith. Impact of long-term storage on stability of standard DNA for nucleic acid-based methods. *Journal of clinical microbiology*, 48(11):4260–4262, 2010.

[192] Raphael M. Franzini, Dario Neri, and Jörg Scheuermann. DNA-encoded chemical libraries: advancing beyond conventional small-molecule libraries. *Accounts of chemical research*, 47(4):1247–1255, 2014.

[193] Ralph E. Kleiner, Christoph E. Dumelin, and David R. Liu. Small-molecule discovery from DNA-encoded chemical libraries. *Chemical Society reviews*, 40(12):5707–5717, 2011.

[194] Claudio Zambaldo, Sofia Barluenga, and Nicolas Winssinger. PNA-encoded chemical libraries. *Current opinion in chemical biology*, 26:8–15, 2015.

[195] Sofia Barluenga, Claudio Zambaldo, Heraklidia A. Ioannidou, Mihai Ciobanu, Pierre Morieux, Jean-Pierre Daguer, and Nicolas Winssinger. Novel PTP1B inhibitors identified by DNA display of fragment pairs. *Bioorganic & medicinal chemistry letters*, 26(3):1080–1085, 2016.

[196] Jean-Pierre Daguer, Claudio Zambaldo, Daniel Abegg, Sofia Barluenga, Cynthia Tallant, Susanne Müller, Alexander Adibekian, and Nicolas Winssinger. Identification of Covalent Bromodomain Binders through DNA Display of Small Molecules. *Angewandte Chemie (International ed. in English)*, 54(20):6057–6061, 2015.

[197] J.-P. Daguer, C. Zambaldo, M. Ciobanu, P. Morieux, S. Barluenga, and N. Winssinger. DNA display of fragment pairs as a tool for the discovery of novel biologically active small molecules. *Chemical science*, 6(1):739–744, 2015.

[198] Zev J. Gartner, Brian N. Tse, Rozalina Grubina, Jeffrey B. Doyon, Thomas M. Snyder, and David R. Liu. DNA-templated organic synthesis and selection of a library of macrocycles. *Science (New York, N.Y.)*, 305(5690):1601–1605, 2004.

[199] Markus Leimbacher, Yixin Zhang, Luca Mannocci, Michael Stravs, Tim Geppert, Jörg Scheuermann, Gisbert Schneider, and Dario Neri. Discovery of small-molecule interleukin-2 inhibitors from a DNA-encoded chemical library. *Chemistry (Weinheim an der Bergstrasse, Germany)*, 18(25):7729–7737, 2012.

[200] Peng Zhao, Zitian Chen, Yizhou Li, Dawei Sun, Yuan Gao, Yanyi Huang, and Xiaoyu Li. Selection of DNA-encoded small molecule libraries against unmodified and non-immobilized protein targets. *Angewandte Chemie (International ed. in English)*, 53(38):10056–10059, 2014.

[201] Gang Li, Ying Liu, Yu Liu, Li Chen, Siyu Wu, Yang Liu, and Xiaoyu Li. Photoaffinity labeling of small-molecule-binding proteins by DNA-templated chemistry. *Angewandte Chemie (International ed. in English)*, 52(36):9544–9549, 2013.

[202] Samu Melkko, Christoph E. Dumelin, Jörg Scheuermann, and Dario Neri. On the magnitude of the chelate effect for the recognition of proteins by pharmacophores scaffolded by self-assembling oligonucleotides. *Chemistry & biology*, 13(2):225–231, 2006.

[203] Francesco V. Reddavide, Weilin Lin, Sarah Lehnert, and Yixin Zhang. DNA-Encoded Dynamic Combinatorial Chemical Libraries. *Angewandte Chemie (International ed. in English)*, 54(27):7924–7928, 2015.

[204] T. Fournier, N. Medjoubi-N, and D. Porquet. Alpha-1-acid glycoprotein. *Biochimica et biophysica acta*, 1482(1-2):157–171, 2000.

[205] Masahiko Hirota, Masaki Ohmuraya, and Hideo Baba. The role of trypsin, trypsin inhibitor, and trypsin receptor in the onset and aggravation of pancreatitis. *Journal of gastroenterology*, 41(9):832–836, 2006.

[206] Samu Melkko, Yixin Zhang, Christoph E. Dumelin, Jörg Scheuermann, and Dario Neri. Isolation of high-affinity trypsin inhibitors from a DNA-encoded chemical library. *Angewandte Chemie (International ed. in English)*, 46(25):4671–4674, 2007.

[207] Maximilian T. Strauss, Florian Schueder, Daniel Haas, Philipp C. Nickels, and Ralf Jungmann. Quantifying absolute addressability in DNA origami with molecular resolution. *Nature communications*, 9(1):1600, 2018.

[208] Yonggang Ke, Stuart Lindsay, Yung Chang, Yan Liu, and Hao Yan. Self-assembled water-soluble nucleic acid probe tiles for label-free RNA hybridization assays. *Science (New York, N.Y.)*, 319(5860):180–183, 2008.

[209] Zhao Zhang, Dongdong Zeng, Hongwei Ma, Guoying Feng, Jun Hu, Lin He, Can Li, and Chunhai Fan. A DNA-Origami chip platform for label-free SNP genotyping using toehold-mediated strand displacement. *Small (Weinheim an der Bergstrasse, Germany)*, 6(17):1854–1858, 2010.

[210] Luca Mannocci, Samu Melkko, Fabian Buller, Ilona Molnàr, Jean-Paul Gapian Bianké, Christoph E. Dumelin, Jörg Scheuermann, and Dario Neri. Isolation of potent and specific trypsin inhibitors from a DNA-encoded chemical library. *Bioconjugate chemistry*, 21(10):1836–1841, 2010.

[211] Adrian Keller, Janina Kopyra, Kurt V. Gothelf, and Ilko Bald. Electron-induced damage of biotin studied in the gas phase and in the condensed phase at a single-molecule level. *New Journal of Physics*, 15(8):083045, 2013.

[212] Luvena L. Ong, Nikita Hanikel, Omar K. Yaghi, Casey Grun, Maximilian T. Strauss, Patrick Bron, Josephine Lai-Kee-Him, Florian Schueder, Bei Wang, Pengfei Wang, Jocelyn Y. Kishi, Cameron Myhrvold, Allen Zhu, Ralf Jungmann, Gaetan Bellot, Yonggang Ke, and Peng Yin. Programmable self-assembly of three-dimensional nanostructures from 10,000 unique components. *Nature*, 552(7683):72–77, 2017.

[213] Thomas Bocklitz, Evelyn Kämmer, Stephan Stöckel, Dana Cialla-May, Karina Weber, Roland Zell, Volker Deckert, and Jürgen Popp. Single virus detection by means of atomic force microscopy in combination with advanced image analysis. *Journal of structural biology*, 188(1):30–38, 2014.

[214] Arivazhagan Rajendran, Masayuki Endo, and Hiroshi Sugiyama. State-of-the-art high-speed atomic force microscopy for investigation of single-molecular dynamics of proteins. *Chemical reviews*, 114(2):1493–1520, 2014.

[215] Noriyuki Kodera, Daisuke Yamamoto, Ryoki Ishikawa, and Toshio Ando. Video imaging of walking myosin V by high-speed atomic force microscopy. *Nature*, 468:72 EP –, 2010.

[216] Adrian P. Nievergelt, Niccolò Banterle, Santiago H. Andany, Pierre Gönczy, and Georg E. Fantner. High-speed photothermal off-resonance atomic force microscopy reveals assembly routes of centriolar scaffold protein SAS-6. *Nature nanotechnology*, 13(8):696–701, 2018.

[217] Beata E. Mierzwa, Nicolas Chiaruttini, Lorena Redondo-Morata, Joachim Moser von Filseck, Julia König, Jorge Larios, Ina Poser, Thomas Müller-Reichert, Simon Scheuring, Aurélien Roux, and Daniel W. Gerlich. Dynamic subunit turnover in ESCRT-III assemblies is regulated by Vps4 to mediate membrane remodelling during cytokinesis. *Nature cell biology*, 19(7):787–798, 2017.

[218] Tetsuya Takeda, Toshiya Kozai, Huiran Yang, Daiki Ishikuro, Kaho Seyama, Yusuke Kumagai, Tadashi Abe, Hiroshi Yamada, Takayuki Uchihashi, Toshio Ando, and Kohji Takei. Dynamic clustering of dynamin-amphiphysin helices regulates membrane constriction and fission coupled with GTP hydrolysis. *eLife*, 7, 2018.

[219] Nicolas Chiaruttini, Lorena Redondo-Morata, Adai Colom, Frédéric Humbert, Martin Lenz, Simon Scheuring, and Aurélien Roux. Relaxation of Loaded ESCRT-III Spiral Springs Drives Membrane Deformation. *Cell*, 163(4):866–879, 2015.

[220] Mikihiro Shibata, Hiroshi Nishimasu, Noriyuki Kodera, Seiichi Hirano, Toshio Ando, Takayuki Uchihashi, and Osamu Nureki. Real-space and real-time dynamics of CRISPR-Cas9 visualized by high-speed atomic force microscopy. *Nature communications*, 8(1):1430, 2017.

[221] Toshiya Kozai, Taichiro Sekiguchi, Tadashi Satoh, Hirokazu Yagi, Koichi Kato, and Takayuki Uchihashi. Two-step process for disassembly mechanism of proteasome α7 homo-tetradecamer by α6 revealed by high-speed atomic force microscopy. *Scientific reports*, 7(1):15373, 2017.

[222] Masaki Okumura, Kentaro Noi, Shingo Kanemura, Misaki Kinoshita, Tomohide Saio, Yuichi Inoue, Takaaki Hikima, Shuji Akiyama, Teru Ogura, and Kenji Inaba. Dynamic assembly of protein disulfide isomerase in catalysis of oxidative folding. *Nature chemical biology*, 15(5):499–509, 2019.

[223] Markus Sutter, Matthew Faulkner, Clément Aussignargues, Bradley C. Paasch, Steve Barrett, Cheryl A. Kerfeld, and Lu-Ning Liu. Visualization of Bacterial Microcompartment Facet Assembly Using High-Speed Atomic Force Microscopy. *Nano letters*, 16(3):1590–1595, 2016.

[224] Takamitsu Haruyama, Yasunori Sugano, Noriyuki Kodera, Takayuki Uchihashi, Toshio Ando, Yoshiki Tanaka, Hiroki Konno, and Tomoya Tsukazaki. Single-Unit Imaging of Membrane Protein-Embedded Nanodiscs from Two Oriented Sides by High-Speed Atomic Force Microscopy. *Structure (London, England : 1993)*, 27(1):152–160.e3, 2019.

[225] Takayuki Uchihashi, Noriyuki Kodera, and Toshio Ando. Guide to video recording of structure dynamics and dynamic processes of proteins by high-speed atomic force microscopy. *Nature Protocols*, 7(6):1193–1206, 2012.

[226] Sandra Sagredo, Tobias Pirzer, Ali Aghebat Rafat, Marisa A. Goetzfried, Gabriel Moncalian, Friedrich C. Simmel, and Fernando de la Cruz. Orthogonal Protein Assembly on DNA Nanostructures Using Relaxases. *Angewandte Chemie International Edition*, 55(13):4348–4352, 2016.

[227] Barbara Saccà and Christof M. Niemeyer. DNA origami: the art of folding DNA. *Angewandte Chemie (International ed. in English)*, 51(1):58–66, 2012.

[228] William Hawkes, Da Huang, Paul Reynolds, Linda Hammond, Matthew Ward, Nikolaj Gadegaard, John F. Marshall, Thomas Iskratsch, and Matteo Palma. Probing the nanoscale organisation and multivalency of cell surface receptors: DNA origami nanoarrays for cellular studies with single-molecule control. *Faraday discussions*, 219(0):203–219, 2019.

[229] N. Michael Green. Avidin and streptavidin. In Meir Wilchek, editor, *Avidin-biotin technology*, volume 184 of *Methods in Enzymology*, pages 51–67. Acad. Press, San Diego, Calif., 1990.

[230] F. Gołek, P. Mazur, Z. Ryszka, and S. Zuber. AFM image artifacts. *Applied Surface Science*, 304:11–19, 2014.

Publications

Parts of this thesis have been published in:

1. C. Kielar, F. V. Reddavide, S. Tubbenhauer, M. Cui, X. Xu, G. Grundmeier, Y. Zhang, and A. Keller: *Pharmacophore Nanoarrays on DNA Origami Substrates as a Single-Molecule Assay for Fragment-Based Drug Discovery*; Angewandte Chemie International Edition; 57(45); 2018
2. C. Kielar, Y. Xin, B. Shen, M. A. Konstiainen, G. Grundmeier, V. Linko, and A. Keller: *On the Stability of DNA Origami Nanostructures in Low-Magnesium Buffers*, Angewandte Chemie International Edition; 57(30); 2018
3. C. Kielar, Y. Xin, X. Xu, S. Zhu, N. Gorin, G. Grundmeier, C. Möser, D. M. Smith, and A. Keller: *Effect of Staple Age on DNA Origami Nanostructure Assembly and Stability*; Molecules; 24(14); 2019

Other publications:

1. C. Kielar, S. Ramakrishnan, S. Fricke, G. Grundmeier, and A. Keller: *Dynamics of DNA Origami Lattice Formation at Solid-Liquid Interfaces*, ACS applied materials & interfaces; 10(51); 2018
2. B. Hämisch, A. Büngeler, C. Kielar, A. Keller, O. Strube, and K. Huber: *Self-Assembly of Fibrinogen in Aqueous, Thrombin Free Solutions of Variable Ionic Strength*; Langmuir; 35,37; 2019
3. Y. Xin, C. Kielar, S. Zhu, C. Sikeler, X. Xu, C. Möser, G. Grundmeier, T. Liedl, A. Heuer-Jungemann, D. M. Smith, and A. Keller: *Cryopreservation of DNA origami nanostructures*; Small 2020; 1905959

Acknowledgements

I want to Professor Dr. Guido Grundmeier for giving me this chance and his support throughout my thesis and my studies. I really appreciate the time I have been working in his group.

I would like to thank my thesis advisor Dr. Adrian Keller for his guidance throughout my thesis and the many fruitful discussions.

Special thanks to my mates Yu, Yang, Zin, and Sam. It was a great pleasure to work with you.

All our collaborators who contributed to this thesis are sincerely acknowledged: Professor Dr. Yixin Zhang and Dr. Francesco Reddavide from Dresden, Christin Möser and David M. Smith from Leipzig, and Dr. Veikko Linko, Dr. Boxuan Shen, Professor Dr. Mauri A. Kostiainen from Finland.

I thank my friends Peter, Frank, Matthias, Ronny, and Karim for their selfless and extraordinary friendship.

Last but not least I want to thank my family for their ongoing support during my studies and my thesis. Without you I could not have done this.